ÇUKUROVA UNIVERSITY
INSTITUTE OF NATURAL AND APPLIED SCIENCES

PhD THESIS

Mehmet BÜYÜK

DESIGN AND EXPERIMENTAL VERIFICATION OF RESONANCE DAMPING METHODS FOR A SHUNT ACTIVE POWER FILTER WITH LCL FILTER

DEPARTMENT OF ELECTRICAL AND ELECTRONICS ENGINEERING

ADANA-2019

ÇUKUROVA UNIVERSITY
INSTITUTE OF NATURAL AND APPLIED SCIENCES

DESIGN AND EXPERIMENTAL VERIFICATION OF RESONANCE DAMPING METHODS FOR A SHUNT ACTIVE POWER FILTER WITH LCL FILTER

Mehmet BÜYÜK

PhD THESIS

DEPARTMENT OF ELECTRICAL AND ELECTRONICS ENGINEERING

We certify that the thesis titled above was reviewed and approved for the award of degree of the Doctor of Philosophy by the board of jury on 06/12/2019.

……………………………	……………………………………	…………………………………..
Prof. Dr. Mehmet TÜMAY SUPERVISOR	Prof. Dr. K. Çağatay BAYINDIR MEMBER	Assoc. Prof. Dr. M. Uğraş CUMA MEMBER
……………………………	……………………………………	
Asst. Prof. Dr. Adnan TAN MEMBER	Asst. Prof. Dr. M. Mustafa SAVRUN MEMBER	

This PhD Thesis is written at the Department of Electrical and Electronics Engineering of Institute of Natural and Applied Sciences of Çukurova University.
Registration Number:

Prof. Dr. Mustafa GÖK
Director
Institute of Natural and Applied Sciences

ABSTRACT

PhD THESIS

DESIGN AND EXPERIMENTAL VERIFICATION OF RESONANCE DAMPING METHODS FOR A SHUNT ACTIVE POWER FILTER WITH LCL FILTER

Mehmet BÜYÜK

ÇUKUROVA UNIVERSITY
INSTITUTE OF NATURAL AND APPLIED SCIENCES
DEPARTMENT OF ELECTRICAL AND ELECTRONICS ENGINEERING

Supervisor : Prof. Dr. Mehmet TÜMAY
Year: 2019, Pages: 175
Jury : Prof. Dr. Mehmet TÜMAY
: Prof. Dr. K. Çağatay BAYINDIR
: Assoc. Prof. Dr. M. Uğraş CUMA
: Assist. Prof. Dr. Adnan TAN
: Assist. Prof. Dr. M. Mustafa SAVRUN

A Shunt Active Power Filter (SAPF) with LCL filter is designed and constructed in order to examine and apply various damping methods for the resonance issue of LCL filter. In this thesis work, by this means, passive damping (PD) method, active damping (AD) method and auxiliary converter based damping method are investigated and compared according to power losses, resonance damping performance, impact on harmonic compensation and implementation cost. A converter based active damper (CBAD) method is proposed in this thesis to suppress the resonance of LCL filter. Additionally, the design of LCL filter for SAPF is presented and the constraints of the design are conducted and explained in detail. In this thesis study, the implemented SAPF with LCL filter prototype is designed to compensate dominant low order harmonic currents of six pulse rectifiers up to 15A. In the scope of this thesis, a control algorithm is developed and applied to the SAPF with LCL filter prototype. The performances of LCL filter interfaced SAPF with the developed control algorithm and the applied damping methods are verified in the steady-state and dynamic situations with comprehensive experimental results.

Key Words: Harmonic Compensation, Shunt Active Power Filters (SAPF), LCL Filter, Resonance Damping, Passive Damping (PD), Active Damping (AD), Converter Based Active Damper (CBAD)

ÖZ

DOKTORA TEZİ

LCL FİLTRELİ AKTİF GÜÇ FİLTRESİ İÇİN RESONANCE SÖNÜMLEME YÖNTEMLERİNİN TASARIMI VE DENEYSEL DOĞRULAMASI

Mehmet BÜYÜK

ÇUKUROVA ÜNİVERSİTESİ
FEN BİLİMLERİ ENSTİTÜSÜ
ELEKTRİK – ELEKTRONİK MÜHENDİSLİĞİ ANABİLİM DALI

Danışman : Prof. Dr. Mehmet TÜMAY
Year: 2019, Pages: 175
Jüri : Prof. Dr. Mehmet TÜMAY
: Prof. Dr. K. Çağatay BAYINDIR
: Doç. Dr. M. Uğraş CUMA
: Dr. Ögr. Üyesi Adnan TAN
: Dr. Öğr. Üyesi M. Mustafa SAVRUN

LCL filtresinin rezonans problemi için farklı sönümleme yöntemlerini incelemek ve uygulamak amacıyla LCL filtreli Şönt Aktif Güç Filtresi (ŞAGF) tasarlanmış ve uygulanmıştır. Bu bağlamda, bu tez çalışmasında pasif sönümleme (PS) yöntemi, aktif sönümleme (AS) yöntemi ve konvertör tabanlı sönümleme yöntemi incelenmiş ve güç kayıpları, rezonans sönümleme performansları, harmonik kompanzasyonu üzerindeki etkileri ve maliyetler açısında kıyaslaması yapılmıştır. Bu tezde, LCL filtresinin rezonansını sönümlemek için dönüştürücü tabanlı aktif sönümleyici (DTAS) yöntemi önerilmiştir. Ayrıca, ŞAGF için LCL filtresinin tasarımı sunulmuş ve tasarımdaki zorluklar ele alınıp, ayrıntılı olarak açıklanmıştır. Bu tez çalışmasında, LCL filtreli ŞAGF prototipi altı darbeli doğrultucunun 15A'e kadar düşük dereceli harmonik akımlarını kompanze etmek için tasarlanmıştır. Bu tez çalışması kapsamında, LCL filtreli ŞAF için bir kontrol algoritması geliştirilerek uygulanmıştır. LCL filtreli ŞAGF için geliştirilen kontrol algoritması ve uygulanan sönümleme yöntemlerinin kararlı ve dinamik durumlardaki performansları kapsamlı deneysel sonuçlarla doğrulanmıştır.

Anahtar Kelimeler: Harmonik Kompanzasyonu, Şönt Aktif Güç Filtresi (ŞAGF), LCL Filtresi, Rezonans Sönümlemesi, Pasif Sönümleme (PS), Aktif Sönümleme (AS), Dönüştürücü tabanlı Aktif Sönümleyici (DTAS)

ACKNOWLEDGEMENTS

I would like to express my deepest gratitude to my supervisor Prof. Dr. Mehmet TÜMAY for his support, guidance and encouragement during this thesis study. I would like also thank for his valuable contributions not only to my academic knowledge but also for confidence in me.

I would like to present my special thanks to Prof. Dr. K. Çağatay BAYINDIR and Assoc. Prof. Dr. M. Uğraş CUMA for their comments and suggestions in my thesis progress committee.

I wish to express my endless thanks to Asst. Prof. Dr. Adnan TAN for his continuous help and sharing his valuable knowledge and experience on electrical power quality and active power filters.

I am also grateful to Asst. Prof. Dr. Mustafa SAVRUN and Asst. Prof. Dr. Tahsin KÖROĞLU for their support.

I am thankful to Asst. Prof. Dr. Mustafa İNCİ for sharing his knowledge and help.

I would like to express my thanks to technicians Metin KURT and Sefa MERAL for their voluntary help.

I thank to my father Zeynettin BÜYÜK, my mother Meryem BÜYÜK, my wife Emine BÜYÜK and my borthers and sisters for helping and supporting me throughout my entire life.

CONTENTS **PAGE**

LIST OF TABLES **PAGE**

LIST OF FIGURES **PAGE**

LIST OF ABBREVIATIONS

A	: Amperes
AC	: Alternative Current
AD	: Active Damping
ADC	: Analog to Digital Conversion
ANN	: Artificial Neural Netwoek
ASD	: Adjustable Speed Drives
CBAD	: Converter Based Active Damper
CSI	: Current Source Inverter
DC	: Direct Current
DFT	: Discrete Fourier Transform
DQ	: Direct-Quadrate
DSP	: Digital Signal Processor
EMI	: Electromagnetic Interface
ESL	: Equivalent Series Inductance
ESR	: Equivalent Series Resistance
F	: Frequency
FFT	: Fast Fourier Transform
FWD	: Freewheeling Diode
HPF	: High Pass Filter
HVDC	: High Voltage Direct Current
Hz	: Hertz
IEC	: International Electro-technical Commission
IEEE	: Institute of Electrical and Electronics Engineers
IGBT	: Insulated Gate Bipolar Transistor
IHD	: Individual Harmonic Distortion
KW	: Kilo Watts
L	: Inductor

LC	: Inductor-Capacitor
LCL	: Inductor-Capacitor-Inductor
LPF	: Low Pass Filter
MCU	: Microcontroller
MOSFET	: Metal Oxide Semiconductor Field Effect Transistor
PCC	: Point of Common Coupling
PD	: Passive Damping
PF	: Passive Filter
PI	: Proportional Integrator
PQ	: Power Quality
PR	: Proportional Resonant
PWM	: Pulse Width Modulation
RDFT	: Recursive Discrete Fourier Transform
SAPF	: Shunt Active Power Filter
SPWM	: Sinusoidal Pulse Width Modulation
SRF	: Synchronous Reference Frame
STATCOM	: Static Compensator
TDD	: Total Demand Distortion
THD	: Total Harmonic Distortion
V	: Volts
VSI	: Voltage Source Inverter
WACC	: Weighted Average Current Control

1. INTRODUCTION

The rapid development in power electronics based technology and the growing change of the electrical load characteristics with increasing electrical energy consumption bring about electrical energy quality and efficiency concerns to come into prominent in recent years. Despite providing controllable efficient systems to many applications in industry and domestic, the power electronics based technology creates electrical power quality (PQ) issues including impacts on the entire systems such as consumer, distribution, generation and transmission. PQ is mainly clarified as the problems in voltage and current waveforms consisting of amplitude and/or frequency that result in malfunction and failure of equipment tied to electric grid system.

In electrical grid system, the most widespread PQ problem is harmonics generated by nonlinear loads such as arc furnaces, uncontrolled/controlled rectifiers and adjustable speed drives (ASDs) etc. Although these nonlinear loads maintain improvement of electrical energy system efficiency, they draw currents from the electric grid including fundamental and harmonic components. The harmonic components lead to degradation of electric energy efficiency due to increasing rms value of the line current, disturbance on the communication network and disoperation of control system etc. PQ issues cause significant revenue and economical losses of countries and reduction in humanity life quality (Özkaya, 2007). Hence, PQ problems, especially harmonics issue, should be taken into consideration as important issue required to be solved.

Traditional passive filters (PFs) are used as an earlier solution owing to lower cost and easy installation (Fujita and Akagi, 1991). Nevertheless, some drawbacks, limited capacity and compensation performance of PFs make them economically infeasible. Furthermore, the increasing growth in semiconductor devices like Insulated Gate Bipolar Transistor (IGBT) and high performance microcontroller play an important role in the development of active power filters

(APFs). In addition, the enhancement of control methods in power electronic based devices gives rise in practical application and commercial products. Compared with PFs, APFs have excellent harmonic filtering performance and smaller physical volume. APFs is mainly formed by semiconductor devices based devices such as voltage source inverter (VSI) which includes switching components like IGBTs or MOSFETs. The operation principle of APFs is based on controlling the switching components of VSI. However, another problem arises during operation of VSI because of switching IGBTs. High order ripple harmonics are produced due to switching VSI components. These ripple harmonics are generated at the switching frequency and multiples of the switching frequency. Therefore, these switching ripple harmonics issue are to be solved.

To alleviate switching related harmonics problem, a single inductor (L) interface filter is used with APFs. A bulky inductor, resulting in a huge physical size, is required to ensure effective attenuation of the switching ripple harmonics. However, the larger interface inductance value is, the higher dc link voltage level of VSI is, thus, leading an increased cost of APF system. In order to overcome this phenomena, inductor-capacitor-inductor (LCL) interface filter is proposed for grid-connected VSI in the last two decades and for APFs in recent one decade. LCL filter has remarkable mitigation performance of the switching harmonics in comparison to single L filter. On the other hand, LCL filter has a significant resonance problem, which must be solved, endangering the stability of APF system.

Different resonance damping methods have been presented in literature. The resonance damping methods are mainly based on passive components, modification in control algorithm and an auxiliary VSI. The details of these methods are presented in the following sections. Their benefits and drawbacks are given in detail.

1.1. Harmonics: Definition and Solutions

1.1.1. Definition of Harmonics

Harmonic is defined as a signal that has a multiple integer frequency of another reference signal. In electric system, harmonics are sinusoidal voltage/current with multiple integer of fundamental frequency 50/60 Hz (IEC, 1990; IEEE, 2009). The fundamental, third harmonic and distorted waveforms are demonstrated in Figure 1.1. Current harmonics are raised from nonlinear loads in power system. On the other hand, voltage harmonics are aroused from the current harmonics. Voltage and current harmonics result in voltage drop and additional power losses in power system. Moreover, they may interference with other systems and cause malfunction operation of the systems.

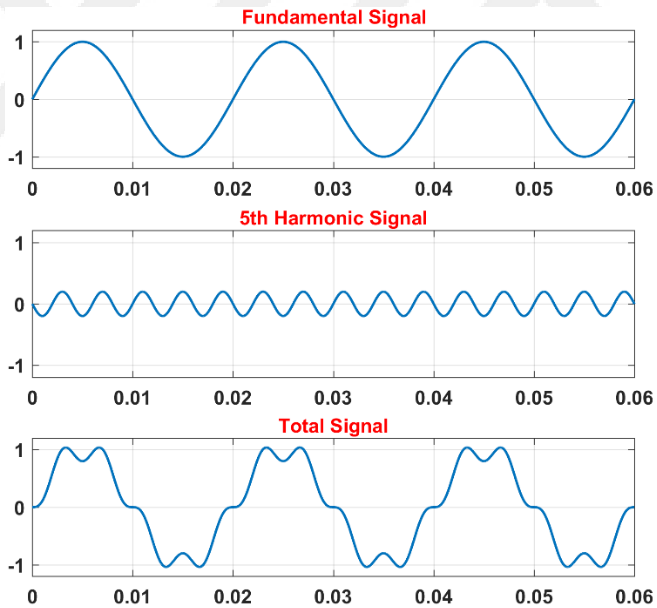

Figure 1.1. Fundamental, fifth harmonic and distorted waveforms

1.1.1.1. The Effects of Harmonics

The design of electrical grid systems are performed according to operation of linear loads. However, the nonlinear loads are used in the electric grid system, and they behave as harmonic current source and supply harmonic currents to the electrical grid. On the other hand, generators, transformers and transmission lines demonstrate linear characteristics such as series and/or parallel connected resistance, inductance and capacitance. Besides, reactive power compensation systems are widespread used in the industrial plants and they include large capacitor banks. Considering series and/or parallel connected inductance and capacitance in the power system, the nonlinear loads may cause resonance issue when connected to electrical grid. The resonance issue magnifies voltage or current in electrical grid.

The sensitivity of the electrical grid or other system change the impacts of harmonics (IEEE, 1992). These impacts are classified as short term and long term. The short term impacts are improper operation or decreased performance of other equipment. In short term effects, electronic based systems and power electronic based converters are usually affected from harmonics. In long term effects, on the other side, thermal losses and overheating occur in motors, transformers, cables and capacitors, which diminish lifetime of equipment or may even damage the equipment (IEC, 2002).

1.1.1.2. Standards and Measure of Harmonics

In behalf of advanced utilization of electrical energy, some international standards are recommended by IEEE and IEC to prevent the consumer from adverse effects of low electric power quality and to provide clean and sustainable electrical energy. These standards, IEEE 519-1992 and EN61000-3-4, regulate electric power quality issue such as power factor and harmonics etc. (IEEE, 1992; IEC, 1998). Besides, these standards determine obligations of supplier and customer. The harmonics and low power factor in electric grid increase the losses on electric cables and limit the usage capacity of cables. Especially, the harmonics that generated by nonlinear loads pollute the electric power system and heavily influence the operation of electronic systems.

Total harmonic distortion (THD), individual harmonic distortion (IHD) and total demand distortion (TDD) determine the harmonic distortion amount of voltage/current signals and specify harmonic limit levels. IHD is explained as the ratio of individual harmonic rms value to fundamental signal rms value. The calculation of IHD for voltage and current is given in Eq. 1.1.

$$IHD_Y = \frac{Y_h}{Y_1}\ ; \quad Y: V\ or\ I \tag{1.1}$$

Where h is the order of related individual harmonic.

THD is defined as the ratio rms value of individual harmonic signals to rms value of fundamental signal. The calculation of THD for voltage and current is given in Eq. 1.2. THD is an index that measures distortion of a periodic signal including harmonics with fundamental signal and demonstrates the overall distortion impact on the electric grid system.

$$THD_Y = \frac{\sqrt{\sum_{h=2} Y_h^2}}{Y_1}\ ; \quad Y: V\ or\ I \tag{1.2}$$

Although THD and IHD are used to define harmonic limits, these indices may mislead under some situations. Thus, another parameter for determination of harmonics TDD is used. TDD is determined as the ratio of rms value of individual harmonic signals to rms value of rated demand current of load. The calculation of TDD is performed for load current and given in Eq. 1.3. IEEE Std. 519-1992 recommends the limits for individual harmonics and TDD as presented in Table 1.1.

$$TDD_I = \frac{\sqrt{\sum_{h=2} I_h^2}}{I_L} \tag{1.3}$$

Table 1.1. Distortion limits of current harmonics specified by IEEE Std. 519-1992

I_{sc}/I_L	<11 (%)	11≤h<17 (%)	17≤h<23 (%)	23≤h<35 (%)	35≤h (%)	TDD (%)
<20	4.0	2.0	1.5	0.6	0.3	5.0
20<50	7.0	3.5	2.5	1.0	0.5	8.0
50<100	10.0	4.5	4.0	1.5	0.7	12.0
100<1000	12.0	5.5	5.0	2.0	1.0	15.0
>1000	15.0	7.0	6.0	2.5	1.4	20.0

1.1.2. Solutions of Harmonics Issue

Harmonics phenomena in electrical grid system is mitigated by two common systems. In literature, passive filters (PFs) or active power filters (APFs) are offered to eliminate the harmonics. The passive filters which consist of inductors, capacitors and resistors are simple and cheap solution for harmonics compensation. APFs, on the other hand, consist of power electronic equipment.

PFs have been preferred in the electrical grid system for a long time because of simple installation and low cost. PFs are connected in parallel or series with AC grid near to harmonic source and perform harmonic mitigation by tuning the passive components at individual harmonic frequency order such as 5th, 7th, 11th, 13th, etc. (Liang and Ilochonwu, 2011). Each passive filter shows low impedance at pre-tuned frequency. PFs are mainly connected in series or parallel to the systems. The series PFs are applied between the electrical grid and nonlinear load in series connection to prevent the tuned harmonic frequency component flowing on grid through performing high impedance. However, the series PFs require high rating components because of carrying the rated current of load on. Parallel PFs, commonly preferred type, are installed in parallel with nonlinear load. The parallel PFs show low impedance at the tuned harmonic frequency and ensure that dominant harmonic current flowing on it. The widespread used parallel PFs are demonstrated in Figure 1.2.

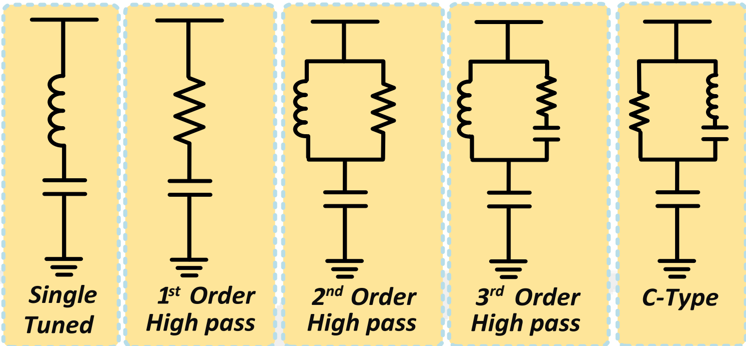

Figure 1.2. Widespread used parallel PFs in electrical grid system (Tan, 2015)

Single tuned PF is commonly used type of parallel PFs, which also called band-pass filter (Akagi, 1996). In this filter type, PF components, inductor and capacitor, are tuned to a single frequency having too low frequency at related frequency. This PF type provides sufficient compensation for tuned frequency and economical solution. Another PF type, high pass filter, has low frequency for wide range of harmonic frequencies. However, these PF types are preferred in low power applications due to high power losses and reactive power consumption (Arrillaga, 1997). C-type PFs, showing similar compensation performance with high pass PFs, are used to reduce to power losses owing to fundamental frequency. In general, this PF type is installed with arc furnaces and HVDC.

Even though PFs have several advantages, the applications of PFs are restricted due to resonance risk with grid impedance and requiring bulky system to eliminate multiple harmonic orders, lifetime and overloading of PFs.

The limited performance and usage of PFs lead to improvement of APFs for 1970s (Akagi, 2005). APFs can mainly be categorized through their connection to Point of Common Coupling (PCC); either series APF or shunt APF (Singh et al., 1999; El-Habrouk et al., 2000). General demonstrations of APFs are illustrated in

Figure 1.3. Series APFs compensate voltage harmonics, sag and swell problems while shunt APFs are capable of eliminating current harmonics, reactive power, negative and zero sequence current components (Buyuk et al., 2015; Inci et al., 2016). In industrial applications, since the most of loads cause current harmonics in the power system, shunt APFs have found their common penetration into the most industrial plants in order to alleviate the harmonic currents. Shunt APFs can be single-phase or three-phase. Three-phase shunt APFs have more interest and applications thanks to high power capability.

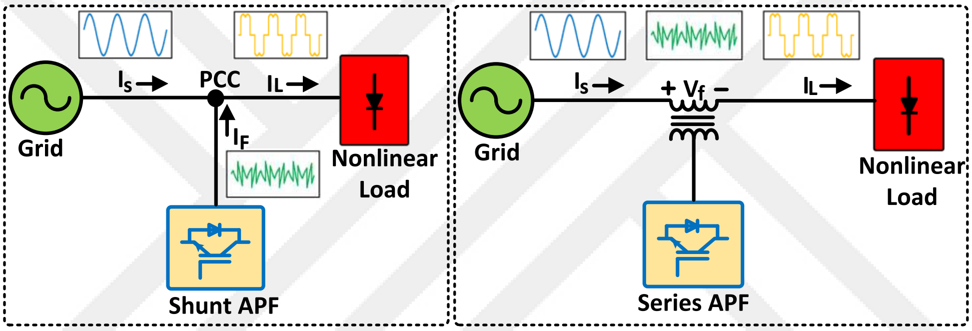

Figure 1.3. Block diagrams of APFs: shunt APF (left) and series APF (right)

Shunt active power filters (SAPF) are classified in terms of converter source type as current source inverter (CSI) or voltage source inverter (VSI). The general demonstrations of these APF types are shown in Figure 1.4. CSI based APF consists of three-phase bridge converter, dc link inductor and an LC interface filter. In CSI-APF, the reactor is used to store the required energy for the compensation and converter switching losses. The advantages of CSI-APF are fast and excellent current control performance (Terciyanlı, 2010). However, power losses, installation cost and size of CSI-APF are excessively high. VSI-APF includes three-phase bridge converter, dc link capacitor and an L interface filter. In VSI-APF, different from CSI-APF, the capacitors are used to store the required energy for compensation and converter switching losses. The advantages of VSI-APF are high efficiency, low installation cost and size (Akagi, 2005; Routimo et al., 2007). In literature and industry, VSI-APF has more attraction on academic research and practical applications than CSI-APF because of its several advantages. By this means, VSI based APF topology, named SAPF hereafter, are preferred in this thesis studies.

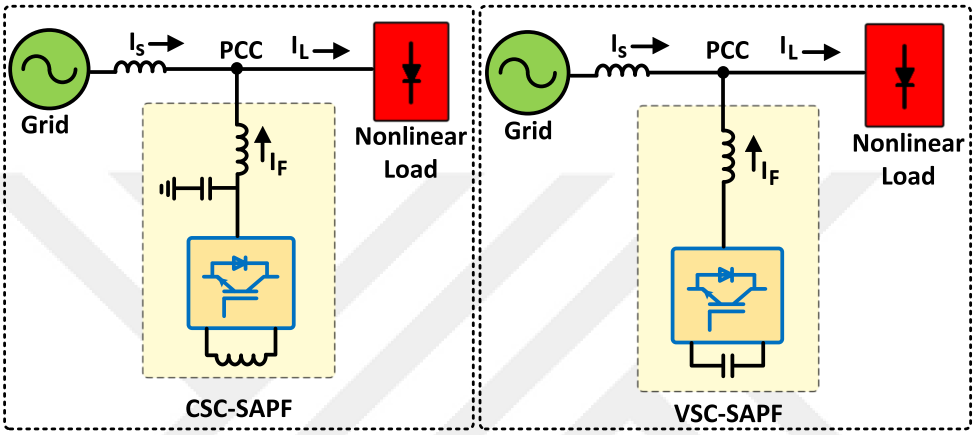

Figure 1.4. Block diagrams of SAPFs: CSC-SAPF (left) and VSC-SAPF (right)

1.2. Interface Filters of VSIs: L, LC and LCL

The progression in power electronic devices and digital signal processor encourage advances in power quality devices. The enhancement of semiconductor components such as IGBTs and MOSFETs with high sophisticated DSPs have led the utilization of VSI in APFs (Büyük, 2015). VSIs are generally modulated by sinusoidal pulse width modulation (SPWM) method to generate harmonic compensation currents. The harmonic compensation currents are generated during switching IGBT switches of VSI. However, switching ripple harmonics (SRHs) are released during switching of VSI, which raise THD of the electrical grid system, thereby the requirements of standards are not satisfied (Buyuk et al., 2016). Single L, LC and LCL filters are the most commonly investigated filter types. The circuit diagrams of these filters are illustrated in Figure 1.5.

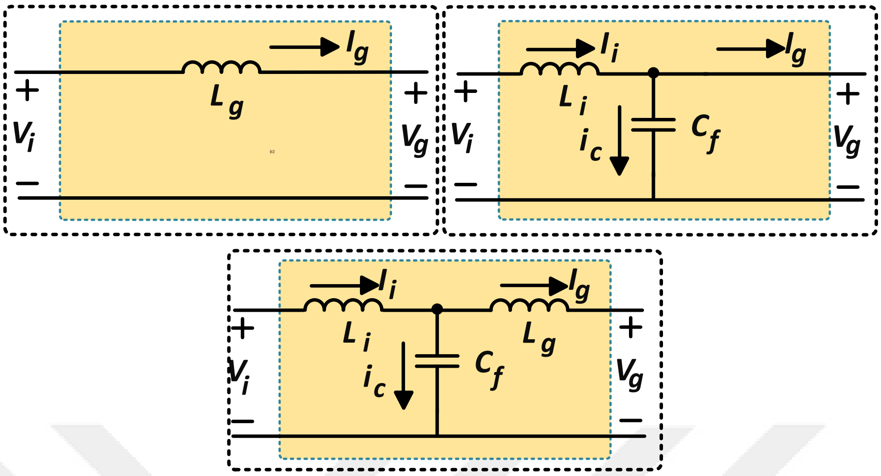

Figure 1.5. Equivalent circuits of L, LC and LCL filters

Single L (inductance) filter was traditionally used so as to mitigate the SRHs and interface VSI with the grid. Nevertheless, a single first-order L filter are not able to attenuate the SRFs enough in the higher frequencies (Büyük et al., 2016). Furthermore, although it has simple design, single L filter requires high inductance to sufficiently attenuate SRHs, resulting in bulky size. In recent literature, single L filter has rare applications due to its drawbacks.

LC (inductance-capacitance) filter, another type of SRFs, is preferred instead of single L filter to ensure greater mitigation of SRHs and satisfy the requirements of standards (Li, 2009; Lo Calzo et al., 2015). In this filter type, the capacitor shows low impedance at high frequencies, thus, switching harmonic components pass through it. But, this filter type has a resonance which frequency excessively change with the grid impedance.

LCL (inductance-capacitance-inductance) filter, in recent years, is the most commonly used filter type in literature studies and commercial products (Serpa et al., 2007; Channegowda and John, 2010; Jia et al., 2014; Reznik et al., 2014; Zhang et al., 2014). The attenuation of high frequencies of LCL filter is greater than single L and LC filters. Because of effective attenuation of switching harmonic components, a smaller inductance is used in LCL filter. Thus, voltage drop on the inductance is smaller than previous two filter types. However, LCL filter, compared with L and LC filters, has several disadvantages such as phase lag and design complication (Zou et al., 2014).

In order to analyze the filter performances, Bode diagram is plotted from the filter transfer functions. The transfer functions of single L, LC and LCL filters, obtained from block diagrams shown in Figure 1.6, are given in Eqs. 1.4, 1.5 and 1.6, respectively. As seen from Eqs. 1.5 and 1.6, LC and LCL filters have resonances. The resonance frequencies are calculated as in Eqs. 1.7 and 1.8.

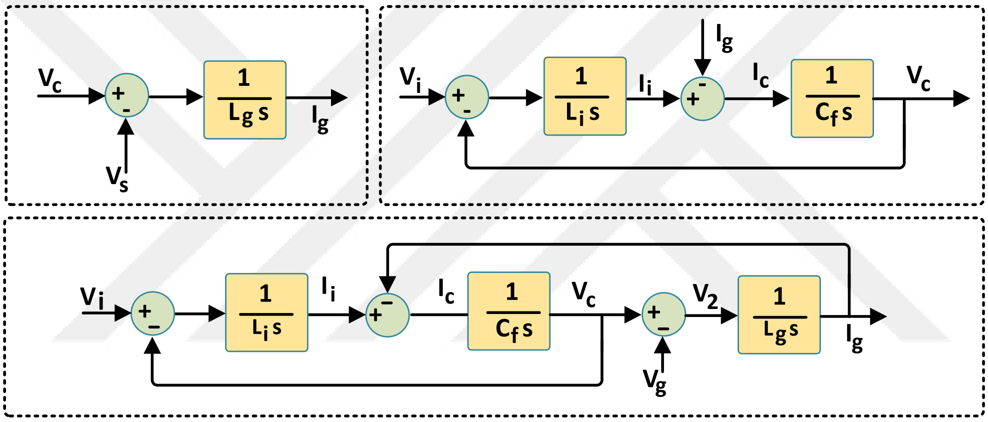

Figure 1.6. Block diagrams of single L, LC and LCL filters

According to transfer functions of the filters, Bode diagrams are plotted as shown in Figure 1.7. Bode diagrams are obtained with same inductance values. It can be seen from the figure that the filters have attenuations with -20 dB/dec, -40 dB/dec and -60 dB/dec, respectively. LC and LCL filter have resonance peaks as mentioned above. LC filter resonance frequency is smaller than LCL filter, which approximates lower limit of the resonance frequency.

$$G_{Vi \to Ig}(s) = \frac{I_g}{V_i} = \frac{1}{L_g s} \qquad (1.4)$$

$$G_{Vi\rightarrow Vc}(s) = \frac{V_c}{V_i} = \frac{1}{L_i C_f s^2+1} \tag{1.5}$$

$$G_{Vi\rightarrow Ig}(s) = \frac{I_g}{V_i} = \frac{1}{L_i L_g C_f s^3+(L_i+L_g)s} \tag{1.6}$$

$$w_{res,LC} = \frac{1}{\sqrt{L_i C_f}} \tag{1.7}$$

$$w_{res,LCL} = \sqrt{\frac{L_i+L_g}{L_i L_g C_f}} \tag{1.8}$$

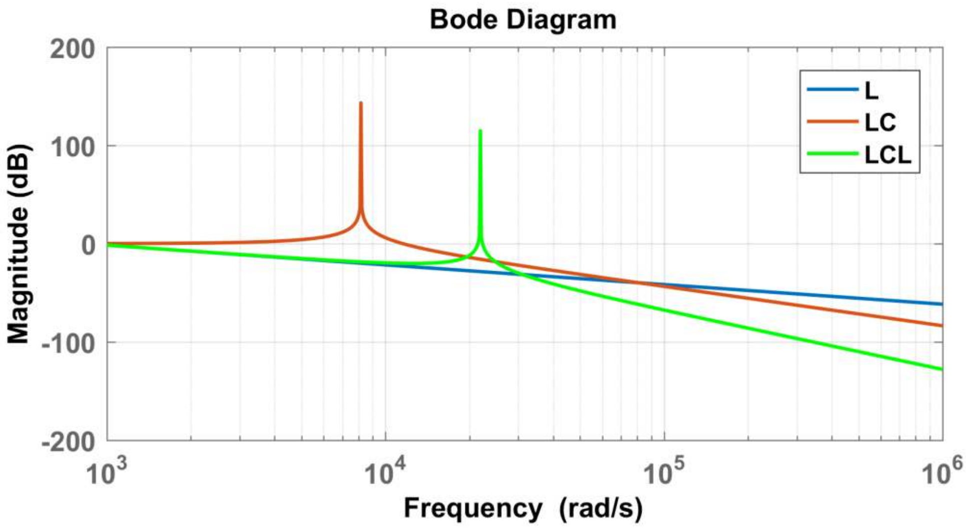

Figure 1.7. Bode diagrams of single L, LC and LCL filters

1.3. Motivation of Thesis

The growing application of grid-connected VSIs brings about distortion issues because of high frequency ripple components. Power electronics based VSIs including SAPF, STATCOM and another grid-connected VSIs generate harmonic ripple components at switching frequency and multiples of switching frequency. In electric power systems, power quality phenomena occurs due to these harmonic components. Meanwhile, the severity ratio of the switching harmonics have increased in recent years with the rising power of the grid-connected VSIs. To mitigate or eliminate the switching ripple harmonics because of the grid-connected VSIs, interfacing filters are applied between VSI and PCC as mentioned in previous section.

LCL filter, the most famous interfacing filter type, has an excellent attenuation benefit of the high frequency components. Due to this benefit, LCL filter has prominent applications with the grid-connected VSIs, likewise it is used with SAPF system. Although LCL filter has been examined and analyzed by the engineers and researchers over twenty years for the grid-connected VSIs, it has almost ten year history for application with SAPF.

The most crucial adversities in front of application of LCL filter with SAPF are the resonance phenomena and the wide control bandwidth of SAPF, which is 1.2-1.5 kHz. These obstacles lead to the complexity of the filter design and system controller. In order to overcome these issues, researchers have recently focused on the filter design for SAPF and the development of resonance damping techniques by considering SAPF system efficiency and harmonic compensation performance.

1.4. Research Objectives and Contributions

In this thesis work, a laboratory prototype of SAPF with LCL filter that is capable to application of different damping methods is designed and implemented. The implemented prototype system is able to fulfil PD, AD and auxiliary converter based resonance damping methods. By this way, a small power rated auxiliary converter is designed and implemented with the prototype system. In the view of this thesis study, three-phase three-wire SAPF with LCL laboratory prototype is designed and constructed in order to compensate the harmonic components of nonlinear load group up to 15A. The installed nonlinear load groups include three six pulse bridge rectifiers with 5kVA each load. Besides, the implemented auxiliary converter prototype is designed to suppress up to 10A resonance current. The design details of the prototypes are given in the following sections.

In the implemented system, Proportional-resonant (PR) controller in dq frame is proposed to track the harmonic reference currents generated by the nonlinear loads. LCL filter is designed to ensure the requirements stated previously. The details of filter design is presented following sections. According designed filter parameters, the damping methods are developed and applied. By this way, PD resistor value is chosen, the capacitor current feedback constant is determined and the controller of auxiliary converter is developed to suppress the resonance current. To acquire the resonant current for the controller of the auxiliary converter, a notch filter is used.

The overall design progress of power circuits of SAPF with LCL filter and auxiliary converter is given in detail in the following sections. The design of the power circuits and the performance of the controller under steady state and dynamic cases are examined and verified through simulation studies carried out using MATLAB/Simulink simulation environment and the experimental study results.

The primary contributions of this thesis work on the application and research areas of SAPF with LCL filter are summarized as;

- LCL filter is designed for SAPF to improve the attenuation of the switching ripple harmonics and to satisfy the standards.
- A selective harmonic elimination based on PR controller is conducted for SAPF with LCL filter.
- Three damping methods for LCL filter resonance are applied, analyzed and compared with respect to power losses, damping performance, system stability and attenuation of switching ripple harmonics.
- An auxiliary converter based active damper is proposed for SAPF with LCL filter and a design is fulfilled for the auxiliary converter.

- Open loop and closed loop transfer functions of SAPF with LCL filter system are constituted for three damping cases and their stability analysis are realized through Bode plots.
- A comprehensive design approaches for SAPF with LCL filter and CBAD are performed through theoretical methods and simulation studies.
- The proposed design approaches and controller of SAPF and CBAD are supported with comprehensive experimental results.

1.5. Thesis Outline

The organization of the thesis is as follows;

- In Chapter 2, a comprehensive state of art consisting of LCL filter application with SAPF and resonance damping methods for LCL filter is presented. The studies of SAPF with LCL filter are given in detail. Besides, the damping methods applied to grid-connected VSI are introduced.
- In Chapter 3, the main power circuits and operation principles of SAPF and CBAD are explained. The control algorithms of SAPF and CBAD are described in details. Different damping methods are presented including conventional simple resistor PD method and capacitor current feedback AD method. An auxiliary converter based damping method is proposed for SAPF with LCL filter. The theoretical stability analysis are performed by Bode plots. Besides, the calculations of power losses for PD and auxiliary converter are given.
- In Chapter 4, design guides and implementations of SAPF with LCL filter and CBAD are introduced. The design requirements are specified according to laboratory applications. The design of both prototypes are

provided in terms of theoretical and simulation cases. Furthermore, the design of the electronic control cards, based on digital signal processor (DSP), are presented.

- In Chapter 5, comprehensive experimental studies of SAPF with single L filter and LCL filter applying three damping methods are performed. The design approaches of LCL filter and damping methods are verified through experimental results. A comprehensive discussion of damping methods is also presented with various parameters.
- In Chapter 6, a summary of this thesis work is introduced with general conclusions obtained from experimental results. The main contributions of the thesis are emphasized. Additionally, future work proposals of this thesis study are described.

2. STATE OF ART

In recent years, LCL filters have found common applications with the grid-connected VSIs. Thus, in this section, progresses in damping methods applied to LCL filter in the grid-connected VSI and LCL filter applications in SAPF are presented. A research that also shows the number of publications about LCL filter gives the number of studies published until 2015 as illustrated in Table 2.1 (Buyuk et al., 2016). It is seen from the table that the research has been increased every year, demonstrating the importance of LCL filter in literature.

Table 2.1. The number of published papers until 2015

Year	2000-2004	2004-2007	2008	2009	2010	2011	2012	2013	2014
Study Number	18	49	30	34	40	49	75	106	110

2.1. Review of Damping Methods for LCL Filter

Even though great switching harmonic attenuation performance, LCL filter has a resonance issue that must be taken into consideration. The resonance damping methods are mainly classified into three different parts, which are passive damping (PD), active damping (AD) and converter based active damper (CBAD). PD methods are performed by additional adding passive components like resistor, inductor and capacitor to LCL filter. AD methods are fulfilled through modifying the controller algorithm. Lastly, in CBAD methods, an auxiliary converter is used to damp the resonance problem. Each methods have their benefits and drawbacks in terms of power losses, implementation cost, and damping and controller performances.

PD methods are performed by using extra passive components and categorized in three main parts such as series PD, parallel PD and complex PD methods. Figure 2.1 shows various passive damping method schemes.

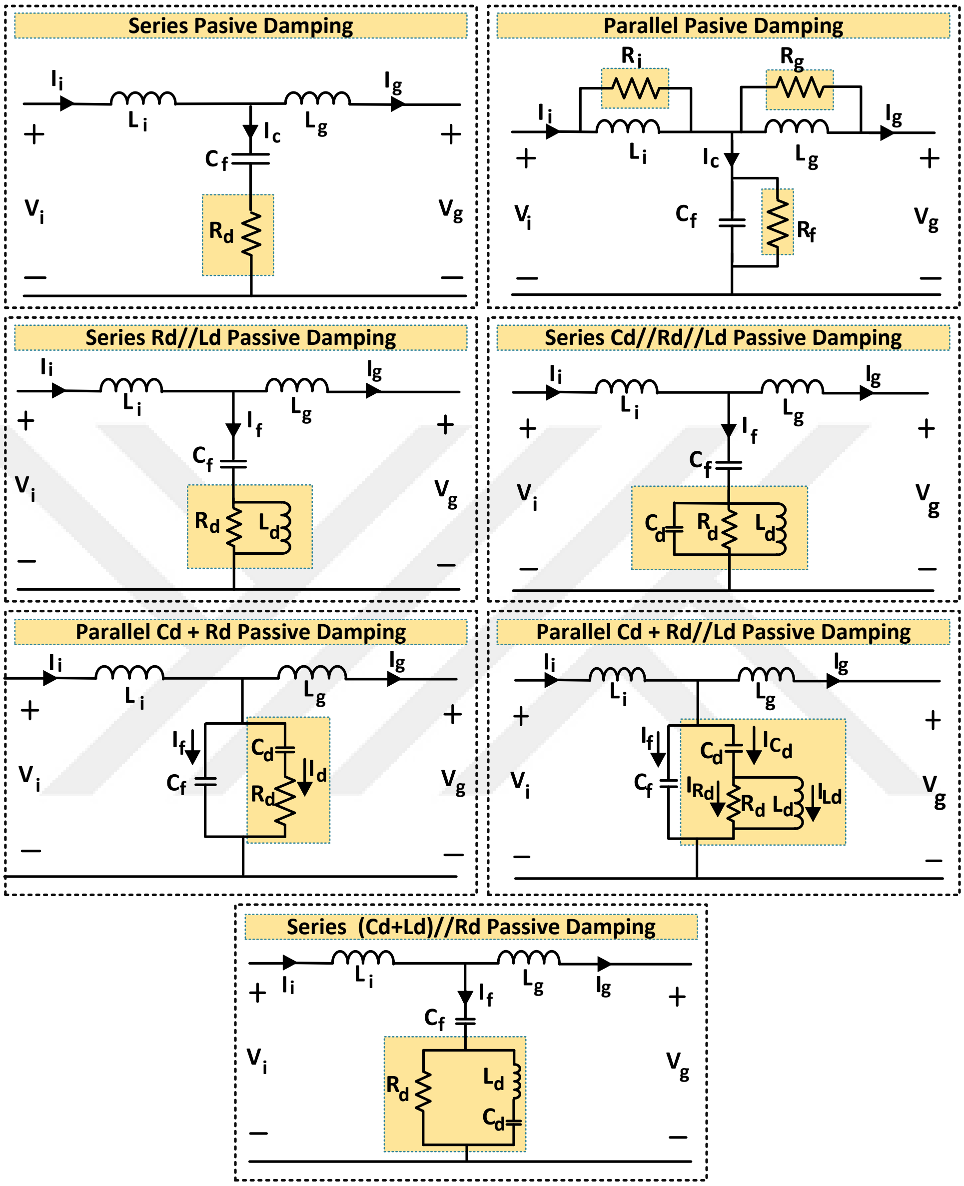

Figure 2.1. Circuit schemes of LCL filter with PD methods

The earlier PD method in literature is performed by adding simple resistor. This resistor can be connected either in series with the filter capacitor or parallel with filter inductors/capacitor (Guo et al., 2010; Pena-Alzola et al., 2013). The series connected PD method is the most common used PD technique to damp LCL filter resonance. Thus, this method is investigated experimental in this thesis work. The details of this method is given in the following section. However, series resistor PD method has power losses that decreases the overall efficiency of the system. To reduce the power losses on the damping resistor, complex PD methods are applied in literature by adding inductor or capacitor in series and/or parallel to the damping resistor. An inductor is connected in parallel with the damping resistor to lessen the fundamental frequency losses (Buyuk et al., 2016). The inductor performs lower impedance than the damping resistor at fundamental frequency, which causes the fundamental current flowing on the inductor. On the other side, a capacitor is paralleled to the damping resistor-inductor components to decrease the power losses stemmed from high frequency harmonics (Pena-Alzola et al., 2013). This capacitor shows lower impedance than the damping resistor at high frequencies, resulting high frequency harmonics flowing on this capacitor instead of the damping resistor. Another method to decrease the damping losses is to put shunt $C_d + R_d$ branch with the filter capacitor. In this method, the total value of the filter capacitor and branch capacitor is same with single capacitor situation. The values of these capacitors are proposed to be chosen half of single capacitor case (Channegowda and John, 2010). Furthermore, to decrease further power losses in previous method, $C_d + R_d//L_d$ branch is connected in parallel with the filter capacitor (Balasubramanian and John, 2013). By adding additional inductor parallel with the damping resistor, the component at resonance frequency is passed through dissipative components, thus reducing losses of resonant current. The last complex PD method in literature is performed by changing the filter capacitor as C-type filter, series $(C_d + L_d)//R_d$ method (Liu et al., 2013). In this method, the series $(C_d + L_d)$ branch is adjusted to the switching frequency. By this way, the switching harmonics are mitigated more effectively than previous PD methods.

To eliminate PD power losses, AD methods are proposed in literature. AD methods are realized by configuring the system control algorithm. However, making configuration in control algorithm results in a more complicated system. Similar to

PD methods, AD methods are divided into three main categories (Buyuk et al., 2016). These categories are single-loop AD, multi-loop AD and complex AD methods. Single-loop AD methods are mainly based on using digital filter and do not use additional feedback loop, where an additional measurement point is not necessary. In multi-loop AD methods, an extra point is measured and feed backed in controller loop, increasing the system cost and complexity. Another way for AD is to use complex control algorithms. Moreover, each category consists of sub-category as illustrated in Figure 2.2.

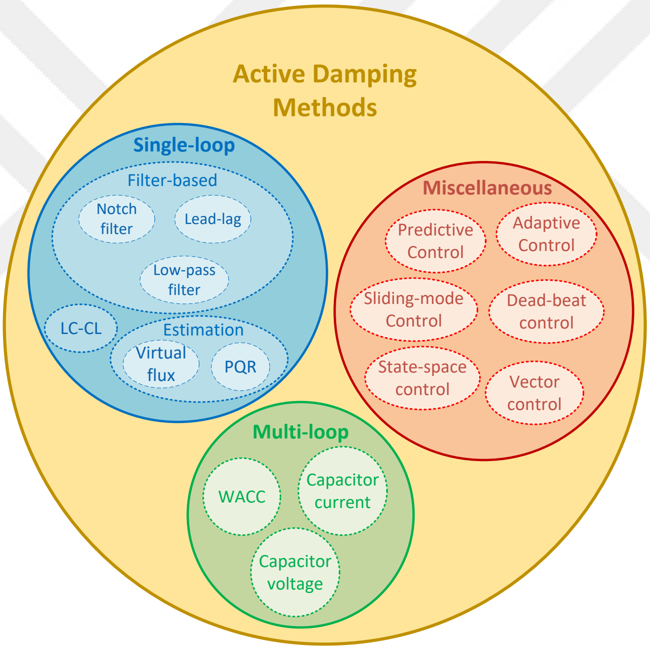

Figure 2.2. Classification of AD methods

The single-loop, also called sensorless, AD methods do not require additional sensing point. These methods are also classified as filter-based, splitting capacitor (LC-CL) and estimation based methods. The filter based AD methods are the most widespread investigated methods among the single-loop AD methods. The block diagram of the filter-based AD method is demonstrated in Figure 2.3. As seen from the figure that a filter G_d is added in the control algorithm. Low-pass, lead-lag and notch filters are a few types applied in literature (Dannehl et al., 2011; Pena-Alzola et al., 2014; Pena-Alzola et al., 2014). Another single-loop AD method is performed by splitting the capacitor filter and use the current passing among two capacitor as feedback current to control (Balasubramanian and John, 2013). It is also named as LC-CL AD method. The block diagram of splitting capacitor AD method is shown in Figure 2.4. The total capacitor value is not changed. However, the ratio of split capacitors should be determined carefully. This ratio is determined to be as $L_g/(L_i + L_g)$. There are also some methods based on estimation of capacitor current through virtual flux and pq theory (Malinowski et al., 2005; Hu et al., 2013). The single-loop AD methods, however, are affected from the variation of parameter in the system. To overcome this issue and improve the performance, multi-loop AD methods are proposed in literature.

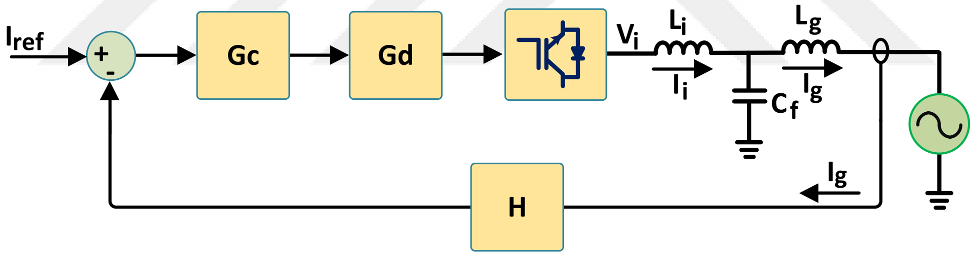

Figure 2.3. Block diagram of filter-based AD method

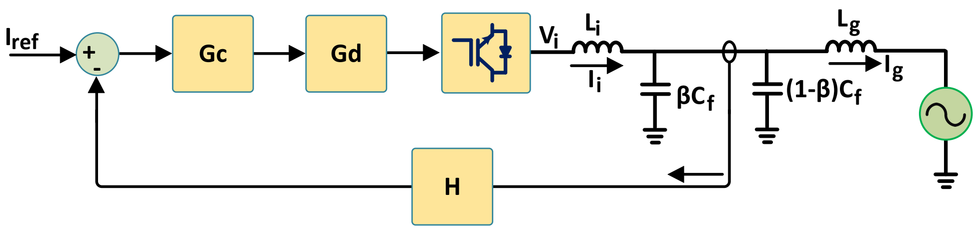

Figure 2.4. Block diagram of splitting capacitor AD

In multi-loop AD methods, compared with single-loop AD, an additional point is measured and added in control loop, thus, the system is enhanced to the system parameter variations. This additional loop can be the inverter-side current, the capacitor current or the capacitor voltage. According to measured point, multi-loop AD methods are classified as capacitor current feedback, capacitor voltage feedback and weighted average current control (WACC) methods. The capacitor current feedback method, also called virtual resistor method, is the most commonly applied method in literature (Bao et al., 2014; Jia et al., 2014). This method is one of the investigated method in the experimental study for SAPF with LCL filter. The block diagram of the capacitor current feedback AD method is shown in Figure 2.5. It is seen from the figure that the measured capacitor current is measured and feed backed in control loop. The measured current is multiplied with a function before adding in control loop (Pan et al., 2014). This function is usually a constant, determined according to system parameter. The higher constant value provides better resonance damping. On the other hand, further increase of the constant may cause high phase shift and unstable system condition (Buyuk et al., 2016). Another multi-loop AD method is performed by measuring the capacitor voltage and adding in control loop (Dannehl et al., 2010). The capacitor voltage feedback AD method is demonstrated in Figure 2.6. It is seen that the capacitor voltage, similar to capacitor current feedback method, is multiplied with a function before adding in the control loop. This function is offered to be derivative to ensure resonance damping. Another distinct multi-loop AD method is WACC as shown in Figure 2.7 (Shen et al., 2010; He et al., 2013). In this method, inverter-side current is measured in addition grid-side current and their weighted average is used as feedback control signal. The transfer function of LCL filter is reduced to behave as single L filter if the weighted average ratio is selected as $L_g/(L_i + L_g)$.

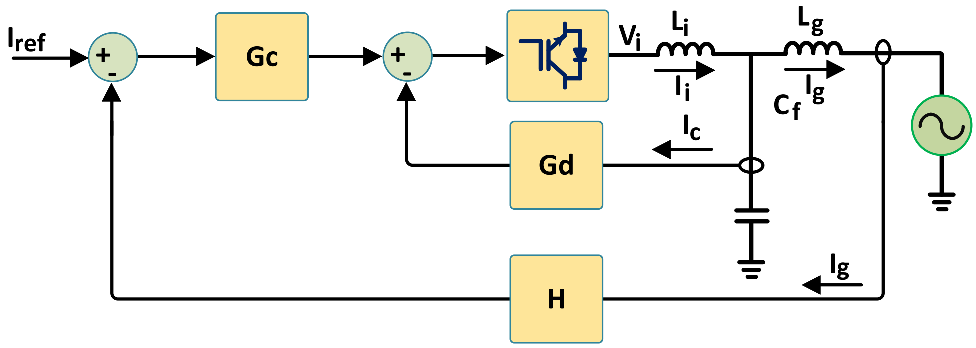

Figure 2.5. Block diagram of capacitor current feedback AD method

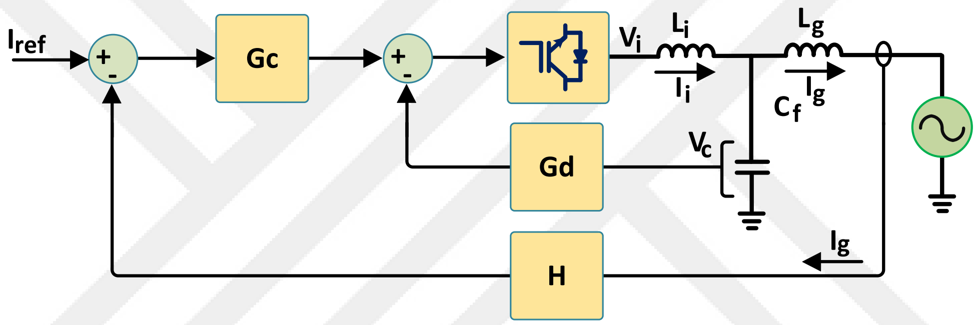

Figure 2.6. Block diagram of capacitor voltage feedback AD method

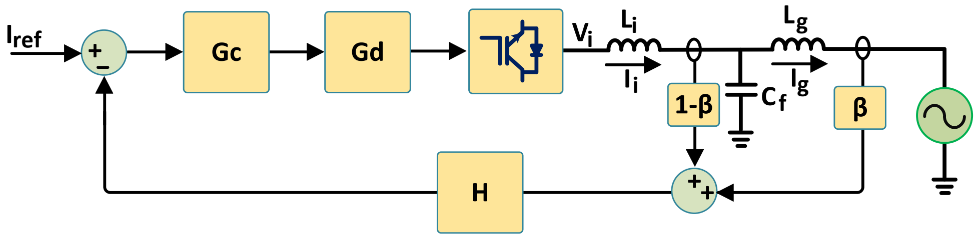

Figure 2.7. Block diagram of weighted average current control AD

PD methods have power losses disadvantage and AD methods have drawback of reducing controller bandwidth. In order to decrease damping power losses due to PD and eliminate disadvantage of AD in controller bandwidth, CBADs are proposed in literature. CBADs are based on power electronics system, VSIs. They operate dynamically to suppress the resonance problem through demonstrating virtual resistor at the resonance frequency. Moreover, they have low power implementation and high control bandwidth because of working only for resonance frequency. It is worth nothing that CBAD methods propose flexible and efficient damping property. In literature, a few CBAD topologies are proposed. The CBAD topologies used in literature are illustrated in Figure 2.8. The first topology is performed by connecting a VSI interfaced with single L filter to PCC (Leblanc et al., 2013; Wang et al., 2014; Wang et al., 2014). This structure is similar with SAPF system. The resonance frequency is obtained by using filter and applied as reference signal for current control algorithm. Instead single L filter, LCL filter is preferred to reduce switching ripple harmonics of CBAD (Jia et al., 2018). The second topology is performed by replacing LC filter instead of single L filter (Wang et al., 2015; Bai et al., 2016; Bai et al., 2017). This topology has smaller VSI rating in comparison to first topology since the capacitor holds the fundamental component. The first and second topologies can be used to damp multiple resonance frequencies of parallel connected VSIs. The third and fourth topologies are fulfilled by connecting CBAD in series to the filter capacitor. Considering that the filter capacitor causes the resonance frequency, the third and fourth structures come into prominence. The third topology is similar with series APF topology (Usluer and Hava, 2014). It uses a VSI, LC filter and series transformer with the filter capacitor. The last topology is done by connecting VSI with single L filter to the capacitor leg (Usluer and Hava, 2014). This topology has smaller implementation cost and size in comparison to third topology. Thus, this topology is investigated in experimental studies.

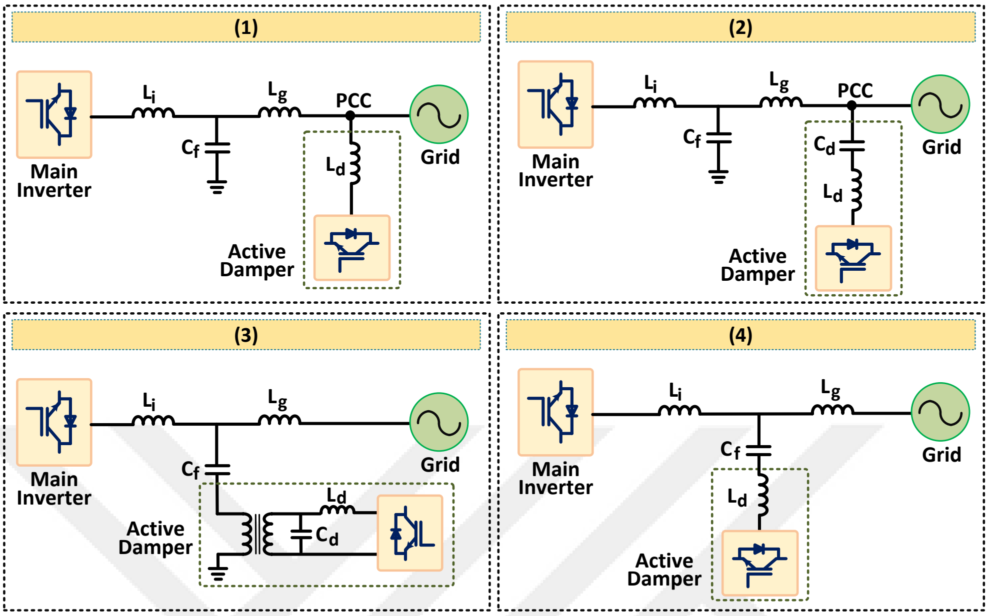

Figure 2.8. Different CBAD topologies in literature

2.2. Review of LCL Filter Applied with SAPF

LCL filter has found wide penetration into the grid-connected VSI in order to achieve great attenuation of SRHs as mentioned in previous Section. Because of its powerful advantages, LCL filter has induced wide interest among researchers in recent years to apply and examine as output filter of SAPF. Likewise, some companies have used LCL filter with their SAPF products. The application of LCL-filter interfaced SAPF puts forward the discussion of the design and resonance issues of LCL-filter owing to wider operating bandwidth range of SAPF. SAPF has control bandwidth between the grid fundamental frequency and up to 50^{th} harmonic components to eliminate harmonic currents. The wide control bandwidth demonstrates a narrow bandwidth for LCL-filter design and resonance suppression.

In literature, several studies have been published about LCL filter interfaced SAPF. These papers in general focus on the filter design for SAPF and apply simple series PD method. Rarely, AD methods are examined and assessed in a few studies for SAPF with LCL filter topology. However, CBAD systems have not yet been implemented and analyzed for SAPF with LCL filter. In some studies, Zeng et al. (2010), Tang et al. (2012) and Liu et al. (2014), the design of LCL filter has carried out for application with SAPF. Although the filter parameters are calculated similar to conventional grid-connected VSI, the minimum resonance frequency value is offered to be 1.2-1.6 times of the maximum compensated harmonic frequency (Zeng et al., 2010). Thus, the filter parameters are determined by trial and error until to satisfy specified design limits. Furthermore, Tang et al. (2011) and (2012) prefer to assess the design of the filter and controller simultaneously through applying capacitor current feedback AD method. By this means, interaction of resonance damping and compensation controller with filter design is taken into consideration. A distinct design of LCL filter based on graphical analysis is proposed in (Liu et al., 2014). In this study, Liu et al. (2014), an optimized filter design is fulfilled through considering relationship between the filter parameter and SAPF performance and illustrating this relationship on a graph. Likewise, the trial and error is prevented by this method with observing suitable area on the graph. The design of LCL filter gets more complexity once the switching frequency varies. To overcome this issue, Bina and Pashajavid (2009) proposes a design procedure for LCL filter under variable switching frequency. Pettersson et al. (2006) presents the design of LCL filter for four-wire SAPF by considering frequency model of inductor (fourth-order series Foster equivalent circuit), where this model increase the accuracy of the frequency model analysis. Fang et al. (2017) distinctly offers the design of series resonant parallel to LCL filter capacitor for single-phase half-bridge SAPF. In this study, Fang et al. (2017) adjusts the series resonant (LC) circuit frequency to the switching frequency to ensure more effective elimination of harmonic ripple at the switching frequency. In most of studies in literature, Vodyakho and Mi (2009), Han et al. (2017), Buyuk et al. (2015) and Büyük et al. (2019), LCL filter has preferred because of superior benefits and PD technique is exploited to suppress the resonance in these studies due to its simplicity. Instead, Buyuk et al. (2015) examines and compares performances and damping power losses of various PD methods for SAPF with LCL filter. On the other side, Vodyakho and Mi (2009) presents application of LCL filter with multi-level VSI in SAPF systems, where the simple resistor PD method is applied to damp the resonance. AD methods are examined for SAPF with LCL filter because of eliminating power losses released in PD methods. Predictive control method is utilized to achieve zero-error current tracking and to overcome the resonance problem in (Wojciechowski, 2010). Xie et al. (2012) uses a band-stop filter at resonance frequency in the control loop. The depth of the band-stop filter is adjusted through a constant. The resonance damping is provided by using inverter-side current as proportional feedback inner loop control in (Tian and Jiang, 2013), which has inherent damping characteristic. Similarly, Yuan and Jiang (2016) applies inverter-side current in control loop and subtracts the inverter-side current multiplied with a constant from the error signal. Besides, Yang and Yang (2018) also use inverter-side current control by taking into consideration phase delay and amplification in high order compensation harmonics. This study has further improved via considering design of current controller in (Yang and Yang, 2019). Another study on AD method is performed in (Wang et al., 2014) by using sample delay with first order low-pass filter. Ge et al. (2017) conducts and analyses two AD strategies such as capacitor current feedback and notch filter based. Buyuk et al. (2018) proposes an adaptive notch filter based AD method for SAPF with LCL filter in order to ensure flexible resonance damping against the grid inductance variations, hence it is helpful for increasing the system stability under the impedance variations. Li and Jiang (2013) examine stability of system using the capacitor current feedback AD strategy through determining the feedback constant with Root locus method. Tang et al. (2011) investigates the damping performance of AD methods such as capacitor current/voltage and grid-side current feedback techniques by using discrete state-space model of the system. Their damping abilities are determined in terms of the ratio of the resonance frequency to switching frequency. In (He et al., 2017), LCL filters are applied with dual interfacing VSIs, while one of the VSIs is used to eliminate voltage harmonics, the second VSI is installed to compensate harmonic currents. In both VSIs, inverter-side currents are employed to perform resonance damping. Zou et al. (2014) performs application of LCL filter for multifunction grid-connected inverter in distributed systems including fundamental and harmonic components injection. Equivalent models of multifunction mode and normal power delivery mode are developed through Thevenin/Norton models. Miscellaneous passive and active damping methods are investigated and analyzed by Routimo and Tuusa (2007) and Zhao and Chen (2009). Routimo and Tuusa (2007) examine the damping methods by taking foster model of LCL filter and controller into consideration. On the other side, Zhao and Chen (2009) compare several kind of PD and AD methods with respect to damping performances and power losses. Xu et al. (2016) proposes double resonant LCL filter for SAPF aiming to reduce switching frequency harmonics effectually while not decreasing the controller bandwidth. Double resonant LCL includes two series LC circuits parallel with the series filter capacitor – damping resistor. The resonant frequencies of the series LC circuits are tuned to the switching frequency and double switching frequency.

3. OPERATING PRINCIPLES AND CONTROL

3.1. Circuit Configuration of the SAPF System

The power circuit topology of SAPF with LCL filter mainly consists of VSI, dc link capacitor bank and output LCL filter as demonstrated in Figure 3.1. VSI is the main part of SAPF and it maintains harmonic injection and harmonic insolation between the grid and load. VSI is formed from three-leg inverter topology consisting of six switching devices. IGBTs are the most commonly utilized switching devices in high power VSIs because of satisfying adequate high switching frequency operation. IGBTs are suitable to use in high power SAPF applications.

The dc link capacitor bank connected in parallel with VSI is used to store the energy that requires for harmonics compensation. The required energy of the dc link is instantaneously provided from the grid through VSI. Therefore, an additional dc link power supply is not required for harmonics compensation requirement of SAPF system. The dc link voltage is kept higher than the peak value of the PCC voltage in order to be capable of harmonics injection.

In earlier SAPF topology, single L filter was used as switching ripple filter. The inductance value must be kept higher to sufficiently reduce the switching ripple. Increment of the inductance value requires higher dc link voltage to control active power flow and injection of harmonic currents by SAPF. In recent years, LCL filter has usually been preferred with SAPF (Yang and Yang, 2018; Büyük et al., 2019; Yang and Yang, 2019). The switching ripple harmonics flow on the capacitor because of too low impedance at high frequencies. Thus, the switching ripple harmonics are significantly reduced and prevented to flow the grid. By means of this advantage, the lower filter inductance value can be used and the dc link voltage is kept in optimal value. Moreover, the switching power losses are also diminished thanks to reduced dc link voltage. LCL filter, on the other hand, has resonance disadvantage which may drift the SAPF to instable state. The conventional resonance damping techniques and the proposed method will be mentioned in next section in detail.

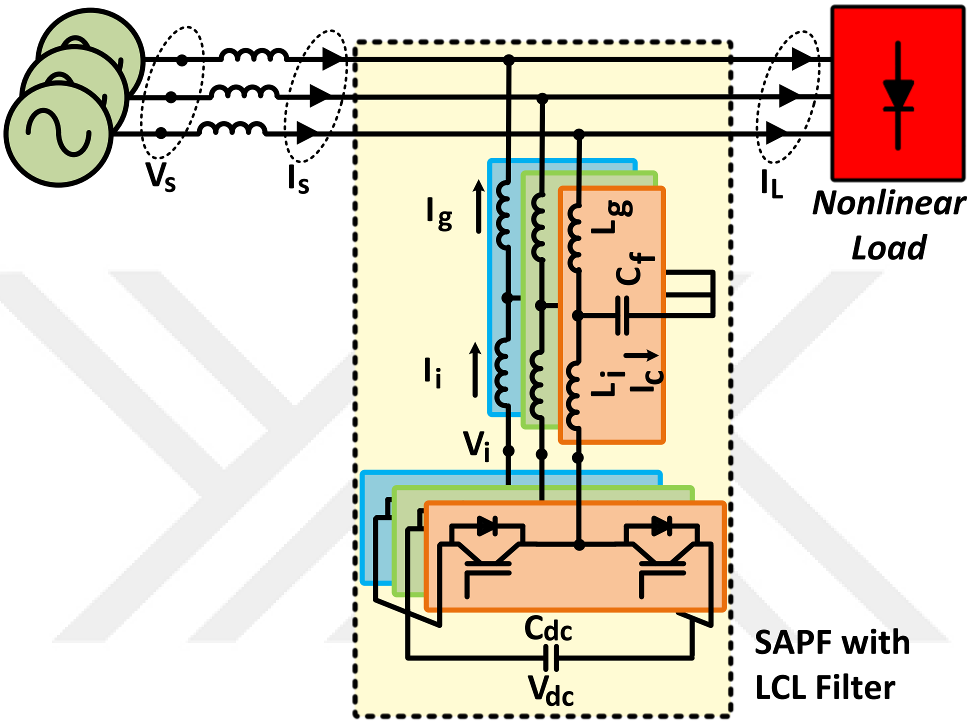

Figure 3.1 Power circuit configuration of SAPF with LCL Filter

3.2. Control Method and Operation of SAPF

Over the years, many control methods are presented for SAPFs in literature. The generalized controller diagram of SAPF is shown in Figure 3.2. The control block diagram of SAPF with LCL filter is demonstrated in Figure 3.3. The controller of conventional SAPFs can be divided into three main parts: reference generation, dc link voltage controller and harmonics current controller. The dc link voltage controller is necessary for providing and keeping the required dc link voltage in constant level to achieve harmonics compensation. The reference signal I_{ref} consists of the dc link current reference $I_{dc,ref}$ and harmonic components of load I_{Lh}. The reference currents are obtained in the reference calculation block through the sum of harmonic components and the reference dc current. Current controller maintains the generation of reference current by the inverter accurately.

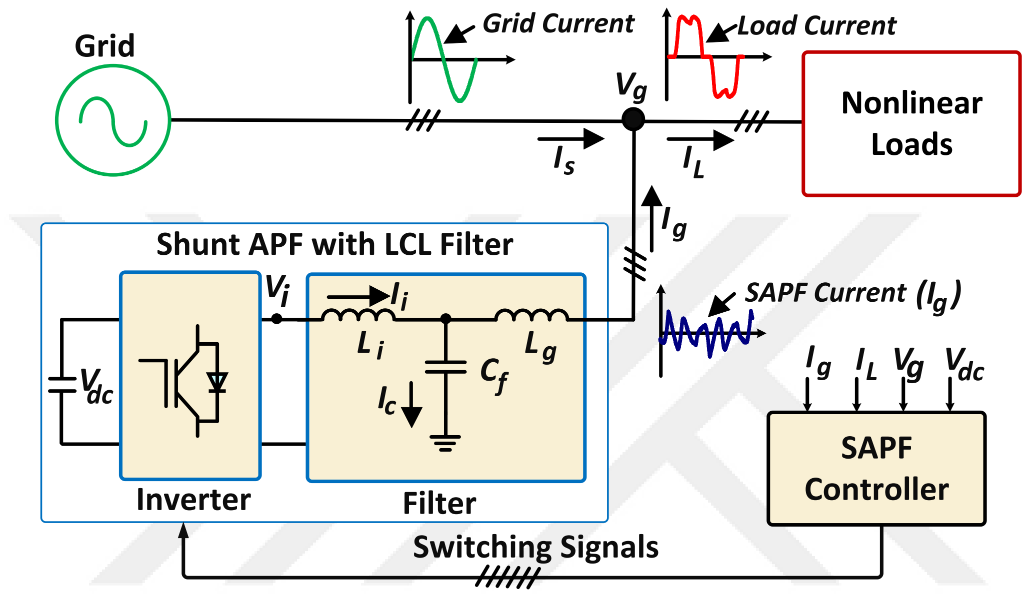

Figure 3.2. Basic block diagram of SAPF with LCL filter

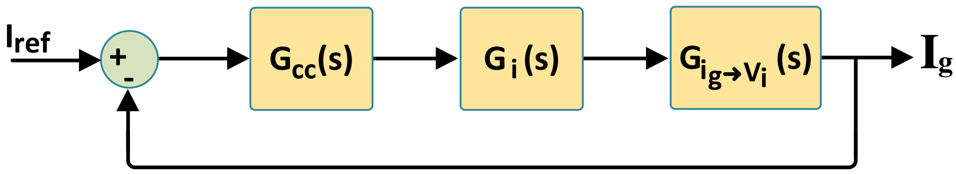

Figure 3.3. Control block diagram of SAPF with LCL filter

3.2.1. Harmonics Current Reference Generation

The generation of harmonic current references is quite important to satisfy effective compensation of harmonics. To achieve an effective compensation, the harmonic current references should be computed accurately with short time (Asiminoaei et al., 2007; Bhattacharya et al., 2009). The miscellaneous reference generation methods have been applied in literature. The reference harmonic components can be acquired through several methods which constitute time domain methods and frequency domain methods as illustrated in Figure 3.4 (Asiminoaei et al., 2005).

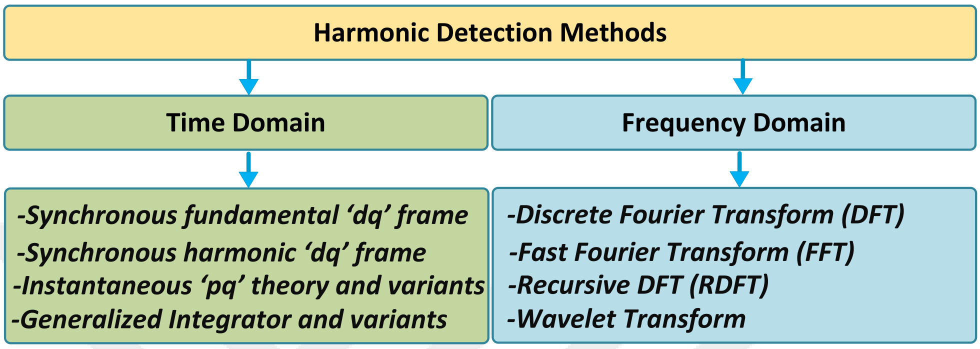

Figure 3.4. Harmonic detection methods

The frequency-domain techniques are usually based on Fourier analysis such as DFT, FFT, and RDFT. Frequency-domain based harmonic generation methods require more computations burden that needs high specified microcontroller. Additionally, frequency-domain based methods has some restriction. In the design of APF, the aliasing effect must be taken into consideration. Synchronization of fundamental frequency and the sampling instant should be satisfied. In order to avoid this problem, antialiasing filter has been applied to verify the synchronization (Bhattacharya et al., 2009).

On the other hand, time-domain approaches are mainly divided into three methods; "dq-frame (or SRF)", "pq-theory" and "generalized integrator". The time-domain reference generation techniques have less mathematical calculation and provide higher speed compared with frequency-domain approaches (Asiminoael et al., 2007). Dq and pq based methods hold comprehensive usage thanks to their simplicity and maintaining powerful performance and stability. In this thesis, a novel harmonic reference generation method based on pq-theory is improved. The detail of dq frame and improved pq theory methods are given below. During experimental studies dq frame based harmonic generation method is preferred because resonant current controller requiring less computation in dq frame is used to control harmonic signals.

Clarke and Park Transformations

Clarke and Park transformations are used to represent three phase circuits into space vector in order to simplify the analysis and reduce the calculation complexity. Clarke transformation, also known as αβ stationary frame transformation, represents the three phase voltages and/or currents in space vector rotating with angular velocity, namely α and β signals are ac signals (Tan, 2015). On the other hand, Park transformation, also known as dq rotating frame transformation, represents rotation of reference frame of three phase signals, namely d and q signals are dc signals.

The three phase balanced signals are expressed as Eq. 3.1. y refers to voltage (v) or current (i) signals. Y_m is the magnitude of signal and $\emptyset_A$, $\emptyset_B$ and $\emptyset_C$ are the phase angles of A, B and C phases, respectively.

$$y = \begin{Bmatrix} y_A = Y_m \sin(wt + \emptyset_A) \\ y_B = Y_m \sin(wt + \emptyset_B) \\ y_C = Y_m \sin(wt + \emptyset_C) \end{Bmatrix} \tag{3.1}$$

Where,

$$\emptyset_B = \emptyset_A - 2\pi/3$$
$$\emptyset_C = \emptyset_A - 2\pi/3$$

In Clarke transformation, three phase signals are transformed into α (real) and β (imaginary) components. The vectorial representation of three phase abc to αβ transformation is shown in Figure 3.5. The mathematical notation of αβ stationary frame transformation is given in Eq. 3.2. The αβ frame signals can be obtained by the transformation in Eq. 3.3. Inverse Clarke transformation can be realized in Eq. 3.4.

$$Y_{\alpha\beta} = Y_\alpha + jY_\beta = \left(Y_A + Y_B e^{j2\pi/3} + Y_C e^{-j2\pi/3}\right) \tag{3.2}$$

$$\begin{bmatrix} Y_\alpha \\ Y_\beta \\ Y_0 \end{bmatrix} = T_{abc\to\alpha\beta} \begin{bmatrix} Y_A \\ Y_B \\ Y_C \end{bmatrix} \tag{3.3}$$

$$\begin{bmatrix} Y_A \\ Y_B \\ Y_C \end{bmatrix} = T_{\alpha\beta\to abc} \begin{bmatrix} Y_\alpha \\ Y_\beta \\ Y_0 \end{bmatrix} \tag{3.4}$$

Where,

$$T_{abc\to\alpha\beta} = C \begin{bmatrix} 1 & -\frac{1}{2} & -\frac{1}{2} \\ 0 & \frac{\sqrt{3}}{2} & -\frac{\sqrt{3}}{2} \\ \frac{1}{2} & \frac{1}{2} & \frac{1}{2} \end{bmatrix} \text{ and } T_{\alpha\beta\to abc} = \frac{1}{C} \begin{bmatrix} \frac{2}{3} & 0 & \frac{2}{3} \\ -\frac{1}{3} & \frac{\sqrt{3}}{3} & \frac{2}{3} \\ -\frac{1}{3} & \frac{\sqrt{3}}{3} & \frac{2}{3} \end{bmatrix}$$

C is a constant and $\emptyset$ is the phase angle information of reference frame. When the constant C is selected as 2/3, the amplitude of d and q quantities is equal to peak value of three phase signals. In the case of constant selection is $\sqrt{2/3}$, power invariant form of expression is obtained. The constant is chosen as 2/3 in order to obtain magnitude quantities in dq frame (Tan, 2015).

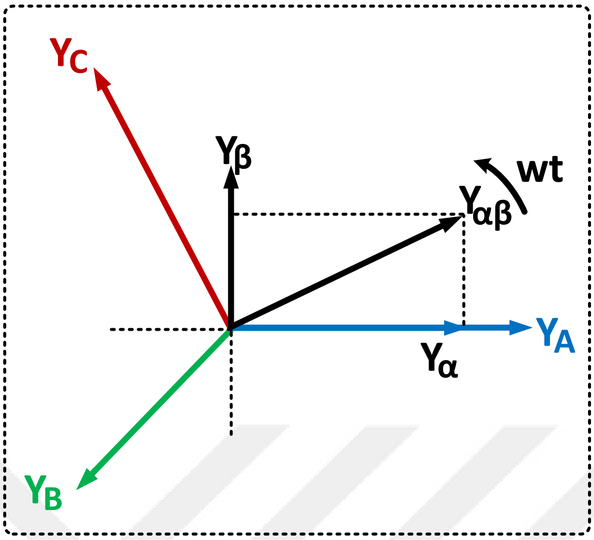

Figure 3.5. Vectorial representation of abc frame and αβ frame

In dq rotating frame, three-phase ac signals are transformed in direct (d) and quadrate (q) signals. The vectorial representation of three phase abc to dq transformation is shown in Figure 3.6. The mathematical notation of dq synchronous frame is given in Eq. 3.5. The dq frame signals can be obtained by the transformation in Eq. 3.6. The dq frame signals are converted to abc frame signals by applying inverse transformation given in Eq. 3.7 (Çetin, 2007; Terciyanlı, 2010).

$$Y_{dq} = Y_d + jY_q = \left(Y_A + Y_B e^{-j2\pi/3} + Y_C e^{j2\pi/3}\right) e^{-j\emptyset} \tag{3.5}$$

$$\begin{bmatrix} Y_d \\ Y_q \\ Y_0 \end{bmatrix} = T_{abc\to dq} \begin{bmatrix} Y_A \\ Y_B \\ Y_C \end{bmatrix} \tag{3.6}$$

$$\begin{bmatrix} Y_A \\ Y_B \\ Y_C \end{bmatrix} = T_{dq\to abc} \begin{bmatrix} Y_d \\ Y_q \\ Y_0 \end{bmatrix} \tag{3.7}$$

Where,

$$T_{abc\to dq} = C\begin{bmatrix} \cos(\emptyset) & \cos(\emptyset-2\pi/3) & \cos(\emptyset+2\pi/3) \\ -\sin(\emptyset) & -\sin(\emptyset-2\pi/3) & -\sin(\emptyset+2\pi/3) \\ \frac{1}{2} & \frac{1}{2} & \frac{1}{2} \end{bmatrix} \text{ and}$$

$$T_{dq\to abc} = \begin{bmatrix} \cos(\emptyset) & -\sin(\emptyset) & \frac{1}{2} \\ cos(\emptyset-2\pi/3) & -\sin(\emptyset-2\pi/3) & \frac{1}{2} \\ \cos(\emptyset+2\pi/3) & -\sin(\emptyset+2\pi/3) & \frac{1}{2} \end{bmatrix}$$

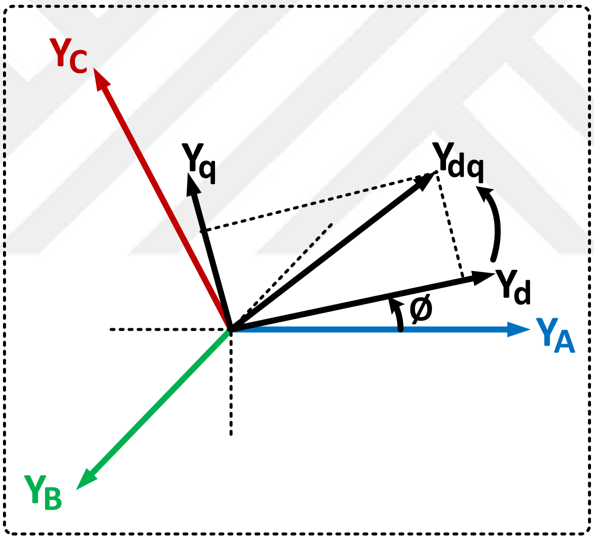

Figure 3.6. Vectorial representation of abc frame and dq frame

SRF Harmonic Extraction Method

SRF method, used to reduce calculations, is based on transformation of three-phase representations of voltages and/or current signals into dq rotating frame. The three-phase ac voltage and/or current signals are transformed into two dc variables d and q in the case of pure and balanced sinusoidal signals (Asiminoaei et al., 2007).

The block diagram of harmonic current generation through dq reference frame is presented in Figure 3.7. The measured three phase load currents are transformed into dq frame with the angle information of voltage fundamental signal. Since the transformation is performed by fundamental signal angle information, d and q invariants of fundamental signals are transformed into dc signal. On the contrary, d and q invariants of the harmonic signals are converted into ac signals. The harmonic signals in dq frame can be extracted via passing the dq frame signals through high-pass filter. Nevertheless, the large phase error may occur in ac components if using high-pass filter (Bhattacharya et al., 2009). Low pass filter does not cause phase error. Thus, to overcome the phase error problem, a low-pass filter is applied to decouple the dc signals in dq frame (Tan, 2015). Then, the decoupled dc signals are extracted from non-filtered dq frame signals to get harmonic signals. The harmonic signals in dq frame, then, are transformed into three phase harmonic current signals by using inverse transformation given in Eq. 3.7.

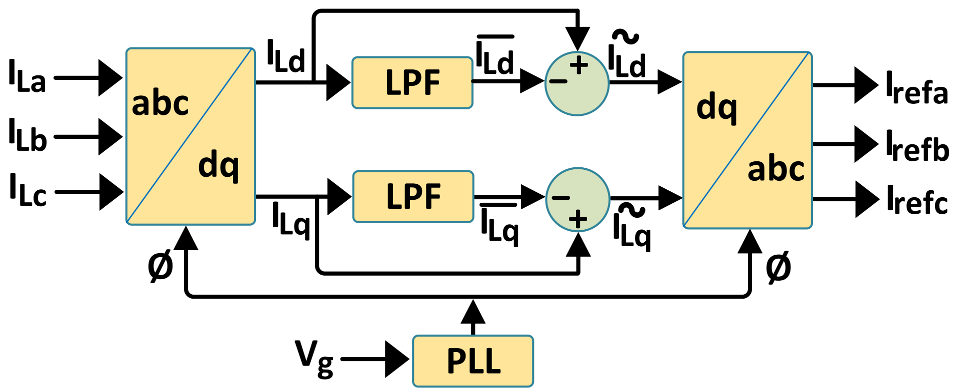

Figure 3.7. Dq reference frame based harmonic components extraction

Improved PQ Theory

During thesis study, a novel harmonic current extraction method is improved by using pq theory. The proposed method is based on virtual signal generation of voltage and current signals. Thus, the proposed method is named as VIS-IPT. The proposed method especially shows considerable performance under unbalanced grid conditions (Büyük et al., 2019).

In the proposed method, the three phase signals are written in polar and exponential formulation as below.

$$Y_x = Y_m \angle \emptyset_x = Y_m e^{j\emptyset_x}\,; x = A, B, C \tag{3.8}$$

In this method, each phase is considered as individual and virtual signals are generated for each phase signal. The real signal of phase-x is denoted as $Y_{x,a}$ given in Eq. 3.9. Then, two symmetrical virtual signals $Y_{x,b}$ and $Y_{x,c}$ are obtained.

$$Y_{x,a} = Y_m e^{j\emptyset_x} \tag{3.9}$$

Considering three balanced signals, virtual-b and -c signals are written as Eqs. 3.10 and 3.11. Virtual-b delays the real signal by 120^0 in this form. Instead, the virtual-b signal is rewritten as Eq. 3.12. By this form, the virtual-b signal is delayed 60^0.

$$Y_{x,b} = Y_m e^{j(\emptyset_x - 2\pi/3)} \tag{3.10}$$

$$Y_{x,c} = Y_m e^{j(\emptyset_x + 2\pi/3)} \tag{3.11}$$

$$Y_{x,b} = Y_m e^{j(\emptyset_x + \pi/3)} e^{-j\pi} = -Y_m e^{j(\emptyset_x + \pi/3)} \tag{3.12}$$

Virtual-c signal in Eq. 3.11 can be revised similar to virtual-b signal. The summation of real signal with its virtual signals equals to zero given in Eq. 3.13 because of balanced virtual signals. The virtual-c signal can be easily obtained by adding the real and virtual-b signal and multiplying with minus 1.

$$Y_{x,a} + Y_{x,b} + Y_{x,c} = 0$$
$$Y_{x,c} = -(Y_{x,a} + Y_{x,b}) \tag{3.13}$$

The block diagram representations of the real and virtual signals are shown in Figure 3.8. In addition, the geometrical representations of the real and virtual signals are demonstrated in Figure 3.9.

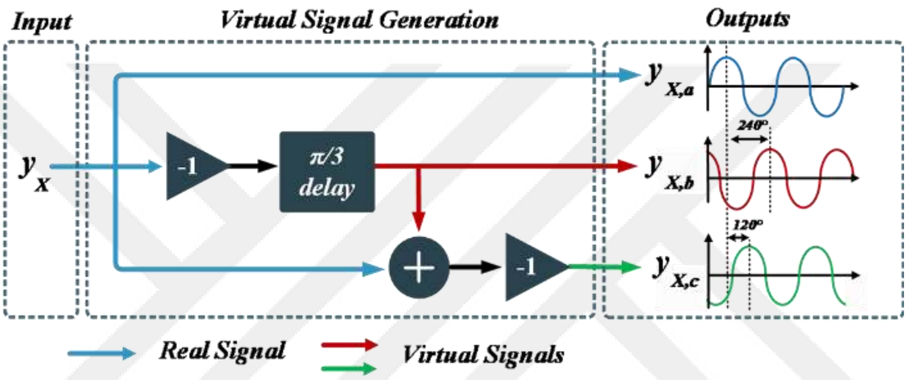

Figure 3.8. Block diagram of real and virtual signals

After generation of virtual signals, conventional pq theory is applied for each phase by considering individually. The instantaneous voltage and current components including real and virtual signals are written as in Eqs. 3.14 and 3.15. Additionally, instantaneous orthogonal voltage components are given in Eq. 3.16.

$$v_{x,abc} = [v_{x,a} \quad v_{x,b} \quad v_{x,c}]^T \tag{3.14}$$

$$i_{x,abc} = [i_{x,a} \quad i_{x,b} \quad i_{x,c}]^T \tag{3.15}$$

$$v_{xd} = \frac{1}{\sqrt{3}}\begin{bmatrix} v_{x,bc} \\ v_{x,ca} \\ v_{x,ab} \end{bmatrix} = \frac{1}{\sqrt{3}}\begin{bmatrix} v_{x,b} - v_{x,c} \\ v_{x,c} - v_{x,a} \\ v_{x,a} - v_{x,b} \end{bmatrix} \tag{3.16}$$

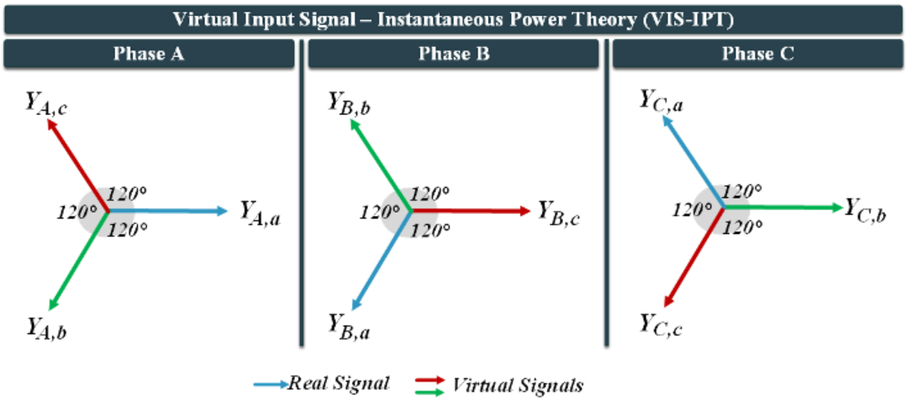

Figure 3.9. Geometrical representations of real and virtual signals

The generated balanced voltage and current components with virtual signals are transformed into $\alpha - \beta$ coordinate by Clark-Concordia transformation mention above. Since the real and virtual signals forms three balanced signals, the zero component of the transformation equals to zero. Therefore, Clark transformations of voltage and current signals are given in Eqs. 3.17 and 3.18.

$$v_{x,\alpha\beta} = T_{abc\to\alpha\beta} v_{x,abc} \tag{3.17}$$

$$i_{x,\alpha\beta} = T_{abc\to\alpha\beta} i_{x,abc} \tag{3.18}$$

In this framework, instantaneous active and reactive power invariants of individual phase can be expressed as Eqs. 3.19 and 3.20. As mention above, no zero components occurs because of balanced real and virtual signals. Thus, the active power of zero invariant equals to zero ($p_{X,0} = 0$).

$$p_{x,\alpha\beta} = v_{x,\alpha\beta}.i_{x,\alpha\beta} = \begin{bmatrix} v_{x,\alpha} & v_{x,\beta} \end{bmatrix} \begin{bmatrix} i_{x,\alpha} \\ i_{x,\beta} \end{bmatrix} = v_{x,\alpha}.i_{x,\alpha} + v_{x,\beta}.i_{x,\beta} \tag{3.19}$$

$$p_{x,\alpha\beta} = v_{x,\alpha\beta} x i_{x,\alpha\beta} = \begin{bmatrix} v_{x,\alpha} & v_{x,\beta} \\ i_{x,\alpha} & i_{x,\beta} \end{bmatrix} = v_{x,\alpha}.i_{x,\beta} - v_{x,\beta}.i_{x,\alpha} \tag{3.20}$$

Similar to conventional pq theory, instantaneous active and reactive power invariants include dc and ac parts. The dc parts define the powers because of fundamental signals. In contrasts, the ac parts come from harmonic signals. Thus, the ac signals can be decoupled from the total signal by low pass filter. After decoupling the ac signals of instantaneous powers, the harmonic currents in αβ stationary frame obtained as in Eq. 3.21.

$$i_{xh} = \begin{bmatrix} i_{xh,\alpha} = \frac{1}{v_{x,\alpha\beta}^2}\left(v_{x,\alpha}\tilde{p}_{x,\alpha\beta} - v_{x,\beta}\tilde{q}_{x,\alpha\beta}\right) \\ i_{xh,\beta} = \frac{1}{v_{x,\alpha\beta}^2}\left(v_{x,\alpha}\tilde{q}_{x,\alpha\beta} + v_{x,\beta}\tilde{p}_{x,\alpha\beta}\right) \\ i_{xh,0} = 0 \end{bmatrix} \tag{3.21}$$

Where, $v_{x,\alpha\beta}^2 = v_{x,\alpha}^2 + v_{x,\beta}^2$

The harmonic reference currents in abc frame are then obtained by applying inverse Clarke transformation as follows.

$$\begin{bmatrix} i_{xh,a} \\ i_{xh,b} \\ i_{xh,c} \end{bmatrix} = T_{\alpha\beta\rightarrow abc} \begin{bmatrix} i_{xh,\alpha} \\ i_{xh,\beta} \end{bmatrix} \tag{3.22}$$

3.2.2. DC link Regulator

DC link controller is used in order to regulate the dc link voltage at a constant value and to compensate the losses stemmed from switching of VSI. There are various dc link regulators applied in literature such as proportional integrator (PI), adaptive controller, artificial neural network (ANN) based controller and fuzzy logic controller (Uçak, 2009). In this thesis study, PI controller is applied to control the dc link as shown in Figure 3.10. Thus, the dc link current reference is obtained as Eq. (3.23).

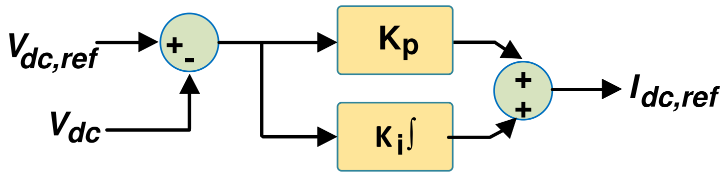

Figure 3.10. Block diagram of dc link regulator

$$I_{dc,ref} = (k_{p,dc} + \frac{k_{i,dc}}{s})(V_{dc,ref} - V_{dc}) \tag{3.23}$$

The reference value of the dc link voltage is offered to be neither too low nor too high. The current tracking is weak when the reference value is too low and the semiconductor components are jeopardized when the reference value is too high (Longhui et al., 2007), thereby the reference value is recommended to be at least 1.6 times of the peak value of the system voltage (Geddada et al., 2012).

3.2.3. Current Controller

The current controller has vital importance in the operation of SAPF and directly effects performance of SAPF. In addition, the controller of SAPF must have effective tracking of the sudden changes in reference signals to sufficiently compensate the harmonics in the grid. According to compensation strategy, the direct current control and the indirect current control methods can be used in controller of SAPF (Tan et al., 2017). Direct control uses load current and APF current for reference generation while indirect control uses source current. Since direct current control method shows faster response when compared with indirect control method, direct current control method will be used for current control. Various current controllers, such as proportional (P) controller, proportional – integral (PI) controller, proportional resonant (PR) controller, fuzzy controller, artificial neutral network based controller, are examined in literature (Terciyanlı, 2010). In this thesis, the current control is performed in dq frame. Proportional Resonant (PR) current controller is used in SAPF system, where P controller is used for fundamental signal control and R controller is preferred to track the harmonic current references. The resonant controller is tuned to control the signal at a specific frequency, which has effective reference current tracking of the tuned signal frequency. The block diagram of the SAPF current controller is demonstrated in Figure 3.11. The transfer function of the controller is given in Eq. 3.24.

In the experimental studies, three phase uncontrolled rectifiers are used as nonlinear load. The uncontrolled rectifiers generate currents harmonics with $6n \pm 1$ orders of the fundamental frequency, which are 5th, 7th, 11th, 13th, etc. in stationary frame. The $(6n \pm 1)^{th}$ order harmonics transformed into $6n^{th}$ order harmonics in dq rotating frame. Hence, the resonant controller is tuned at first fifth harmonic orders in dq frame. These harmonic orders are 6, 12, 18 and 24 in dq frame, respectively.

$$G_{cc}(s) = K_{p,cc} + \sum_{n=1}^{5} K_{r,cc} \frac{s}{s^2+(6n)^2 w_1^2} \tag{3.24}$$

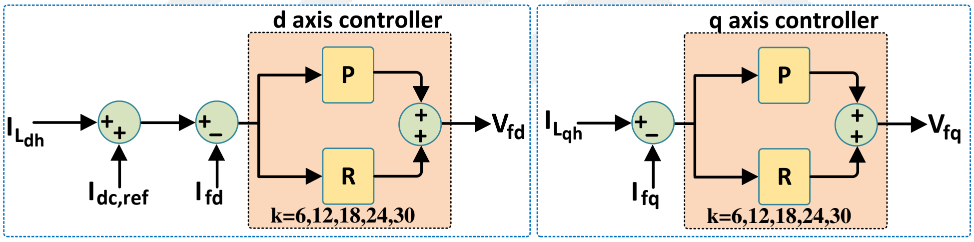

Figure 3.11. Current controller of SAPF with LCL filter

3.3. SAPF with undamped LCL filter system

In this section, SAPF with undamped LCL filter system is analyzed and evaluated. As discussed above, LCL filter has a resonance peak once undamped. The schematic and block diagrams are given in detail in Introduction Section. The transfer functions of open loop and closed loop are obtained for SAPF with undamped LCL filter as in Eqs. 3.25 and 3.26. G_{cc}, G_i and $G_{Vi \to Igf}$ are transfer functions of controller, inverter and LCL filter, respectively. The details of the transfer functions are given in the previous sections. Bode diagrams of the open loop and closed loop transfer functions are demonstrated in Figures 3.12 and 3.13 according to the transfer functions that details determined below.

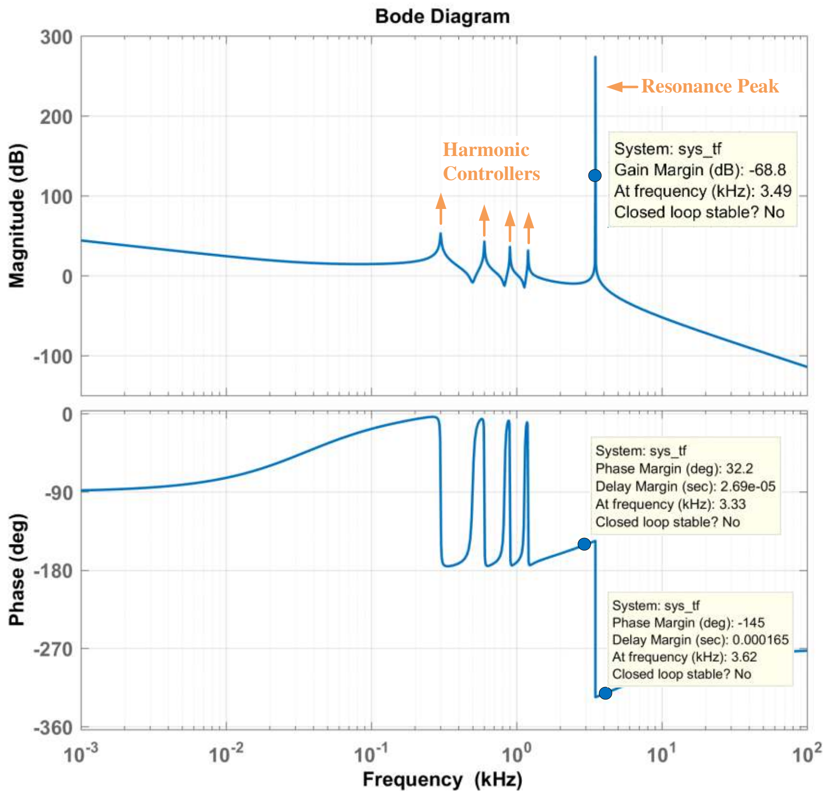

Figure 3.12. Bode plot of open loop transfer function of SAPF with undamped LCL filter

$$G_{ud,open}(s) = G_{cc}(s)G_i(s)G_{Vi\rightarrow Igf}(s) \tag{3.25}$$

$$G_{ud,closed} = \frac{G_{ud,open}}{1+G_{ud,open}} \tag{3.26}$$

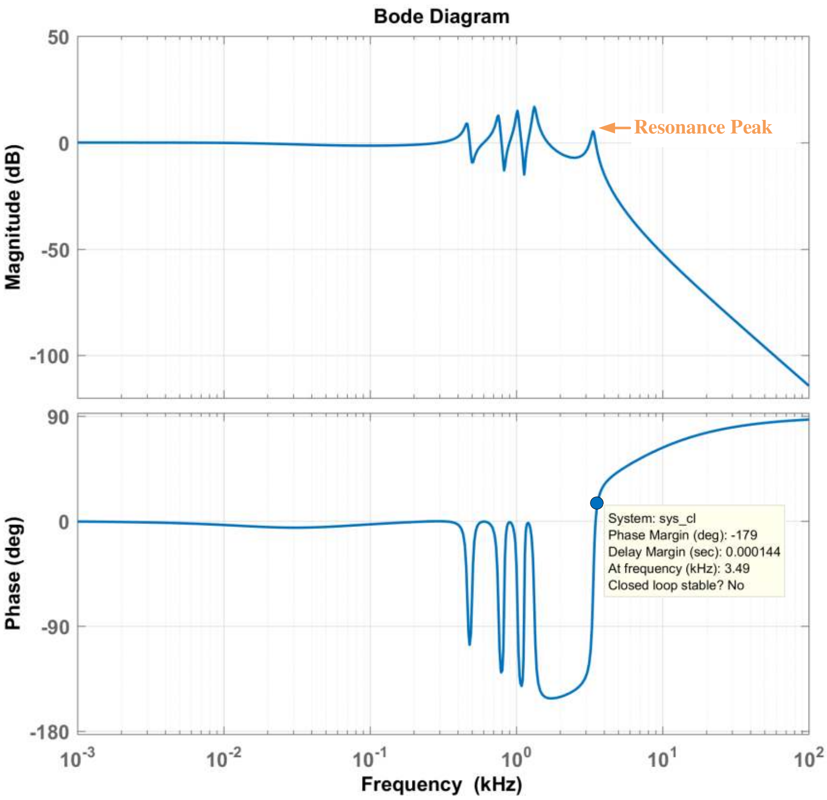

Figure 3.13. Bode plot of closed loop transfer function of SAPF with undamped LCL filter

It is seen from Bode plots of open loop and closed loop transfer functions that SAPF with undamped LCL filter has a resonance peak at 3.49 kHz which causes the unstable system. Besides, there are another peaks in bode plots because of harmonic controllers. These peaks ensure better tracking of harmonic compensation currents. The frequencies of these peaks are set at 300Hz, 600Hz, 900Hz and 1200Hz in dq control frame to control 6th, 12th, 18th and 24th orders in dq frame.

3.4. Investigated Damping Methods for LCL Filter Resonance

In this section, the conventional series resistor passive damping, capacitor current feedback and the proposed CBAD for SAPF with LCL filter have been investigated and analyzed in terms of controller performance and damping power losses.

3.4.1. Simple Series Resistor Passive Damping

The first conventional method used in literature to damp LCL filter resonance is the series resistor PD method. It is realized by adding simple resistor series with the filter capacitor. The circuit and block diagrams of LCL filter with simple resistor PD method are shown in Figure 3.14. The series equivalent resistances, because of too low values, are neglected for analysis of system. Thus, the transfer function of LCL filter with simple resistor PD is obtained from the block diagram as given in Eq. 3.27.

$$G_{Vi\rightarrow Ig}(s) = \frac{R_d C_f s+1}{L_1 L_2 C_f s^3+(L_1+L_2)R_d C_f s^2+(L_1+L_2)s} \tag{3.27}$$

The damping resistor R_d value, at least, is proposed to be as one over three of the capacitor impedance at the resonant frequency to sufficiently attenuate the LCL filter resonance (Liserre et al., 2005). Thus, the damping resistor value can be calculated by Eq. 3.28. Then, the damping factor is acquired in Eq. 3.29.

$$R_d = \frac{1}{3 w_{res} C_f} \tag{3.28}$$

$$\zeta = \frac{R_d C_f w_{res}}{2} \tag{3.29}$$

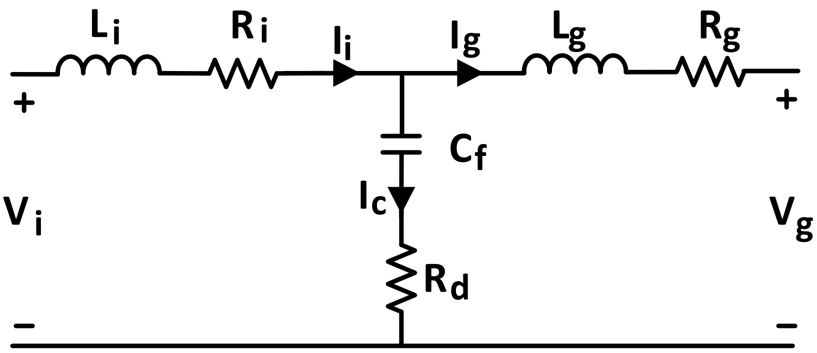

(a)

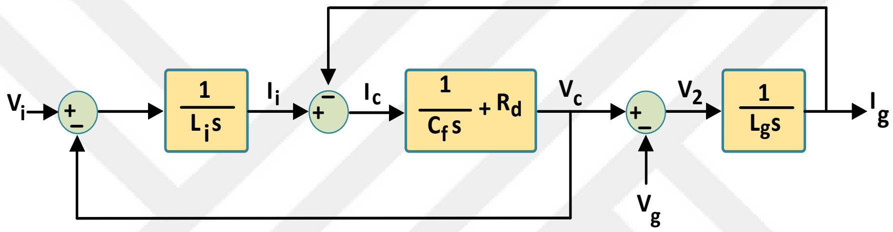

(b)

Figure 3.14. LCL filter with simple resistor PD method (a) Circuit scheme and (b) Block diagram

The transfer functions of open loop and closed loop are given for SAPF with simple resistor passive damped LCL filter in Eqs. 3.30 and 3.31. The bode plots of open loop and closed loop of SAPF with passively damped LCL filter are demonstrated in Figure 3.15 and 3.16, respectively.

$$G_{pd,open}(s) = G_{cc}(s)G_i(s)G_{Vi\rightarrow Igf}(s) \tag{3.30}$$

$$G_{pd,closed} = \frac{G_{pd,open}}{1+G_{pd,open}} \tag{3.31}$$

It is seen from Bode plots of open loop and closed loop transfer functions that SAPF with passively damped LCL filter has a suppressed resonance peak at 3.49 kHz which results in a stable system. From Eq. 3.28, the damping resistor is calculated approximately 1.2 Ω. A 1.5 Ω series resistor is selected from the market and used for sufficient resonance damping.

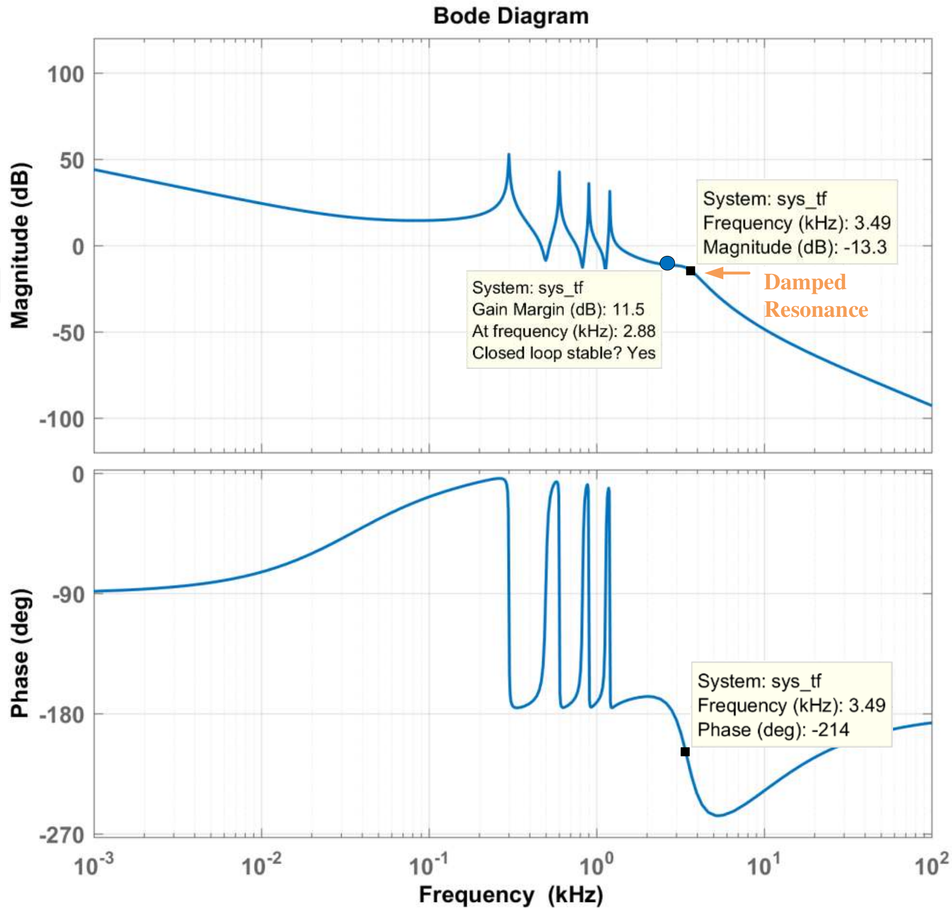

Figure 3.15. Bode plot of open loop transfer function of SAPF with passive damped LCL filter system

The series resistor with the filter capacitor causes additional power losses in the system, which decreases the overall efficiency of SAPF system. The power losses due to series resistor are given in the following section in detail.

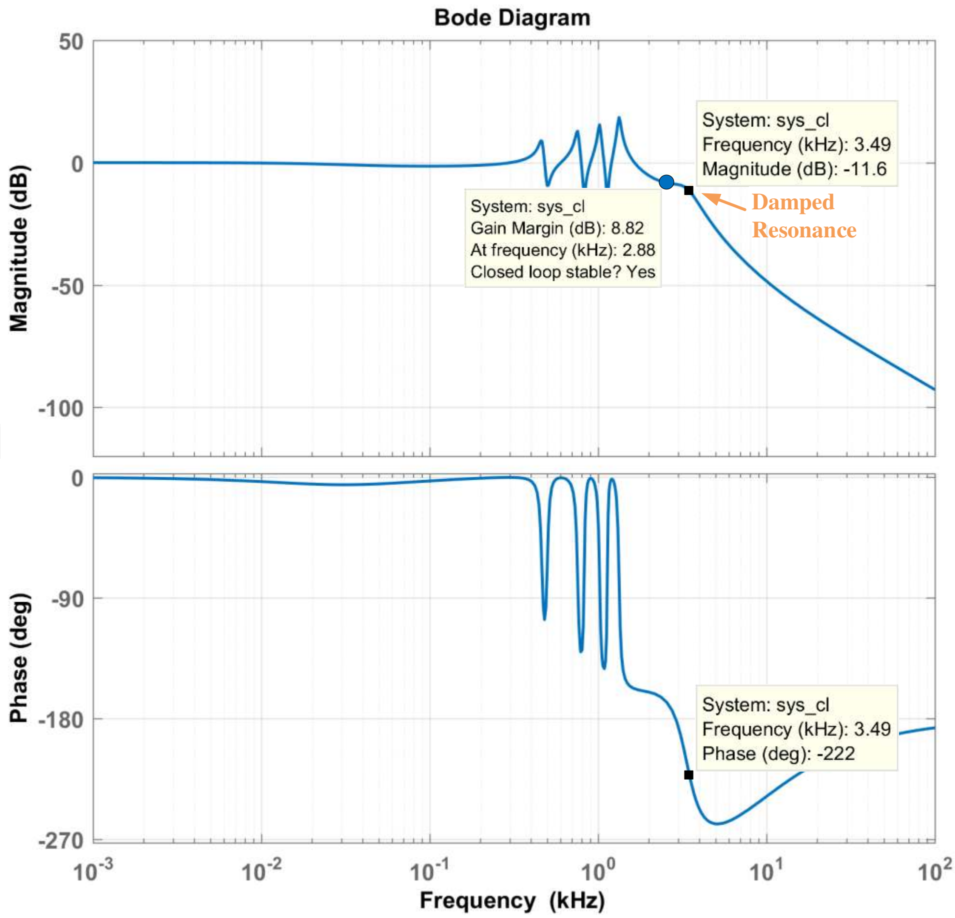

Figure 3.16. Bode plot of closed loop transfer function of SAPF with passive damped LCL filter system

3.4.1.1. Power Losses Calculation of Simple Passive Damping

The total power losses released due to the damping resistor, given in Eq. 3.32, include fundamental, harmonic and switching frequency components, P_{dF} and P_{dSw} (Balasubramanian and John, 2013; Pena-Alzola et al., 2013).

$$P_{loss,PD} = P_{dF} + P_{dSw} \tag{3.32}$$

The power loss of fundamental component, P_{dF}, in the damping resistor is calculated by the fundamental current component passing through the filter capacitor, I_{cF} (Balasubramanian and John, 2013). Because of the capacitor impedance is excessively higher than the damping resistor at fundamental frequency, $R_d \ll Z_{cF}$, the damping resistor is omitted to simplify the equation. Z_{cF} is the filter capacitor impedance at fundamental frequency (Pena-Alzola et al., 2013). Therefore, the power loss owing to fundamental component is estimated as Eq. 3.33.

$$P_{dF} \approx 3I_{cF}^2 R_d \tag{3.33}$$

Where the fundamental capacitor current equals to $I_{cF} \approx V_{cF}/Z_{cF}$ by neglecting the damping resistor. Considering small voltage drop across the grid-side filter inductor, the capacitor voltage can be accounted equal to the grid voltage V_g. Then, Eq. 3.33 is revised as Eq. 3.34.

$$P_{dF} \approx 3V_s^2 (w_1 C)^2 R_d \tag{3.34}$$

The switching frequency components losses, P_{dSw}, in the damping resistor are calculated by the switching frequency current components passing through the filter capacitor, I_{cSw} (Pena-Alzola et al., 2013). The switching components are generated at switching frequency and its multiples. The phase-neutral instantaneous output voltage of inverter with SPWM is expressed as Eq. 3.35. The first and second terms determine the fundamental and the switching frequency sideband voltages, respectively (Chung and Sul, 1997).

$$v_{xn}(t) = V_{dc} M_a cos(w_1 t + \phi_1) + v_{sw}(t) \tag{3.35}$$

Where,

$$v_{Sw}(t) = \frac{4V_{dc}}{\pi} \sum_{m=1}^{\infty} \sum_{n=-\infty}^{\infty} \frac{1}{m} J_n\left(m\frac{\pi}{2}M_a\right) \sin\left([\mathrm{m}+\mathrm{n}]\frac{\pi}{2}\right) \cos(m[w_{sw}t + \emptyset_c]$$
$$+ n[w_1 t + \phi_1]) ; \quad x = a, b, c\ phases$$

m and n are define carrier and baseband index variables. The switching harmonic components are generated at $(mw_{sw} \pm nw_1)$ frequencies. In this regards, the second term is taken into account in order to examine the switching frequency losses on the damping resistor. The switching harmonic components flows the filter capacitor since the capacitor has negligible impedance for the frequencies higher than the resonance frequency. Thus, inverter-side inductance and the damping resistor are used as an equivalent circuit to estimate the switching harmonic currents. The switching harmonic currents flowing on the damping resistor are calculated as follows.

$$I_{cSw} = \frac{V_{Sw}}{R_d + w_{sw}L_1} \tag{3.36}$$

V_{Sw} is the rms voltage value of the switching frequency components. Thus, the switching damping losses are acquired as follows.

$$P_{dSw} = 3I_{cSw}^2 R_d \tag{3.37}$$

3.4.2. Capacitor Current Feedback Active Damping

The capacitor current feedback AD method is one of the most commonly investigated active damping method in literature. This method is performed through measuring and feedback the capacitor current in control algorithm. The most important feature of this method is that the damping power losses are eliminated. The control structure and block diagram of the capacitor current feedback AD are illustrated in Figure 3.17.

The measured capacitor current is multiplied by a function G_{ad} that is usually a constant. The selection of feedback constant is significant for system stability. Although the higher feedback constant maintains more effective resonance damping, the excessive increase of the feedback constant may compromise the system stability.

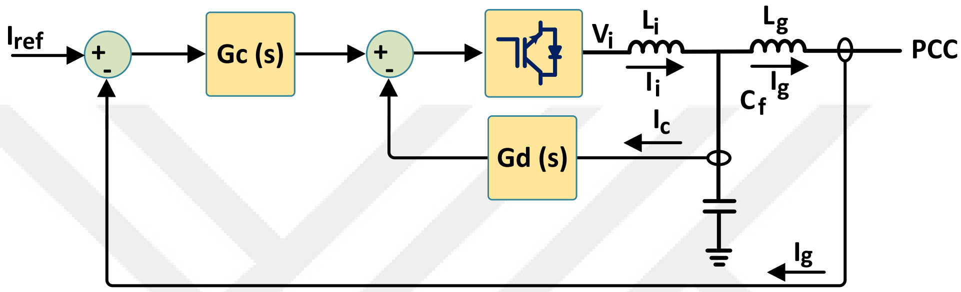

(a)

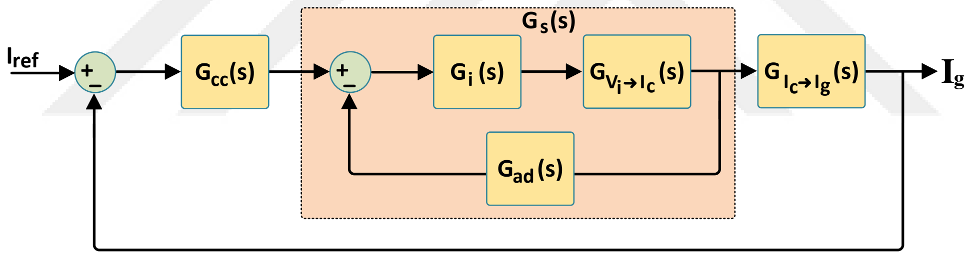

(b)

Figure 3.17. The control structure and block scheme of capacitor current AD

The transfer functions of $G_{Vi\rightarrow Ic}(s)$, $G_{Ic\rightarrow Igf}(s)$ and inner control loop $G_s(s)$, are given in the following Eqs. 3.38, 3.39 and 3.40. The transfer functions of open loop and closed loop of SAPF with capacitor current feedback damped LCL filter are given in Eqs 3.41 and 3.42. Accordingly, Bode plots obtained from open loop and closed loop transfer functions are shown in Figures 3.18-3.21 for different feedback constant values.

$$G_{Vi\to Ic}(s) = \frac{1}{L_1} \cdot \frac{s}{s^2 + w_{res}^2} \tag{3.38}$$

$$G_{Ic\to Ig}(s) = \frac{1}{L_2 C_f s^2} \tag{3.39}$$

$$G_s(s) = \frac{G_i(s).G_{Vi\to Ic}(s)}{1 + G_i(s).G_{Vi\to Ic}(s)} \tag{3.40}$$

$$G_{ad,open}(s) = G_{cc}(s) G_s(s) G_{Ic\to Igf}(s) \tag{3.41}$$

$$G_{ad,closed} = \frac{G_{ad,open}}{1 + G_{ad,open}} \tag{3.42}$$

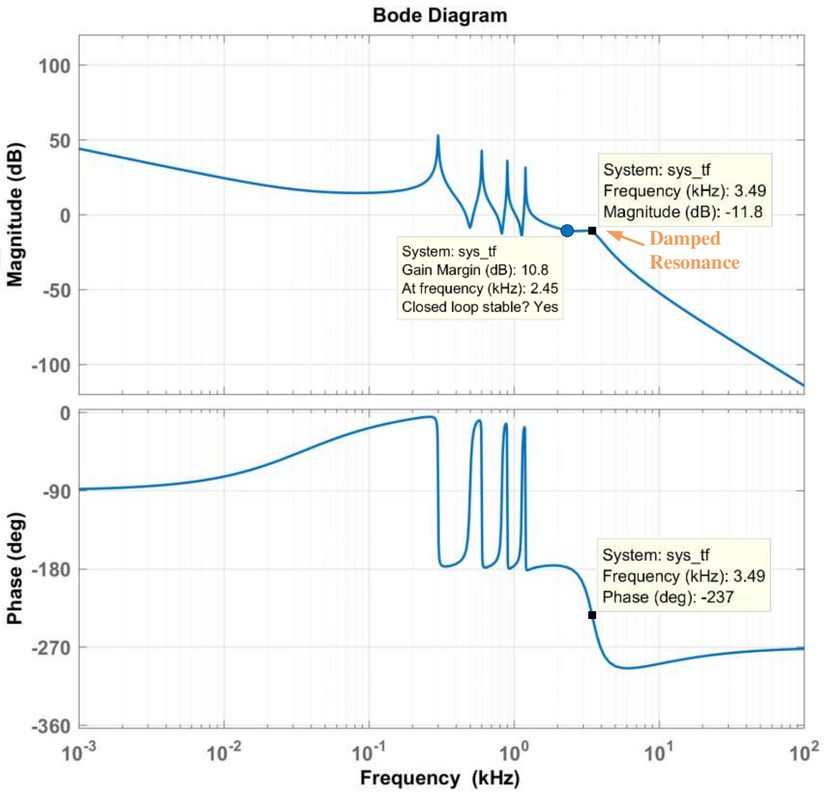

Figure 3.18. Bode diagram of open loop transfer function of SAPF with capacitor current feedback damped LCL filter system ($G_{ad} = 7$)

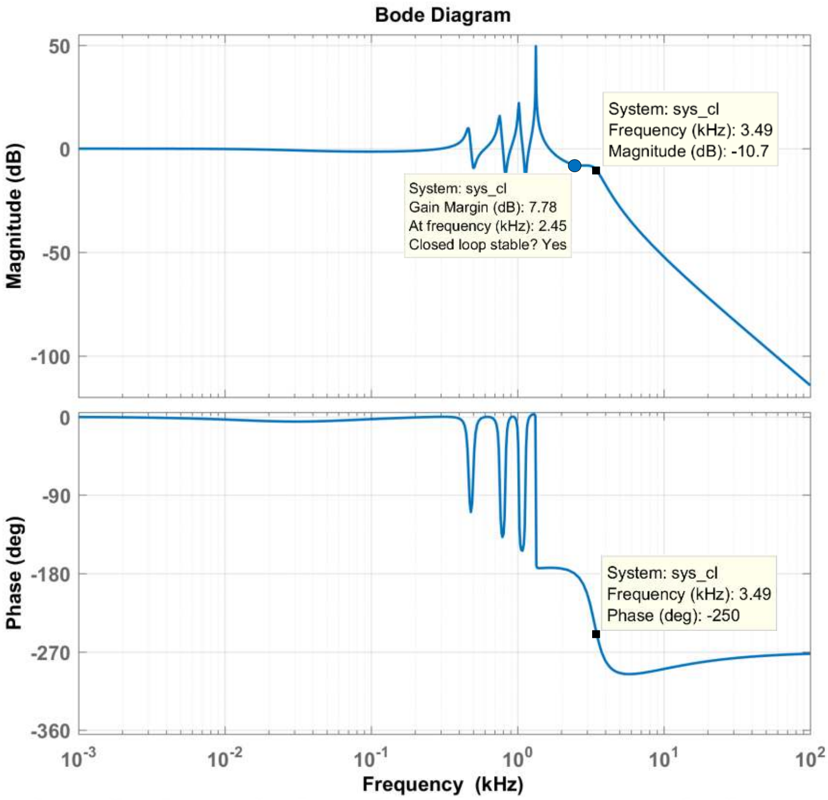

Figure 3.19. Bode diagram of closed loop transfer function of SAPF with capacitor current feedback damped LCL filter system ($G_{ad} = 7$)

It is seen from Bode plots of open loop and closed loop transfer functions that SAPF with capacitor feedback damped LCL filter has a suppressed resonance peak at 3.49 kHz for different feedback constant values. From Bode plot analysis, optimal feedback constant is obtained as, $G_{ad} = 7$. Bode diagrams are plotted by using optimal feedback constant for open loop and closed loop transfer functions. As seen, the resonance of LCL filter is damped and the SAPF system stability is maintained with this value. However, further increase the feedback constant to $G_{ad} = 8.3$, in order to obtain same damping performance with PD method, causes SAPF instability. Moreover, damping the resonance by capacitor current feedback AD method leads to amplification in resonant controller at 24th order frequency.

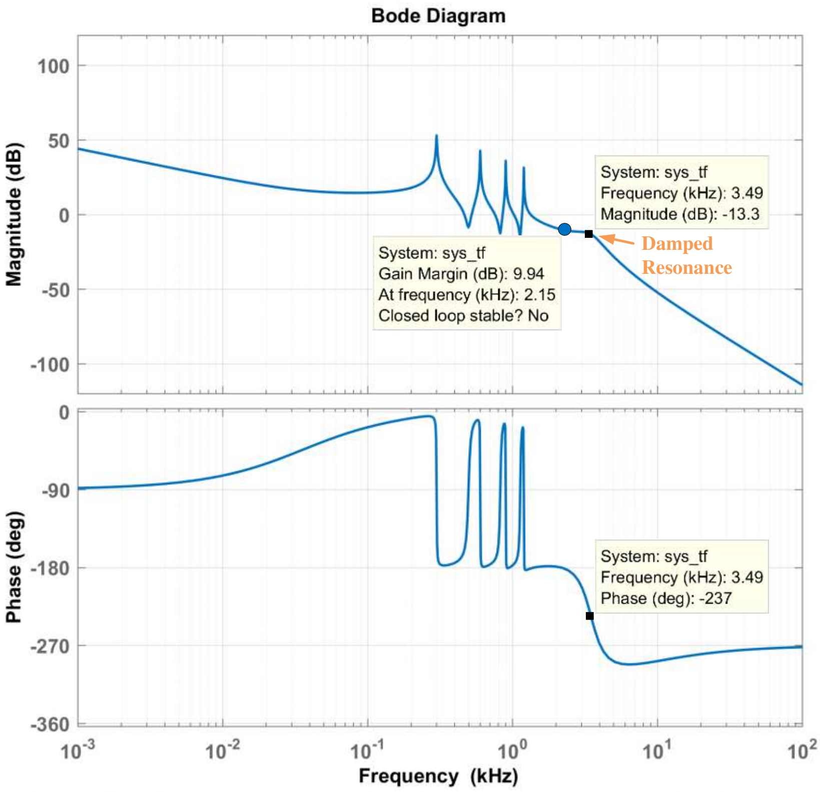

Figure 3.20. Bode diagram of open loop transfer function of SAPF with capacitor current feedback damped LCL filter system ($G_{ad} = 8.3$)

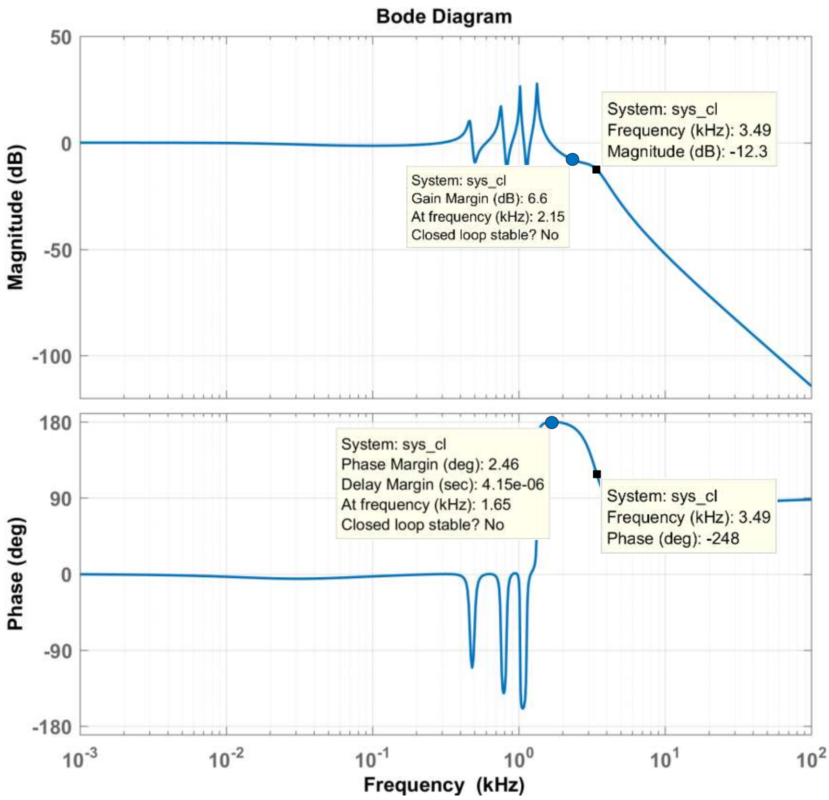

Figure 3.21. Bode diagram of closed loop transfer function of SAPF with capacitor current feedback damped LCL filter system ($G_{ad} = 8.3$)

3.4.3. The Proposed Resonance Damping Method: Converter Based Active Damper

In this section, a novel converter based active damper (CBAD) is proposed for SAPF with LCL filter. The proposed method uses an auxiliary three phase three leg converter with an inductance connected to filter capacitor. The circuit diagram of SAPF with CBAD damped LCL filter is shown in Figure 3.22. The CBAD method, for the first time, is investigated for SAPF with LCL filter.

The auxiliary converter operates similar to the operation principle of SAPF. It includes VSI, dc link capacitor and auxiliary inductance. Different from SAPF, the rating of auxiliary converter is quite low. Since the filter capacitor hold fundamental frequency component, the dc link voltage level of the auxiliary converter can be decreased considerably. Thus, the ratings of the dc link and IGBTs can be reduced.

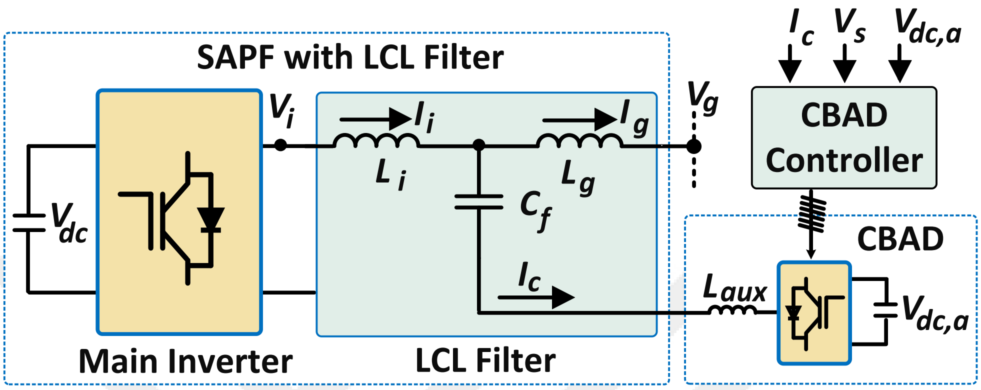

Figure 3.22. The circuit scheme of SAPF with LCL filter damped by CBAD

The control algorithm of auxiliary converter is depicted in Figure 3.23. The dc link energy of auxiliary converter is provided from the grid. Thus, an external energy source is not required similar to SAPF system. Besides, the capacitor current is measured in the auxiliary converter in order to generated reference resonance current. The resonance current is obtained by using a notch filter (Buyuk et al., 2018). Notch filter is a band stop filter rejecting the signal at the tuned frequency. Then, the resonance signal is obtained by extracting the filtered signal from capacitor current. The transfer function of the notch filter is given in Eq. 3.43.

$$G_n(s) = \frac{s^2 + w_n^2}{s^2 + Qs + w_n^2} \tag{3.43}$$

Where, Q index determines the rejection bandwidth and gain of the notch filter (Buyuk et al., 2018).

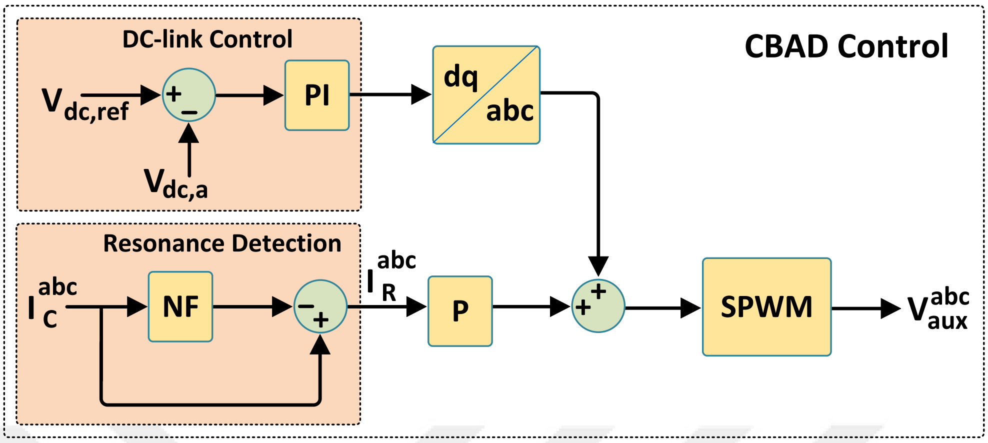

Figure 3.23. The control algorithm of CBAD

The auxiliary converter shows resistance characteristic around the resonant frequency. The simplified circuit scheme of LCL filter with CBAD is illustrated in Figure 3.24. Besides, the resistance characteristic of CBAD is shown in Figure 3.25. $G_d(s)$ is the transfer function of CBAD and it is a constant at the resonance frequency. The resistance of CBAD is tuned to demonstrate 1.5Ω at the resonance frequency. The transfer function of LCL filter with CBAD is then obtained by considering auxiliary inductor as in Eq. 3.44.

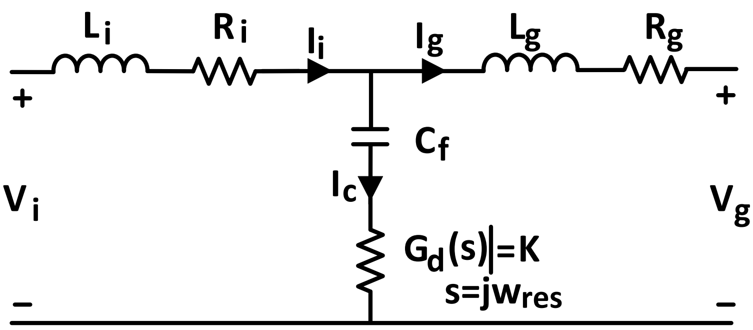

Figure 3.24. Simplified circuit diagram of LCL filter with CBAD

$$G_{Vi\to Ig}(s) = \frac{s^2 C_f L_{aux} + sC_f K + 1}{As^3 + Bs^2 + Cs} \tag{3.44}$$

Where, $A = C_f(L_{aux}L_1 + L_{aux}L_2 + L_1L_2)$, $B = KC_f(L_1 + L_2)$ and $C = L_1 + L_2$.

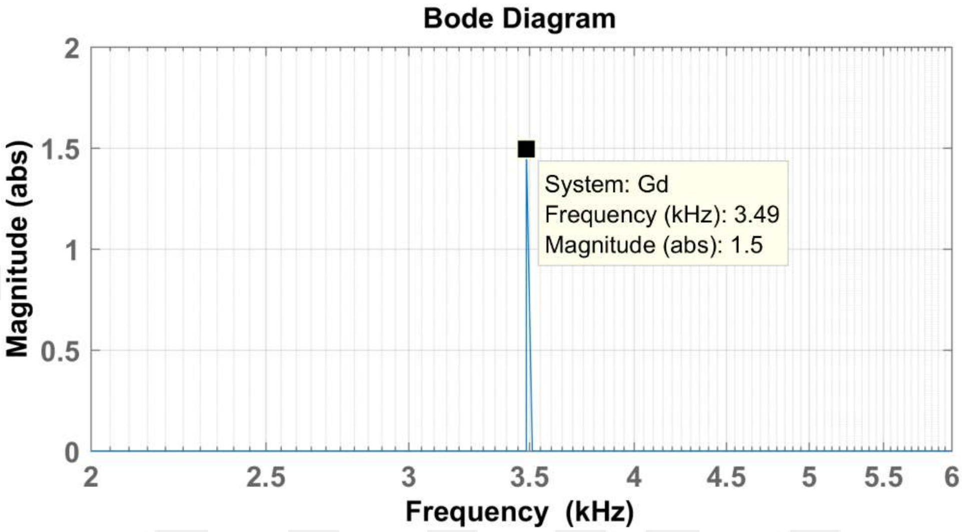

Figure 3.25. Resistance characteristic of CBAD

The transfer functions of open loop and closed loop of SAPF with CBAD damped LCL filter are same as the transfer functions of undamped system. However, $G_{Vi \to Igf}$ is the transfer function of LCL filter damped with CBAD given in Eq. 3.45. Thus, Bode plots obtained from open loop and closed loop transfer functions are demonstrated in Figures 3.26 and 3.27. It can be the frequency response of CBAD has similar characteristic with PD method up to resonance frequency. On the other side, it has the characteristics of undamped LCL filter at the frequencies between the resonance frequency and twice switching frequency. Besides, it shows a notch at the twice switching frequency, which has better attenuation of ripple harmonics at that frequency.

$$G_{cbad,open}(s) = G_{cc}(s)G_i(s)G_{Vi \to Igf}(s) \quad (3.45)$$

$$G_{cbad,closed} = \frac{G_{cbad,open}}{1+G_{cbad,open}} \tag{3.46}$$

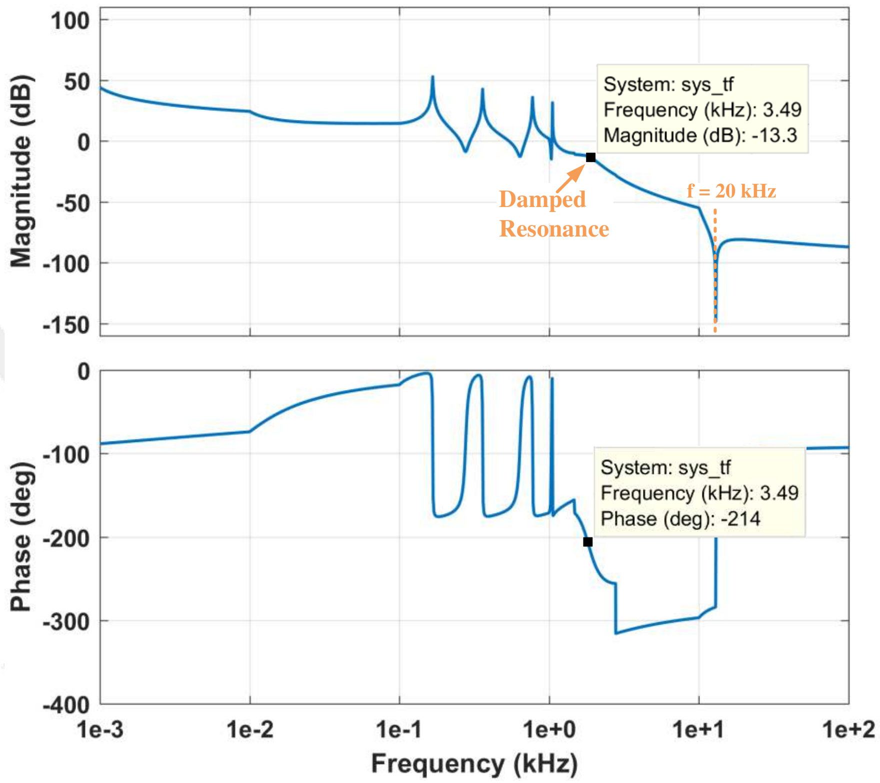

Figure 3.26. Bode diagrams of open loop of SAPF with CBAD damped LCL filter system

The auxiliary converter has power losses released during switching of IGBTs. The power loss calculation of auxiliary converter is given in the following section.

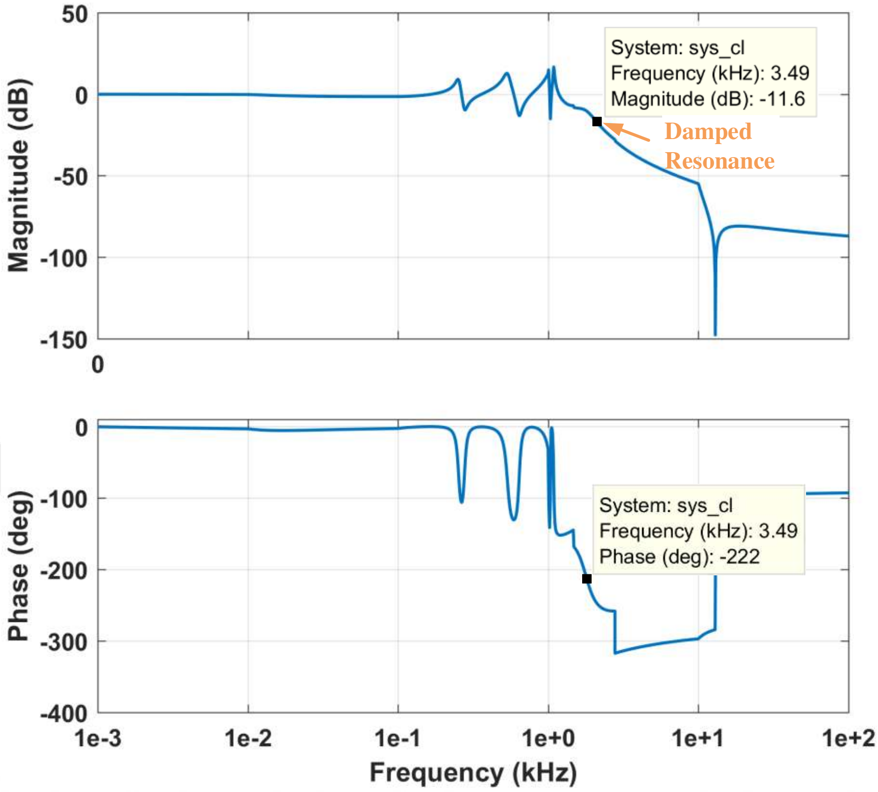

Figure 3.27. Bode diagrams of closed loop of SAPF with CBAD damped LCL filter system

3.4.3.1. Power Losses Calculation of CBAD

CBAD is a three-phase voltage-source inverter formed by a DC link capacitor and six IGBTs. This inverter operates as voltage controlled VSI. An inverter basically includes switching and conduction power losses. These losses are generated during conduction of IGBT and FWD, switch-on/off of IGBT switches and reverse recovery of FWD (Bierhoff and Fuchs, 2004; Aghdam and Gharehpetian, 2005). The total power loss of the inverter is calculated as follows.

$$P_{loss,inv} = \underbrace{P_{cond,IGBT} + P_{cond,FWD}}_{P_{cond}} + \underbrace{P_{on,IGBT} + P_{off,IGBT} + P_{rr,FWD}}_{P_{sw}} \quad (3.47)$$

Where,

$P_{cond,IGBT}$: Individual IGBT conduction loss

$P_{cond,FWD}$: Individual FWD conduction loss

$P_{on,IGBT}$: IGBT switching turn-on loss

$P_{off,IGBT}$: IGBT switching turn-off loss

$P_{rr,FWD}$: FWD reverse recovery loss

The total switching power losses P_{sw}, which include IGBT turn-on and turn-off losses and diode reverse recovery loss, are obtained by Eq. 3.48 from (Bierhoff and Fuchs, 2004).

$$P_{sw} = \frac{6\sqrt{2} f_{sw} V_{dc} I_{inv}}{\pi}.(E_{on,IGBT} + E_{off,IGBT} + E_{off,FWD}) \quad (3.48)$$

On the other side, conduction losses P_{cond}, consist of IGBT and diode conduction losses, are acquired by Eq. 3.49. The total conduction losses are get through multiplying the sum of individual conduction losses of IGBT and FWD by 6 (Bierhoff and Fuchs, 2004). The individual IGBT and FWD conduction losses are calculated as Eqs. 3.45 and 3.46.

$$P_{cond} = 6 * (P_{cond,IGBT} + P_{cond,FWD}) \quad (3.49)$$

$$P_{cond,IGBT} = \frac{V_{CE0} I_{inv}}{2\pi} \int_0^{\pi} \sin(w_1 t) \frac{1+M(t)}{2} dwt + \frac{r_{CE} I_{inv}^2}{2\pi} \int_0^{\pi} sin^2(w_1 t) \frac{1+M(t)}{2} dwt \quad (3.50)$$

$$P_{cond,FWD} = \frac{V_{F0} I_{inv}}{2\pi} \int_0^{\pi} \sin(w_1 t) \frac{1-M(t)}{2} dwt + \frac{r_F I_{inv}^2}{2\pi} \int_0^{\pi} sin^2(w_1 t) \frac{1-M(t)}{2} dwt \quad (3.51)$$

In equations of IGBT and FWD conduction losses, M(t) is the function of modulation type, where SPWM is used for SAPF and CBAD prototypes in experimental studies (Chung and Sul, 1997; Bierhoff and Fuchs, 2004). V_{CE0} and r_{CE} are the threshold voltage and internal collector-emitter resistance of IGBT used in VSI. V_{F0} and r_F are threshold voltage and internal diode resistance of FWD.

According to formulas given above for VSI power losses, CBAD power losses are calculated 78.5W under rated power operation. In addition to the switching and conduction losses of VSI, the IGBT drivers also have near 7-8W power losses. Thus, the total power losses of auxiliary converter operating under the rating given for CBAD are obtained as 85.5W.

4. DESIGN AND IMPLEMENTATION OF THE SYSTEM

4.1. Introduction

In the scope of this thesis study, a laboratory prototype of SAPF with LCL output filter is designed and implemented to compensate the current harmonics generated from nonlinear loads. Moreover, the implemented prototype is also capable for applications of various resonance damping methods, including damping methods based on passive components, control algorithms and auxiliary converter. The experimental studies of implemented prototype system is fulfilled in Power Electronics Research Laboratory of Electrical and Electronics Engineering Department of Çukurova University. The circuit scheme of the designed and implemented system is shown in Figure 4.1.

SAPF with LCL filter, designed as 10kVA, is implemented according to 400V grid system compensating harmonic currents of six pulse rectifiers up to 15A. Besides, auxiliary converter is designed as 1.5 kVA for resonance damping.

The theoretical design studies of SAPF with LCL filter and CBAD are supported by the construction simulation model of all systems in MATLAB/Simulink environment. The design specifications of the prototype power circuits are specified and confirmed by simulation result studies.

The implemented systems mainly include power circuits and electronic control systems. The power circuits are designed according to power ratings. On the other hand, the electronic control systems are almost similar. The measurement scales of currents and dc link may only differ.

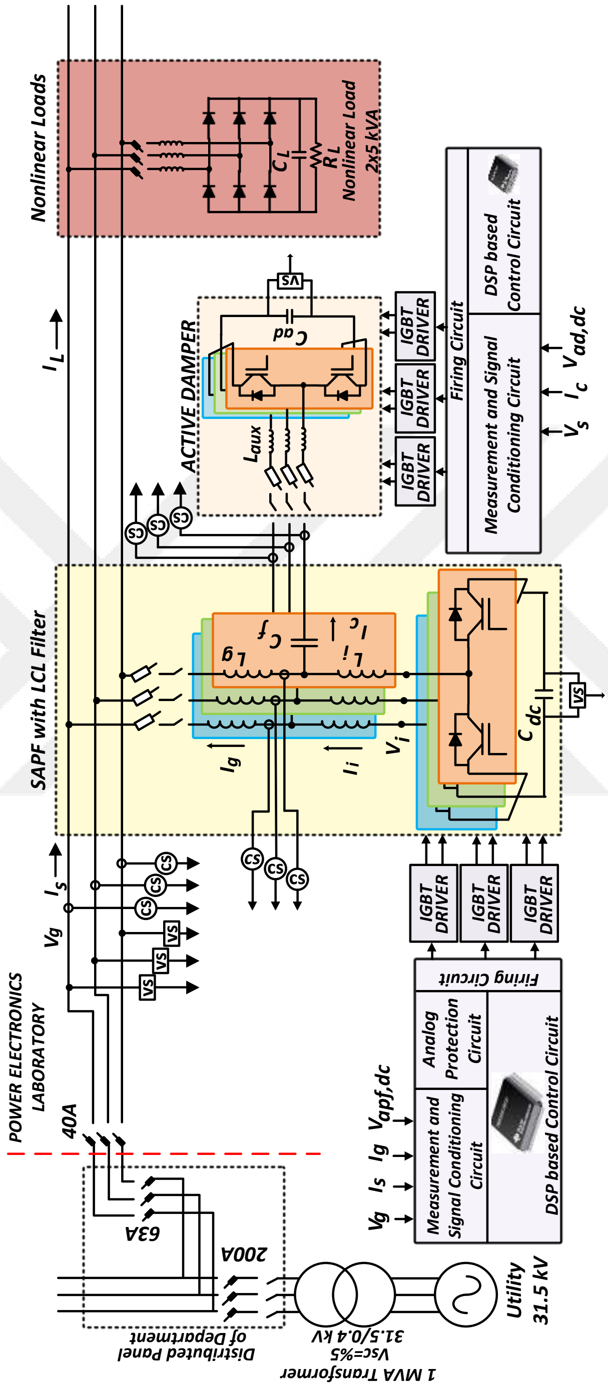

Figure 4.1. The circuit scheme of the implemented system

4.2. Design of SAPF with LCL filter

SAPF with LCL filter prototype is designed as 10 kVA to compensate the harmonic currents of nonlinear loads with 15A rating. The nonlinear loads consists of six pulse capacitive loaded uncontrolled rectifier that is the most widespread used nonlinear load type in the distribution systems. A smoothing inductor with range of 1%-5% of nonlinear load impedance is used to limits the effects of the harmonic currents in the grid (Özkaya, 2007). In the experimental studies, the smoothing reactor is selected as 3% of the rectifier impedance. In accordance, the characteristic of the nonlinear load and ratings of the harmonic currents up to 25th order are presented in Table 4.1. By this means, the design power ratings of SAPF with LCL filter prototype are summarized in Table 4.2.

Table 4.1. Harmonic characteristic and current ratings with 3% smoothing reactor

	Harmonic Current Percentage	Measured Nonlinear Load Currents	Rated Compensation Currents
Fund.	100%	32.3A	-
5th	35%	10.1A	13A
7th	10%	3.62A	6A
11th	6.9%	1.46A	3A
13th	3%	0.75A	2A
17th	2.8%	0.57A	2A
19th	1.8%	0.35A	1A
23rd	1.3%	0.32A	1A
25th	1.2%	0.22A	0.5A

Table 4.2. Power ratings of SAPF with LCL filter prototype

Description	**Rating**
SAPF power	10 kVA
Grid voltage	400 V
Grid frequency	50 Hz
Switching frequency	10 kHz
DC link voltage	700 V

4.2.1. Design of LCL Filter

LCL filter design is one of the most significant part in SAPF system. The design of LCL filter for SAPF has some constraints compared to conventional grid-connected VSI since SAPF has wide control bandwidth to inject harmonic currents. The target of LCL filter design to maintain quite low switching frequency harmonics on grid side current. At the same time, the system stability must be taken into consideration during filter design. Improper design of LCL filter may lead the system instable and not mitigate the switching harmonics sufficiently. A few studies has been conducted in literature for design of LCL filter used with SAPF.

According to the literature, the total inductance are calculated so as to sufficiently decrease the switching harmonics and keep lower dc link voltage as possible. Therefore, the total inductance calculation is given in Eq. 4.1. I_F and δ are the rated current of SAPF and allowable ripple current ratio respectively (Buyuk et al., 2018).

$$\frac{V_{dc}}{8\sqrt{2}\delta I_F f_{sw}} \leq (L_1 + L_2) \leq \frac{(V_{dc}^2 - 8V_s^2/3)^{1/2}}{\sqrt{2}w_1 I_F} \quad (4.1)$$

The determination of the resonance frequency is noticeably important. The range of the resonance frequency is given in Eq. 4.2. The constant k value affects the compensation performance of SAPF and the resonance frequency range. The resonance frequency should be neither higher than half of the switching frequency nor lesser than maximum compensated harmonic component. Because, the lower resonance frequency affects the controller bandwidth and the higher resonance frequency has impacts on current ripple mitigation. By this way, it is offered to be in the range from 1.3 to 3 (Buyuk et al., 2015; Buyuk et al., 2018).

$$k * w_{max,h} \leq w_{res} \leq 0.5 w_{sw} \tag{4.2}$$

The filter capacitor value must be selected so that the power factor does not drop under 5% limits (Liserre et al., 2005). Thus, the selection range of the filter capacitor are given as Eq. 4.3.

$$C_f \leq \frac{0.05 P_N}{3 w_1 V_N^2} \tag{4.3}$$

The main requirements of LCL filter design are mainly through DC link voltage (V_{dc}), injected current ripple ratio (δ), power factor of the system, switching frequency (f_{sw}) of SAPF and additionally the maximum compensated harmonic component frequency as summarized in Table 4.3.

Table 4.3. The requirements for LCL filter design

Parameter	Limitation	Reason
Total inductance (L_1+L_2)	< 0.1 (p.u)	To avoid extreme voltage drop
Reactive power consumed by the capacitor	< 5% of rated power	Power factor limit
Resonance frequency	$1.3 w_{hmax} \leq w_{res} \leq 0.5 w_{sw}$	To prevent the grid from serious resonance problems

The values of LCL filter components are obtained according to specified design limits for LCL filter parameters. Table 4.4 gives the calculated filter parameters.

Table 4.4. Calculated LCL filter parameters

Parameter	Definition	Value
L_i	Inverter-side Inductance	1 mH
L_g	Grid-side Inductance	0.2 mH
C_f	Filter Capacitance	12.5 uF
f_{res}	Resonance frequency	3.9 kHz

4.2.2. Selection of Switching Devices

In above discussion, dc link voltage is stated to be 700 V. Besides, the rms value of the phase current for the worst case is measured as 26.2 A. According to these specifications, possible power semiconductor components are researched and compared with regard to switching losses and cost. SEMiX202GB12E4s from SEMIKRON has been selected among researched devices (Semikron, 2014). The technical specifications of SEMiX202GB12E4s is given in Table A.1 in Appendix-A. This device is IGBT module with half bridge configuration. Thus, three devices are used for three-phase application. Besides, the collector emitter voltage and collector current of this module are 1200V and 200A, respectively. Moreover, this module is screw terminal module that eases mounting and demounting it.

Gate drivers are necessary to achieve switching of IGBTs through microprocessor. SKYPER 32 PRO R from SEMIKRON has been chosen as gate driver (Semikron, 2007). This driver is able for two output channels with some features such as drive interlock top/bottom, short circuit protection, under voltage protection and soft turn-off. Besides, Board 2s SKYPER 32 PRO R is used to insert the driver over SEMiX202GB12E4s modules. The technical specifications of SKYPER 32 PRO P is demonstrated in Table A.2 in Appendix-A. Turn-on and turn-off speed of IGBT switches can be adjusted by changing gate resistors on this board. In addition, setting of soft turn-off, IGBT operation voltage, dead time and dynamic short circuit voltage can be adjusted on this board.

4.2.3. Design of DC Link Capacitor Bank and Busbar

The harmonic compensation performance of SAPF is in fact affected by the voltage stability of DC link capacitor. Several parameters, such as frequency of harmonic current and DC link voltage, have impact on the stability of DC link capacitor (Anwar and Teimor, 2002). In fact, the DC link capacitance are determined in terms of the voltage ripple range. In (Thomas et al., 1998), it is stated that the capacitors are designed to keep the DC link voltage ripple in the range of 1% and 2%.

A detailed design procedure of DC link capacitor for SAPF is given in (Yan and Zhu, 2012). The DC link capacitance, thus, is calculated as Eq. 4.4. δ_{max} is maximum ripple voltage across the DC link, and f_h is considered as the equivalent frequency of the harmonic currents, which is defined as Eq. (4.5). Considering SAPF parameters given in Table 4.2 and δ_{max} = 4V and f_h is calculated as 189. Then, the capacitance is obtained as $C_{DC} \geq 2.8\, mF$.

$$C_{DC} \geq \frac{S_N}{2\pi V_{DC}\delta_{max} f_h} \tag{4.4}$$

$$f_h = \frac{f_1}{\sqrt{\sum_{k=2}^{\infty}\frac{1}{(k-1)^2}}} \tag{4.5}$$

The DC link current ripple of SAPF with LCL filter prototype is examined by simulation result. The waveform of the DC link current at full harmonic compensation and rated voltage conditions is shown in Figure 4.2. It can be seen that peak value of the DC link current ripple is almost 17A.

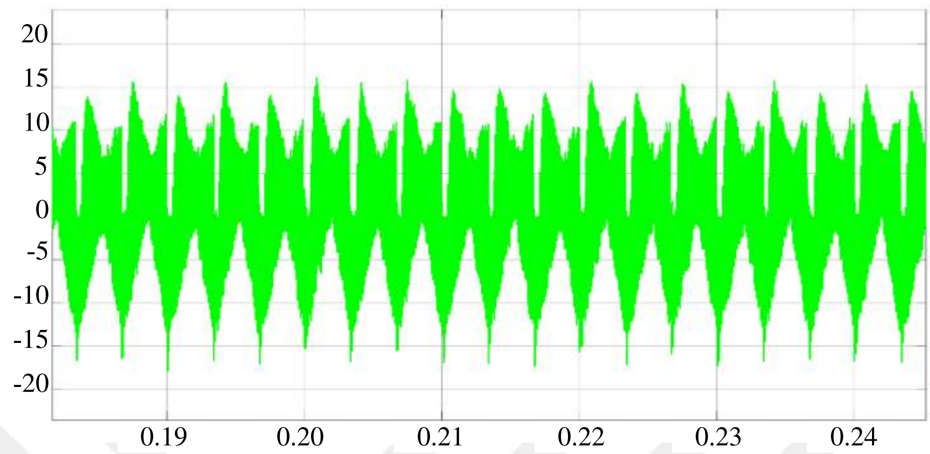

Figure 4.2. The simulation waveform of DC link current

In order to constitute DC link capacitor bank, aluminum electrolytic capacitors are good choice because of their low cost. Several company products are investigated and the optimal capacitor is selected according to the electrical specifications of DC link capacitor for SAPF shown in Table 4.5. According these specifications, 3300µF 450V aluminum electrolytic capacitor, ALS31A332NP450 from KEMET is selected. The technical specifications of the selected dc link capacitor is given in Table 4.6. Four capacitors are used in DC link capacitor bank to form series and parallel branches through two parallel capacitors series with the other two parallel capacitors as demonstrated in Figure 4.3. The electrical specifications of the designed capacitor bank is given in Table 4.7.

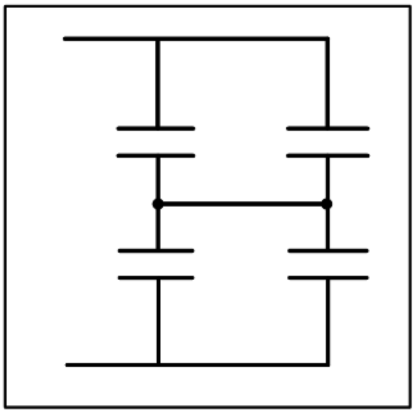

Figure 4.3. The connection diagram of dc link capacitor bank

Table 4.5. Electrical specifications determined for dc link capacitor

Capacitance	≥ 2.8 mF
Rated DC voltage	≥ 800 V
Ripple Current	≥ 30 A
ESL Value	As low as possible
ESR Value	As low as possible

Table 4.6. Technical specifications of the selected dc link capacitor

Manufacturer	KEMET
Product No	ALS31A332NP450
Capacitance	3300 μF
Rated DC Voltage	450 V
Rated Ripple (100 Hz)	16.1 A
Rated Ripple (100 kHz)	25.1 A
ESL (10 kHz)	27 mΩ
ESR Value (100 Hz)	39 mΩ

Table 4.7. Technical specifications of the designed dc link capacitor bank

Equivalent Capacitance	3300 μF
Total Rated DC Voltage	900 V
Total Ripple Current (100 Hz)	32.2 A
Total Ripple Current (100 kHz)	50.2 A
Equivalent ESL	27 mΩ
Equivalent ESR	39 mΩ

A busbar is designed for dc link of SAPF according to design and selection guide given above. In order to prevent IGBTs from high di/dt during switching of IGBTs, which causes high voltage spike across V_{CE} of IGBT, the inductance of current commutation loop should be kept under certain limits. The inductance of current loop is formed from internal inductance of IGBTs, dc link capacitors and dc link busbars. The inductance of IGBTs and dc link capacitors are dependent on manufacturer and produced in low levels through today's technology. The designer dependent parameter for the inductance is dc link busbar design. Low inductance of dc link busbar can be managed by laminated busbar system (Allocco, 1997). The laminated busbar representation is shown in Figure 4.4.

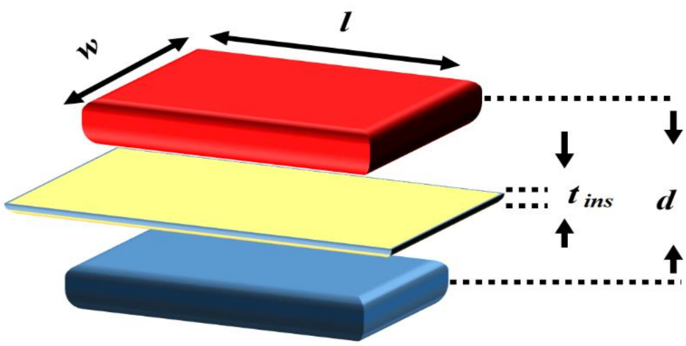

Figure 4.4. The laminated busbar representation

The laminated busbar inductance is the sum of self-inductance and mutual inductance. These inductances can be calculated as Eqs. 4.6 and 4.7, respectively. Besides, the capacitance of the laminated busbar is calculated (Allocco, 1997) as Eq. 4.8.

$$L_s = \frac{\mu_0 \mu_r}{8\pi} l \ (H) \tag{4.6}$$

$$L_m = 2\mu_0 \mu_r \frac{t.l}{\pi(t+w)} \ (H) \tag{4.7}$$

$$C = \varepsilon_0 \varepsilon_r \frac{w.l}{t_{dia}} \ (F) \tag{4.8}$$

Where, μ_0 and μ_r are magnetic permeability of free space and the relative magnetic permeability of material, respectively. ε_0 and ε_r are the permittivity of free space and the relative permittivity of material, respectively.

The DC and AC resistances of laminated busbar and high frequency skin depth (δ) can be calculated as in Eqs. 4.9, 4.10 and 4.11 (Allocco, 1997; Tan, 2015). ρ defines the electrical resistivity of the material.

$$R_{dc} = \rho \frac{2.l}{t.w} \ (\Omega) \tag{4.9}$$

$$R_{ac} = \rho \frac{4.l}{\delta.w} \ (\Omega) \tag{4.10}$$

$$\delta = \sqrt{\frac{\rho}{\pi.f.\mu_0}} \ (\mathrm{m}) \tag{4.11}$$

The laminated busbar of dc link of the proposed SAPF includes three busbar layers, positive (p), negative (n) and midpoint (m) as illustrated in Figure 4.5. The design of power stage layout and laminated busbar of DC link for SAPF have been performed through Autocad program. Figure 4.6 shows the layouts of power stage and laminated busbar of DC link. The laminated busbar has been manufactured by using aluminum plate with 2mm thickness. The aluminum plate has low cost and high resistance to corrosion and oxidation. Trivoltherm series aramid paper from Krempel with 0.36mm thickness has been used between busbars as insulation material.

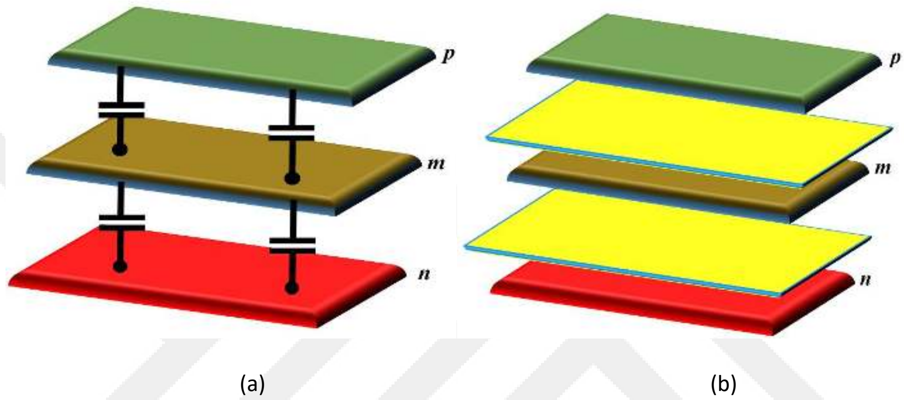

Figure 4.5. (a) The laminated dc busbar with dc capacitors and (b) its layout for SAPF prototype

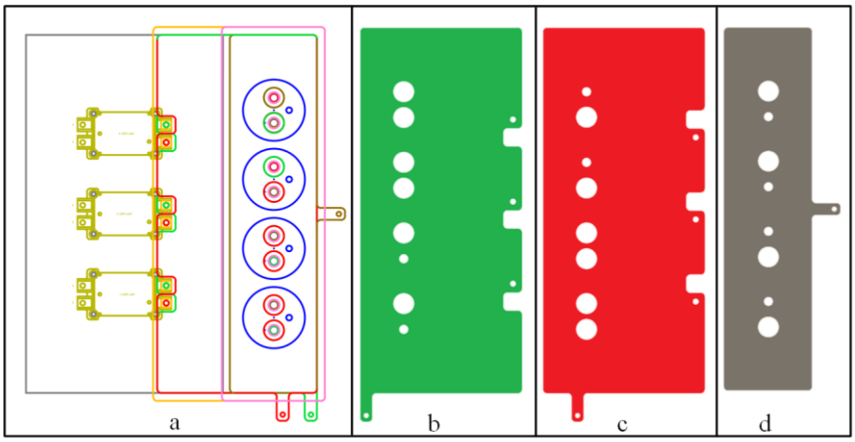

Figure 4.6. Power stage and laminated busbar layouts of dc link busbar for SAPF (a) Power stage layout (b) Positive busbar layout (c) Negative busbar layout and (d) Midpoint busbar layout

The geometrical values and the calculated inductances of the designed laminated busbar are presented in Table 4.8. Thus, the total inductance of DC link current commutation loop is obtained as presented in Table 4.9.

Table 4.8. The specifications of the designed laminated busbar

Busbar width (w)	450 mm
Busbar length (l)	198 mm
Distance between Busbars (d)	2.36 mm
Insulator Thickness (t_{ins})	0.36 mm
μ_r of Aluminum	1.000022
Self-Inductance (L_s)	9.9 nH
Mutual Inductance (L_m)	0.7 nH
Total Inductance of Laminated Busbar	10.6 nH

Table 4.9. The inductance of dc link current commutation loop

Inductance of Laminated busbar	10.6 nH
Total ESL of DC link capacitor bank (2 series capacitor with 2 parallel branch)	20 nH
Internal Inductance of IGBT modules	18 nH
Inductance of Mounting Connection	≈20 nH
Total Inductance of Current Commutation loop (L_t)	68.6 nH

The maximum voltage spike on collector-emitter voltage of IGBT (V_{Cep}) can be calculated by taking account the maximum voltage of dc link, the minimum turn-off time, the maximum turn-off current and dc link commutation inductance as given in (21) (Tan, 2015). The maximum dc link voltage for SAPF is 700 V as discussed above. The maximum turn-off current has been observed as 50 A by simulation study. To get maximum value of V_{CEp} minimum Δt is taken account for turn-off time, and it is determined as 200 ns. Acoordingly, V_{CEp} is obtained as 767.15 V that is well below the value specified for V_{CE} of SEMiX202GB12E4s.

$$V_{CEp} = V_{dc} - L_t \frac{\Delta i_{c,turn-off}}{\Delta t} \tag{4.12}$$

4.2.4. Selection of Heat Sink

The selection of proper heat sink for VSC has been performed by taking account the power loss and thermal calculations. Firstly, the total power consumption of power semiconductors constitutes conduction and switching losses and is obtained as in Eq. 4.13.

$$P_{tot} = P_{cond} + P_{sw} \tag{4.13}$$

In conduction losses of IGBT, there are two type of losses that are IGBT and freewheeling diode losses. In (Tan, 2015), the calculation of the conduction losses are formulated as in Eqs. 4.14 and 4.15.

$$P_{cond,IGBT} = V_{CEO} i_{C,avg} + i_{C,avg}^2 r_{CE} \tag{4.14}$$

$$P_{cond,DIODE} = V_{FO} i_{F,avg} + i_{F,avg}^2 r_F \tag{4.15}$$

The switching losses are calculated in terms of turn-on energy (E_{ON}) and turn-off energy (E_{off}). Turn-on energy is ignored for calculation of freewheeling diodes (Semikron, 2015). The diode losses are calculated with the reverse recovery energy (E_{RR}). Accordingly, the switching losses can be obtained as follows.

$$P_{sw,IGBT} = (E_{ON} + E_{OFF}) f_{sw} \tag{4.16}$$

$$P_{sw,DIODE} = E_{RR} f_{sw} \tag{4.17}$$

In order to determine the thermal resistance of VSI, the thermal model shown in Figure 4.7 is used (Tan, 2015). In (Çetin, 2007), the thermal resistance between heat sink and ambient is calculated as in Eq. 4.18. The parameter values of SEMiX202GB12E4s IGBT module are represented in Table 4.10. Ambient temperature is equal to 40 ºC. P_{module} is the total loss in each SEMiX202GB12E4s IGBT module and calculated as 701.23 W. $P_{loss,VSC}$ is the total power losses of three modules used in VSC that is three times of P_{module}.

$$R_{ha} = \frac{T_J - T_A - R_{th(c-s)} P_{MODULE} - \max(P_{loss,IGBT} R_{th(j-c),IGBT}, P_{loss,DIODE} R_{th(j-c),DIODE})}{P_{loss,VSC}} \tag{4.18}$$

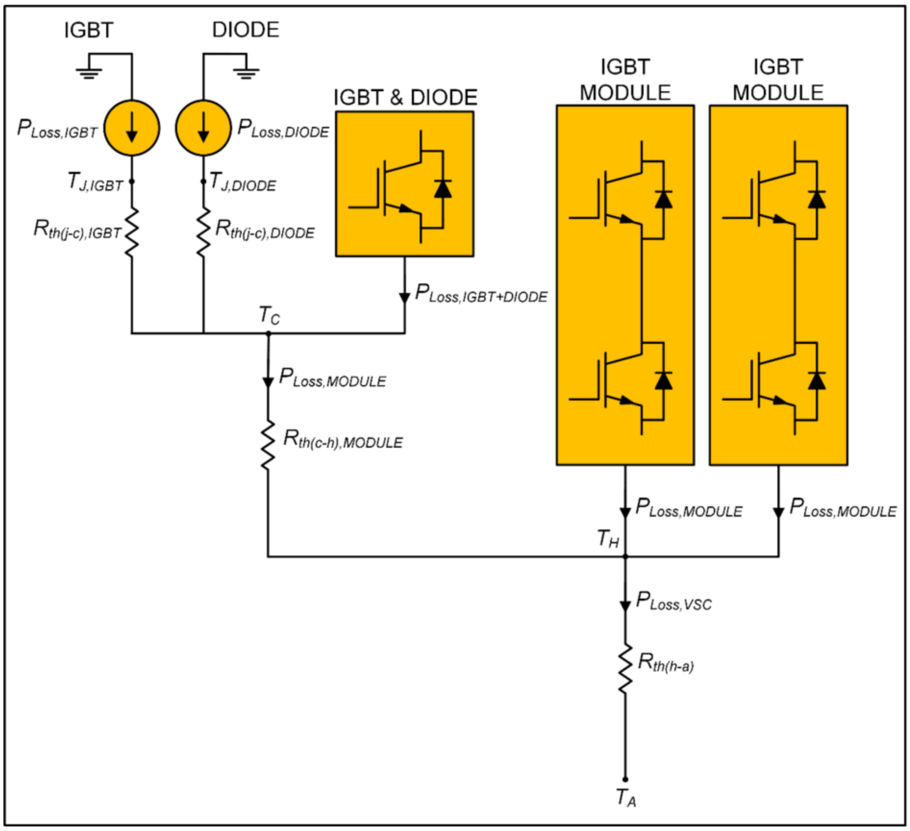

Figure 4.7. Thermal model of three-phase VSI (Tan, 2015)

Table 4.10. Thermal specifications of SEMiX202GB12E4s module

$R_{th(j-c),IGBT}$	0.14 K/W
$R_{th(j-c),DIODE}$	0.26 K/W
$R_{th(c-s)}$	0.045 K/W
T_J	175 °C

The maximum value of the heatsink thermal resistance is calculated as 11.5 K/kW. According this value, the 864 AS heatsink model with natural air cooling is chosen from Arma elektronik.

4.3. Design of CBAD

The design of CBAD includes two main parts; interface filter and VSI. Single inductance interface filter is designed so that it resonates with the capacitor of LCL filter at the switching frequency. The series capacitor-inductance impedance is given in Eq. 4.19. Accordingly, the interface filter value of CBAD is derived as in Eq. 4.20. From Eq. 4.20, L_f is calculated as $5\mu F$ to resonate at switching frequency with the filter capacitor.

$$Z_f = jX_{Lf} - j\frac{1}{X_{Cf}} \tag{4.19}$$

$$L_f = 4\pi f_s^2 C_f \tag{4.20}$$

The power ratings of filter components and VSI are determined by taking account the components at frequencies of fundamental, resonance and switching harmonics. The harmonic current components are neglected because of low effect on rms value of the capacitor current. The fundamental frequency current component is simply attained from Eq. 4.21, which is calculated as 0.91A. The values of the resonance and switching current components are obtained from simulation studies.

The resonance current is measured almost 0.07A once the resonance is damped by CBAD and the rms value of the first fourth switching frequencies are acquired as 2.3A. Thus, the total rms value of the capacitor current is obtained from Eq. 4.22. The current flowing the filter capacitor is calculated as 2.48A. On the other side, the capacitor current peak value during dynamic operation is obtained as 10.5A from simulation results. In order to meet the current ratings and ensure safety system operation, HCTI-10-20.0 series is selected from Signal Transformer for the interface filter of CBAD.

$$I_{cf1} = \frac{V_{g1}}{\sqrt{3}Z_{f1}} \tag{4.21}$$

$$I_{cf} = \sqrt{I_{cf1}^{1} + I_{cf,res}^{2} + I_{cf,sw}^{2}} \tag{4.22}$$

The voltage seen across $L_f - C_f$ is occurred due to fundamental, resonance and switching frequency currents. Therefore, the rms voltage value across Z_f is obtained as Eq. 4.23. Accordingly, the capacitor voltage value is obtained as 233.7V.

$$V_{Zf} = I_{cf1}Z_{f1} + I_{cf,res}Z_{f,res} + I_{cf,sw}Z_{f,sw} \tag{4.23}$$

The auxiliary VSI design has similar aspects with SAPF converter system. In experimental studies, a VSI prototype that previously designed and used in laboratory studies is used as CBAD to suppress the resonance. Only, output interface filter is chosen from market in terms of satisfying the resonance at the switching frequency. To provide the required energy for the VSI losses and the resonance suppression, dc link voltage level of CBAD is kept 100V.

4.4. Design of Electronic Control Systems

The electronic control systems directly have impact on the operation of SAPF with LCL filter and CBAD prototype systems. The performance of microcontroller, the accuracy of the measured voltage and current signals and the resolution of the generated gate signals must satisfy effective operation for the best harmonic compensation of SAPF and resonance damping of CBAD. Moreover, in order to achieve safe operation of the system, analog protection function against the grid voltage and SAPF currents is added to the electronic control system of SAPF. Additionally, the control-command signals for relays and contactors are added to electronic control system via isolated digital input-output circuits.

The DSP based MCU is brain of the electronic control systems. The DSP based MCU has its ADC and PWM units peripherals. All control algorithms have been embedded in it. It gets all the measured signals, I/O signals and fault signals and generates the control signals and PWM signals according to algorithm embedded inside.

In this thesis study, two different electronic control systems are developed for SAPF and CBAD systems. The electronic control system of SAPF with LCL filter is designed to be capable of achieving both PD and AD methods. In addition, it has been designed suitable for both three-phase three-wire and three-phase four-wire systems.

In SAPF prototype, there are fourteen measured signals in electronic control system, which consist of two dc link voltages (positive and negative buses), three grid voltages, three grid-side SAPF currents of LCL filter, three source currents and three capacitor currents of LCL filter. The measured signals have been conditioned for ADC of MCU which of the range is between 0-3V. The signals must be measured with high accuracy to realize the best performance of SAPF. In SAPF prototype system, there will be two protection functionality. One is a digital control where the protection algorithm will be embedded to MCU. The other is an analog protection circuit in the electronic control card. The analog protection is required for safety operation whereas there may be a fault in the program embedded in MCU where the watchdog timer cannot reset the program.

In CBAD, on the other hand, there are eight measured signals in electronic control system, which consist of two dc link voltages, three grid voltages and three capacitor currents of LCL filter. In CBAD prototype system, the protection is only ensured in digital control where embedded to MCU. Additionally, an external watchdog timer is added to protect the system against software crash. The external watchdog timer stop the system once a problem occurs in embedded software.

The digital I/O’s of the MCUs is 3.3V. In order to prevent the electronic control card from EMI influence, the logic signals are transmitted to 5V level. In the electronic control cards, digital I/O circuits are designed to increase the voltage level. Besides, a voltage level transmission is performed for control-command circuit.

4.4.1. DSP based Microcontroller Units

In the electronic control cards, DSP based MCU has been used for overall control algorithms. There are many DSP based MCUs in the microcontroller market. TMS320F28335 and TMS320F28379D DSP based MCUs are chosen from Delfino series of Texas Instrument for SAPF and CBAD prototypes, respectively. Both MCUs has wide application areas such as robotics, industrial automation, power electronics, etc. TMS320F28379D is the recent product from Delfino series of TI. Moreover, it has dual core with 200 MHz clock frequency. Some technical specifications for two MCUs are given in Table 4.11 (Texas-Instruments, 2015; Texas-Instruments, 2018). In many aspects, TMS320F28379D has superiority over TMS320F28335.

Table 4.11. Technical specifications for MCUs

	TMS320F28335	TMS320F28379D
Clock frequency	150 MHz	200 MHz
Floating Point Unit	Available	Available
CPU	32 bit	2x32 bit
RAM	34K x 16	172K x 16
Flash Memory	256K x 16	512K x 16
GPIO Pins	Up to 88	Up to 169
PWM Output	Up to 18	Up to 24
ADC Channels/Resolution	16 Ch/12 bit	12 Ch/16 bit or 24 Ch/12 bit

4.4.2. Measurement Circuits

As mentioned above, fourteen signals for SAPF prototype and eight signals for CBAD prototype are measured. The measured channels are given above for both prototypes. The dc links of SAPF and CBAD are measured to charge dc buses according to their reference values. Three grid voltages are measured for both synchronization and protection against the grid voltage uncertainties. The grid-side SAPF currents of LCL filter are measured to control generated signals and the system protection. The source currents are measured to generated harmonic reference signals. Lastly, the capacitor currents of LCL filter are measured to be able applying active resonance damping methods.

In all measurement signals, AMC1xxx isolation amplifier series from Texas Instruments are preferred. These amplifiers are fully differential precision amplifiers. The input signal and output signal are separated by a barrier with silicon dioxide (SiO_2) material. This barrier provides galvanic isolation of up to 7 kV.

In SAPF measurement signals, AMC1100 amplifier is used. The AMC1100 is able for current and voltage measurement, where the input signals are connected directly to shunt resistors. The output of the AMC1100 can be adjusted either 3V or 5V through low-side supply. Moreover, the operation temperature of the AMC1100 ranges from -40 ^{0}C to 105 ^{0}C that is suitable for industrial applications (Texas-Instruments, 2014).

In CBAD measurement circuits, AMC13x1 e-metering amplifier series from Texas Instrument have been preferred. AMC1301 has been selected for AC measurement signals, which are the capacitor currents and the grid voltages. AMC1311 has been selected for dc voltage measurement because of its wider input range. Both AMC1301 and AMC1311 are isolated amplifiers with their outputs separated from the input circuitry through isolation barrier. This barrier provides galvanic isolation of up to 5 kV for AMC1301 and 7 kV for AMC1311 (Texas-Instruments, 2017; Texas-Instruments, 2018).

The functional block diagrams of AMC1100, AMC1301 and AMC1311 are demonstrated in Figure 4.8. It is seen from the figure that all amplifiers include a delta-sigma modulator input stage with an internal band-gap reference voltage and RC oscillator for clock generation. The input signal and clock are transmitted to output side and processed through an analog filter that is third-order for AMC1100 and fourth-order for AMC1301 and AMC1311. The outputs of all amplifiers are differential. The electrical characteristics of AMC1100, AMC1301 and AMC1311 are given in Table 4.12 (Texas-Instruments, 2014; Texas-Instruments, 2017; Texas-Instruments, 2018).

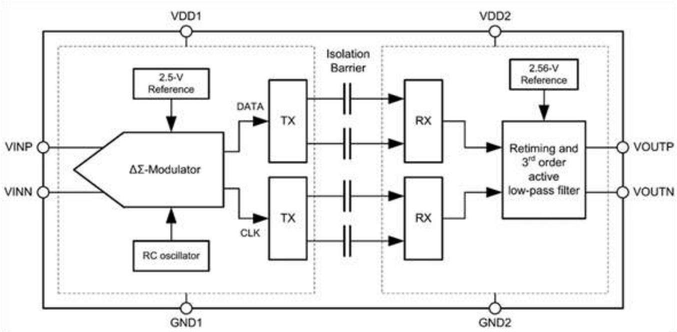

(a)

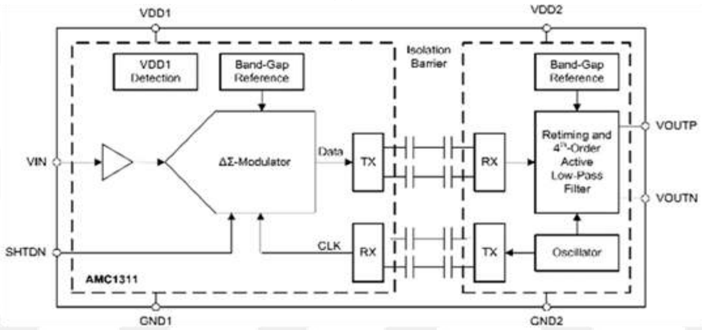

(b)

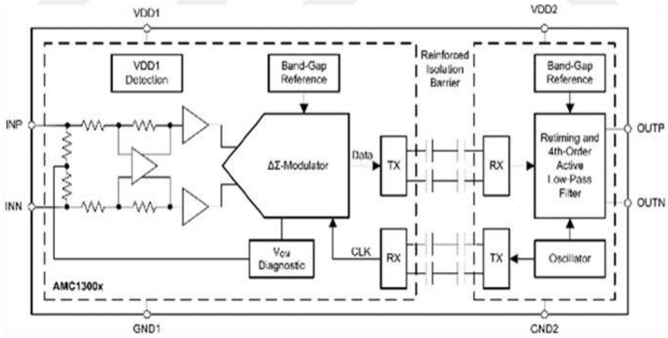

(c)

Figure 4.8. Functional block diagrams of (a) AMC1100, (b) AMC1301 and (c) AMC1311

Table 4.12. Technical specifications of AMC1100, AMC1301 and AMC1311

Parameter	Description	AMC1301	AMC1301	AMC1311	Unit
VINP-VINN	Differential input voltage	±0.25	±0.25	+2	V
V_{CM}	Common-mode operating range	VDD1		VDD1	V
V_{OS}	Input offset voltage	±0.2	±0.2	±0.4	mV
CMRR	Common-mode rejection ratio	95	100	-	dB
G	Nominal gain	8	8.2	1	
G_{ERR}	Gain error	0.05%	0.05%	0.05%	
	Output Noise	3.1	0.23	0.22	mV_{RMS}
PSRR	Power-supply rejection ratio VDD1/VDD2	80/61	96/86	65/85	dB
VDD1	High-side supply voltage	5	5	5	V
VDD2	Low-side supply voltage	5	3.3/5	3.3/5	V

Although different measurement amplifiers are used for SAPF and B-CBAD, their functionalities and operation principles are almost same. By this way, only SAPF measurements will be given in the following. But, the same block diagrams are applied for CBAD instead of a different amplifier.

Measurements of DC Voltage

Two different amplifiers are used for dc link measurement. While AMC1100 amplifier is used for SAPF, AMC1311 amplifier is selected for CBAD. Hereafter, only the measurement circuits for SAPF electronic control system are given.

The block diagram of dc link measurement circuit is shown in Figure 4.9. There are two measurement blocks for dc link measurement circuit. One voltage measurement is between the positive and midpoint terminals, and the second voltage measurement is between the midpoint and negative terminals. Same measurement circuit is applied for both measurements. The range of each dc link voltage measurement circuit is determined as 500V. Thus, the total dc link voltage is adjusted to measure 1000V.

In measurement circuit, dc link voltage is attenuated by a voltage divider. R_S and R_M are voltage divider resistors. In order to decrease loading, the resistance for measurement circuit, R_S, is offered to be higher than 1 MΩ. Thus, a resistance of 1.66 MΩ is selected. The shunt resistance, R_M, can be calculated as given in Eq. 4.24.

$$R_M \leq \frac{V_M \times R_S}{V_{dc,max} - V_M} \qquad (4.24)$$

Where, $V_{dc,max}$ is maximum DC link voltage to be measured. V_M is typical input voltage of AMC1100 or AMC1311, which is 250mV for AMC1100 and 2V for AMC1311 . According to parameter values for SAPF, the shunt resistance value is obtained as 830.4 Ω, and it is chosen 830 Ω that is available in the market. The input signal is filtered by RC filter to provide immunity to noise.

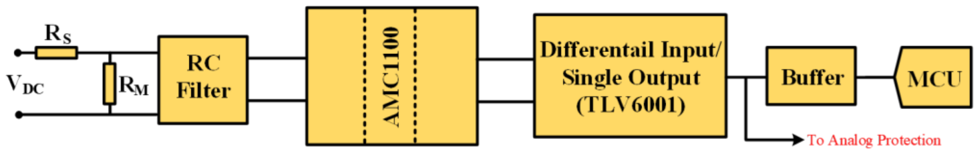

Figure 4.9. Block diagram of dc link voltage measurement

The outputs of the amplifiers are differential. The differential output is transformed to single-ended output by TLV6001 operational amplifier from Texas Instruments due to the limited ADC number of MCU. In addition, the signal is buffered via OPA4376 from Texas Instruments before entering ADC.

Measurement Circuit of Grid Voltages

The block diagram of the grid voltages are demonstrated in Figure 4.10. Three AC gird voltages are measured in the electronic control card. Similar to DC link voltage measurement circuit, R_S is chosen as 1.66 MΩ. To calculate the value of the shunt measurement resistor, Eq. 4.25 is used. The rms value of AC voltage measurement is specified as 280 V_{RMS}. The maximum peak voltage $V_{max,pk}$ is equal to 280*1.414 (395V). The shunt resistance R_M is calculated as 1051.3 Ω, and it is chosen 1000 Ω that is available in the market. The input signal is then filtered by RC filter to give immunity to noise.

$$R_M \leq \frac{V_M \times R_S}{V_{max,pk} - V_M} \tag{4.25}$$

The differential output signal of the measurement amplifiers are transformed to single-ended output by TLV6001 operational amplifier for ADC of MCU. An offset voltage 1.5V is added in TLV6001 amplifier to get the differential output in the range of 0-3V for MCU. Then, the signal is buffered via OPA4376 before entering ADC. Two TLV6001 amplifiers are used in AC voltage measurement circuit as seen from Figure 4.10. One is for control, and the other is for analog protection of SAPF system.

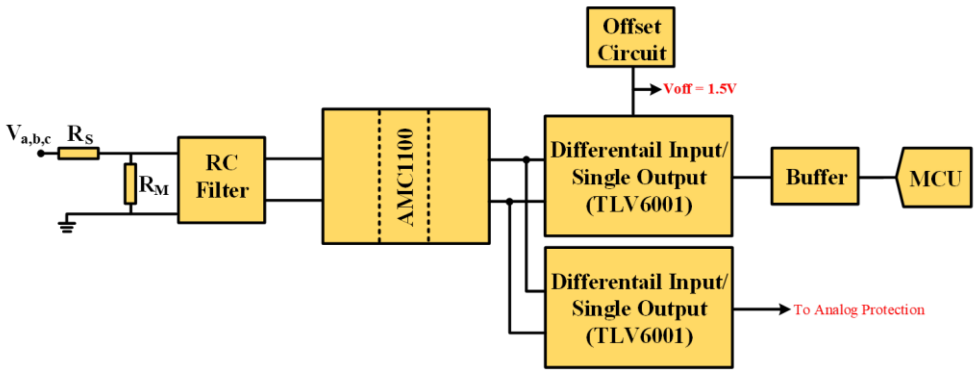

Figure 4.10. Block diagram of grid voltage measurement

Measurement Circuit of Source and SAPF Currents

The block diagram of source and SAPF currents measurement is shown Figure 4.11. The source current and SAPF current measurement circuits have similar configuration with the voltage measurement circuit. The difference is the input signal of current measurement is current signal. Besides, the only difference between source and SAPF currents is that SAPF current circuit has additional TLV6001 amplifier to convert single-ended output for analog protection of the system.

The source and SAPF currents are measured via LF-210s current transducers from LEM USA Inc. The output of LF-210s is current with a ratio of 1/2000. It is able to measure ±420A peak. It requires ±15V supply voltage. An isolated DC/DC converter from RECOM Company, REC7.5-1215DRW/H2/A/M, provides this supply. The measurement range for source SAPF currents is determined as ±100A peak. According to datasheet of LF-210s, maximum measuring resistance ($R_S + R_M$) is calculated as in Eq. 4.26.

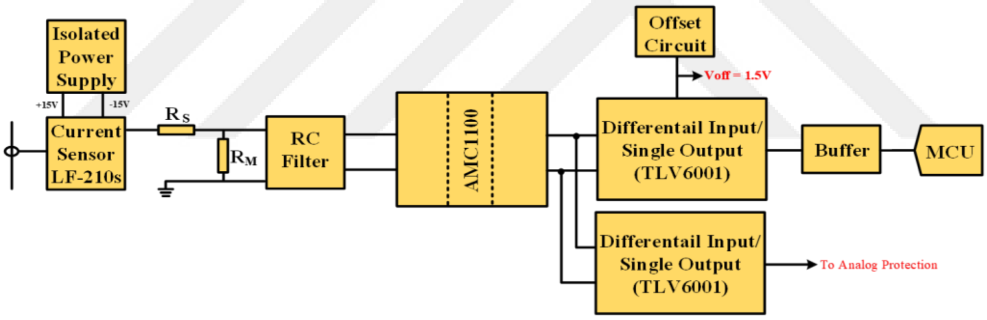

Figure 4.11. Block diagram of source and SAPF currents measurement

$$(R_S + R_M)_{max} = N_S \times \frac{U_{C,min} - 0.3\,V}{I_p} - R_{TS,max} - 4.1\Omega \qquad (4.26)$$

Where $U_{C,min}$ is mimimum transducer supply voltage, N_S is number of secondary turn and $R_{TS,max}$ is maximum resistance of secondary winding. According to the Equation, maximum measuring resistance is calculated as 250 Ω for $I_p = 100A$. It is selected as 154.7 Ω in order to operate in lower current range. The shunt resistance R_M is selected according to Eq. 4.27. V_M is AMC1100 input voltage 250 mV and $I_{p,max}$ is 100A. It is obtained as $R_M \leq 5\Omega$, and 4.7Ω is chosen from the market. In addition, R_S is selected as 150 Ω.

$$R_M \leq \frac{V_M}{I_{p,max}} \tag{4.27}$$

Measurement Circuit of Capacitor Current

The block diagram of capacitor current measurement of LCL filter is shown Figure 4.12. The measurement resistance of the capacitor current measuring circuit is directly connected in series with capacitor current. Thus, the capacitor current flows through the measuring resistance. The maximum capacitor current is obtained as 16A from simulation studies. Accordingly, the current range of capacitor current is determined to measure 25A for safe operation. Thus, the shunt resistance is obtained from Eq. 4.27 as 10 mΩ. The power dissipation on shunt resistor is calculated as 6.25 W. Two 20 mΩ with 5 Watt resistors, RS005 from Vishay, are paralleled to obtained 10 mΩ and required power level.

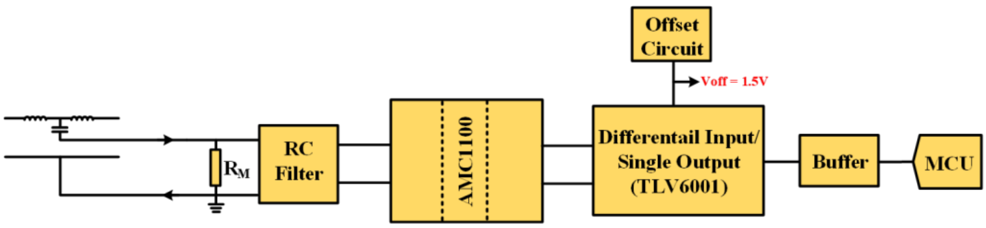

Figure 4.12. Block diagram of capacitor current measurement

4.4.3. Analog Protection and Fault Management Circuit

In the electronic control card of SAPF, two possible protections are provided, which are an algorithm embedded in MCU and analog protection. The analog protection circuit is performed for dc link voltage, grid voltage and SAPF current. The block diagram of analog protection and fault management circuits are demonstrated in Figure 4.13. The analog protection includes two main parts; a fault voltage level and comparator. In addition to these main parts, a precision rectifier is required for ac signal protection signals, namely for grid voltage and SAPF current. A voltage divider circuit determines the fault voltage level. In dc link measurement circuit, this fault voltage level is compared with the signal taken from TLV6001 output. In grid voltage and SAPF current protection circuit, the signals taken from TLV6001 are firstly rectified and then compared with the fault voltage level.

In fault management circuit as shown in Figure 4.13(c), it has two stages. These stages are fault latch/reset signal and trip signal generation. In first stage, the fault latch and reset signal are operated with NAND logic gate and NAND R/S latch. In second stage, the outputs of R/S latches of all fault signals are used to generate trip signal by AND logic gates.

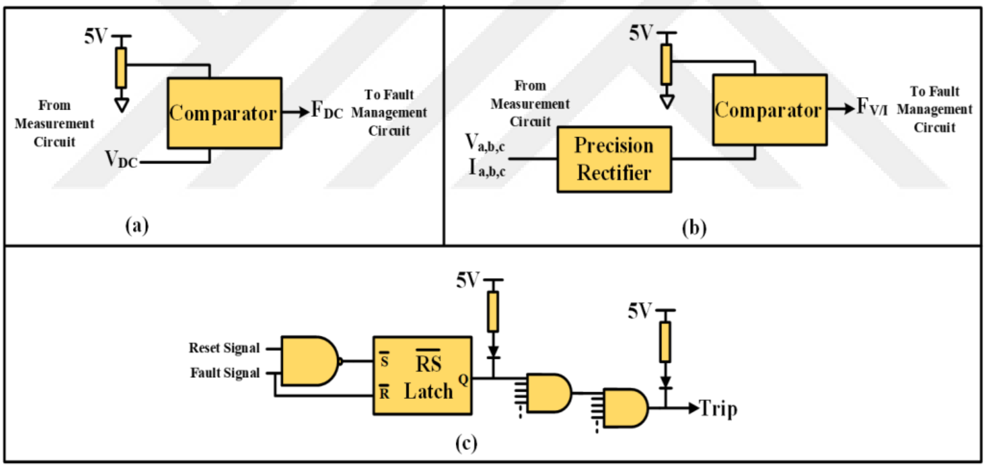

Figure 4.13. Block diagram of analog protection and fault management circuits
(a) DC link voltage protection,
(b) Grid voltage and SAPF current protection and
(c) Fault management

4.4.4. Digital Input/output Circuits

The digital input/output voltage level of DSP based MCU used in the Electronic control card is 3.3V. However, the voltage level of the external control signals has different values such as 5V and 24V. Thus, a voltage level transition is required in the electronic control card circuit. The voltage level transition is performed by using bus transceiver as shown in Figure 4.14. The digital output signals of MCU are increased to 5V from 3.3V for digital outputs. Besides, the digital input signals are reduced to 3.3V from 5V for digital inputs of MCU.

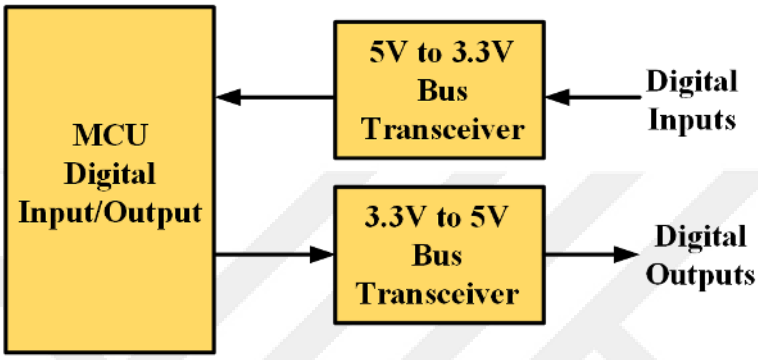

Figure 4.14. Block diagram of digital I/O circuits

The external control-command signals are realized with 24V. A voltage transition is performed from 5V to 24V and vice versa. The voltage transition is performed by using optocouplers. The aim of using optocouplers is to isolate and protect the electronic control card from any faults on control-command signals. The block diagram of voltage transition between 24V control-command signals and 5V digital I/Os are shown in Figure 4.15. In digital output signal circuit, a power amplifier is used with optocoupler in order to provide the required current value for driving relays with 24V.

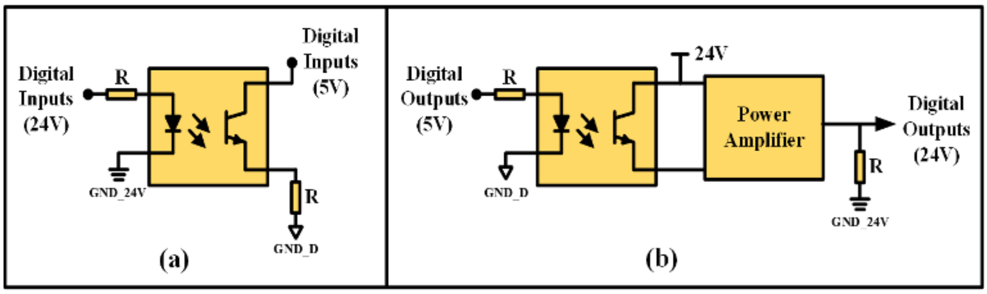

Figure 4.15. Block diagram of isolated voltage transition between 5V and 24V
(a) Digital input signal from 24V to 5V
(b) Digital output signal from 5V to 24V

4.4.5. Firing Circuits

The firing circuits transmits the voltage level of the digital output PWM signals to 15V from 5V and reduces the voltage level of the faults signals taken from IGBT driver to 5V from 15V. The block diagram of firing circuit is demonstrated in Figure 4.16. In order to perform isolation between IGBT driver and electronic control card, Isolated MOSFET driver and optocoupler for fault signal are used. This isolation prevents ground loop issues between the driver and electronic control card.

The firing circuit had been designed in previous by Dr. Adnan TAN and it is already available in Power Electronic laboratory of Electric and Electronic Engineering, Çukurova University. The available firing circuit is used to transmit PWM signals to IGBT driver.

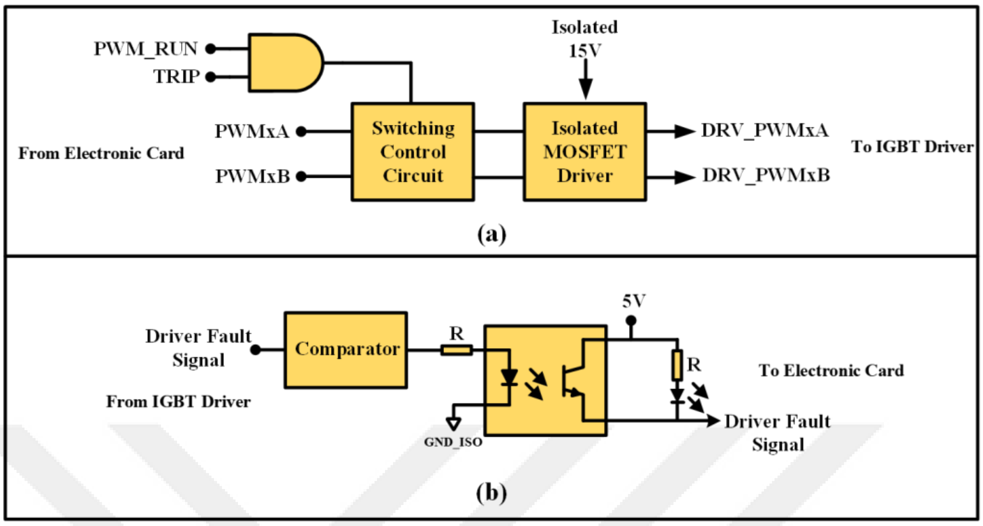

Figure 4.16. Block diagram of firing circuits
(a) PWM signals from 5V to 15V
(b) Driver fault signal from 15V to 5V

4.4.6. PCB Designs of Electronic Control Cards

PCB design of the electronic control cards of SAPF with LCL filter and CBAD prototypes have been performed through the use of Altium Designer software tool. Boards of the electronic control cards have been designed with two layers. While SAPF prototype is designed with single board, CBAD prototype is designed with 7 boards including power, MCU, firing, inputs/outputs, AC and DC measurement boards, and 1 main board which all boards hold on. CBAD prototype is designed in modular scheme for several purposes. The designed SAPF electronic control card with 2-D and 3-D view are illustrated in Figure 4.17. The detailed representation of electronic card of SAPF is shown in Figure 4.18. Besides, the designed CBAD electronic control card and its detailed representation are demonstrated in Figure 4.19 and 4.20, repectively.

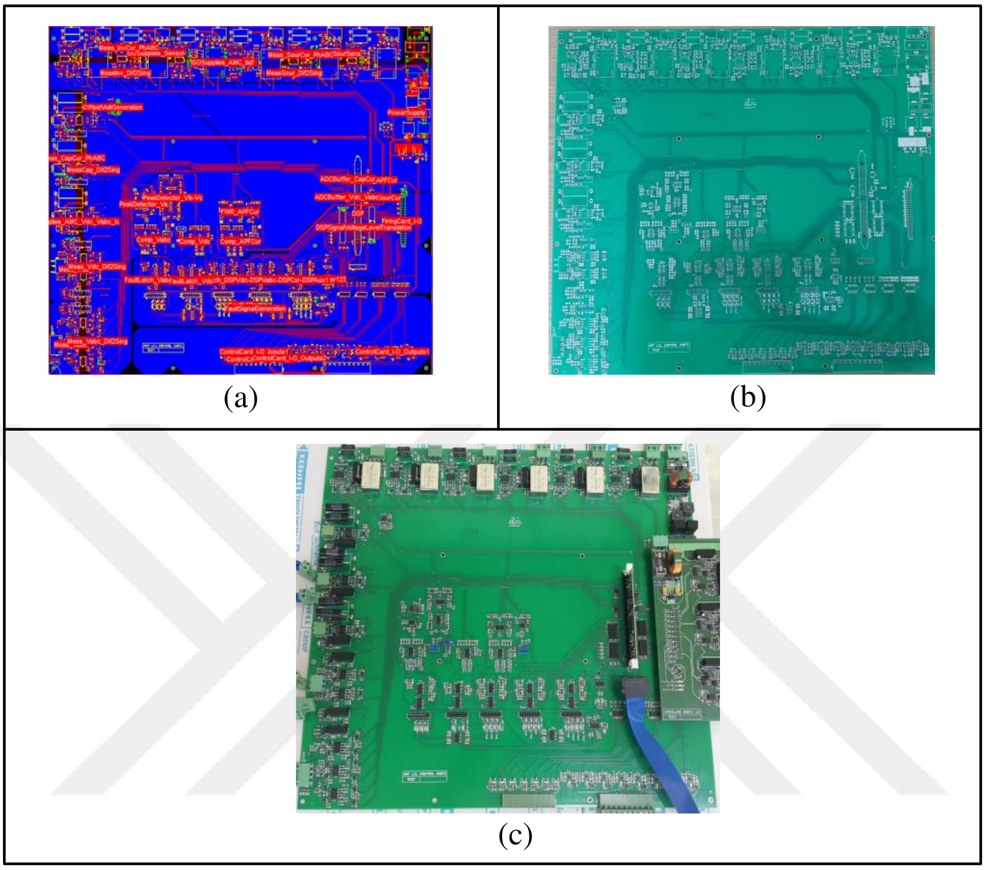

(a) (b) (c)

Figure 4.17. The designed PCB of electronic control card of SAPF and its implementation
(a) 2D layout of electronic control card
(b) 3D layout of electronic control card
(c) Photo of electronic control card

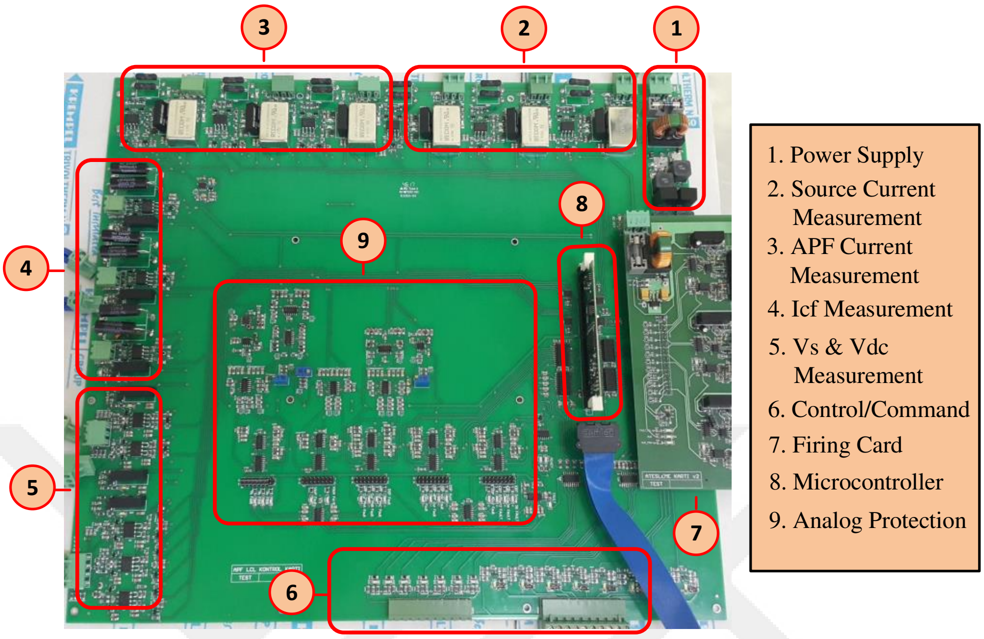

Figure 4.18. Detailed representation of SAPF electronic card

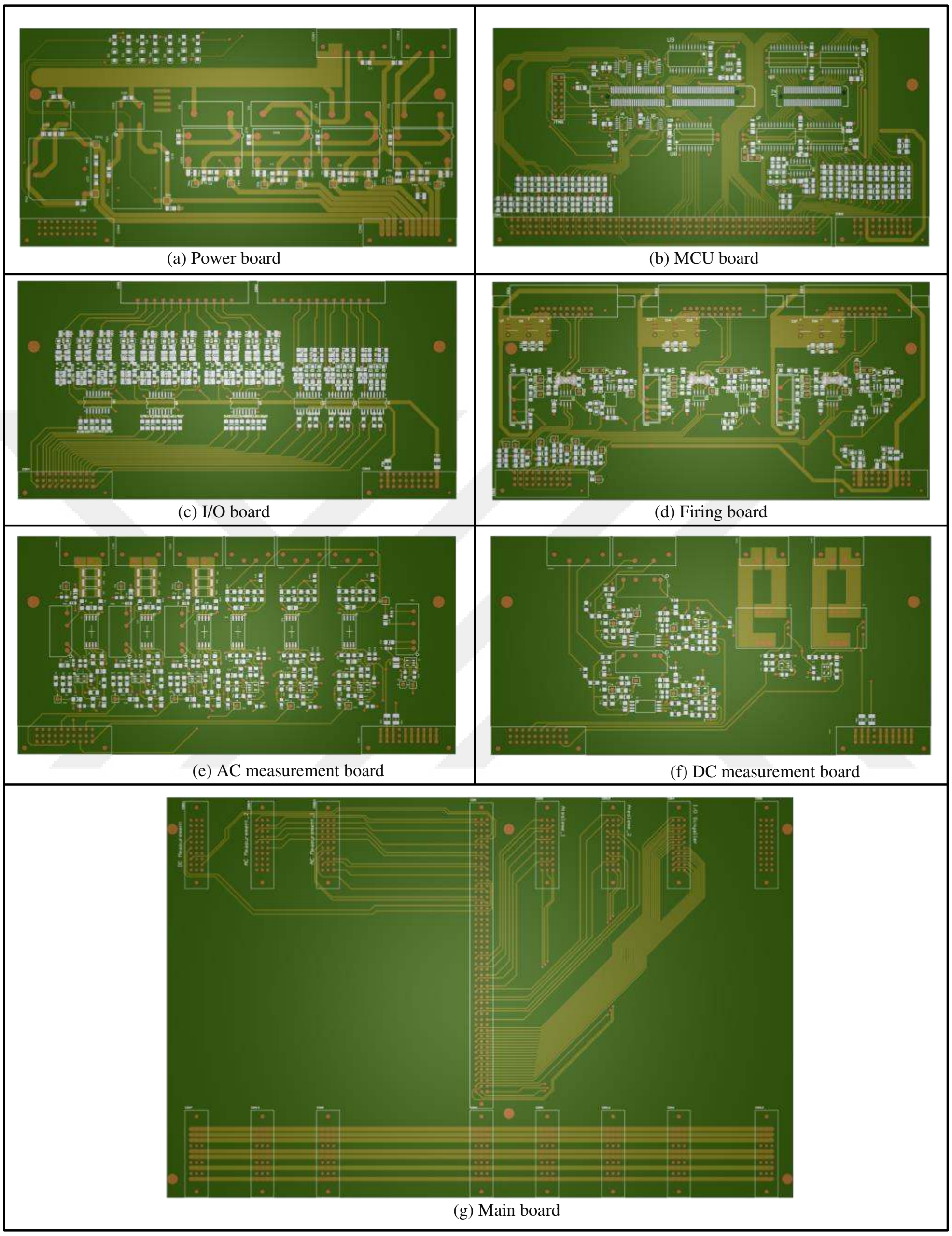

(a) Power board

(b) MCU board

(c) I/O board

(d) Firing board

(e) AC measurement board

(f) DC measurement board

(g) Main board

Figure 4.19. The designed PCBs of electronic control cards of CBAD

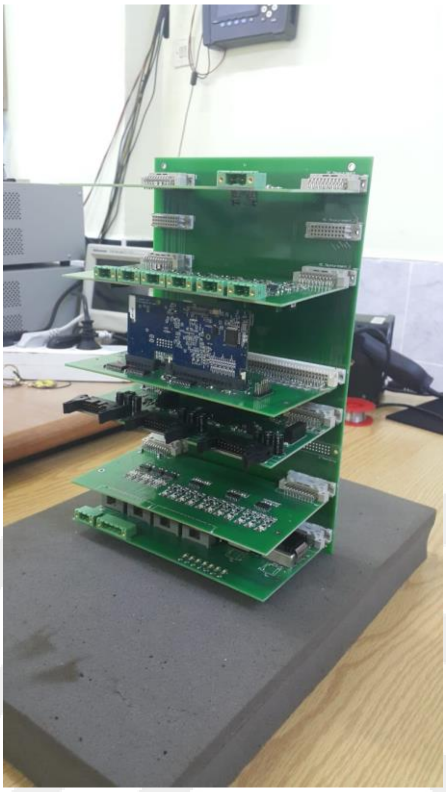

Figure 4.20. The implemented photo of CBAD electronic control card

4.5. Hardware Implementation of the System

The hardware implementation of SAPF with LCL filter and CBAD have been performed in Power Electronics Research Laboratory of Electrical and Electronics Engineering Department, Çukurova University. The hardware installation of SAPF with LCL filter and CBAD had been performed after all components of power circuit and electronic control card had been provided in terms of specifications by applying the following steps. The power circuit of implemented prototype and its picture are shown in Figure 4.21 and 4.22, respectively.

- The electronic control card was manufactured and electronic components were soldered on it.
- The function tests of electronic control card were realized.

- SAPF with LCL filter and CBAD circuits were installed with respect to electrical connections and mechanical design.

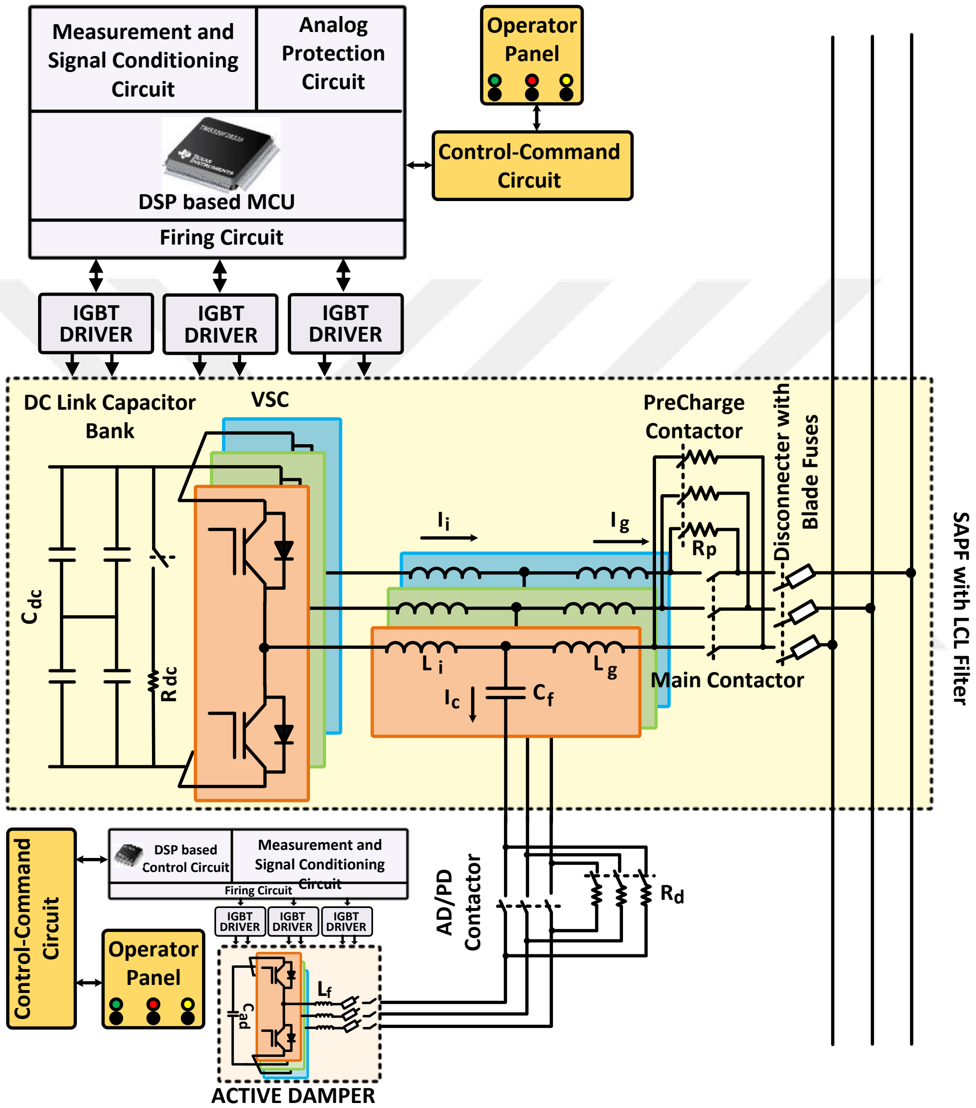

Figure 4.21. Three-phase power circuit of implemented prototype

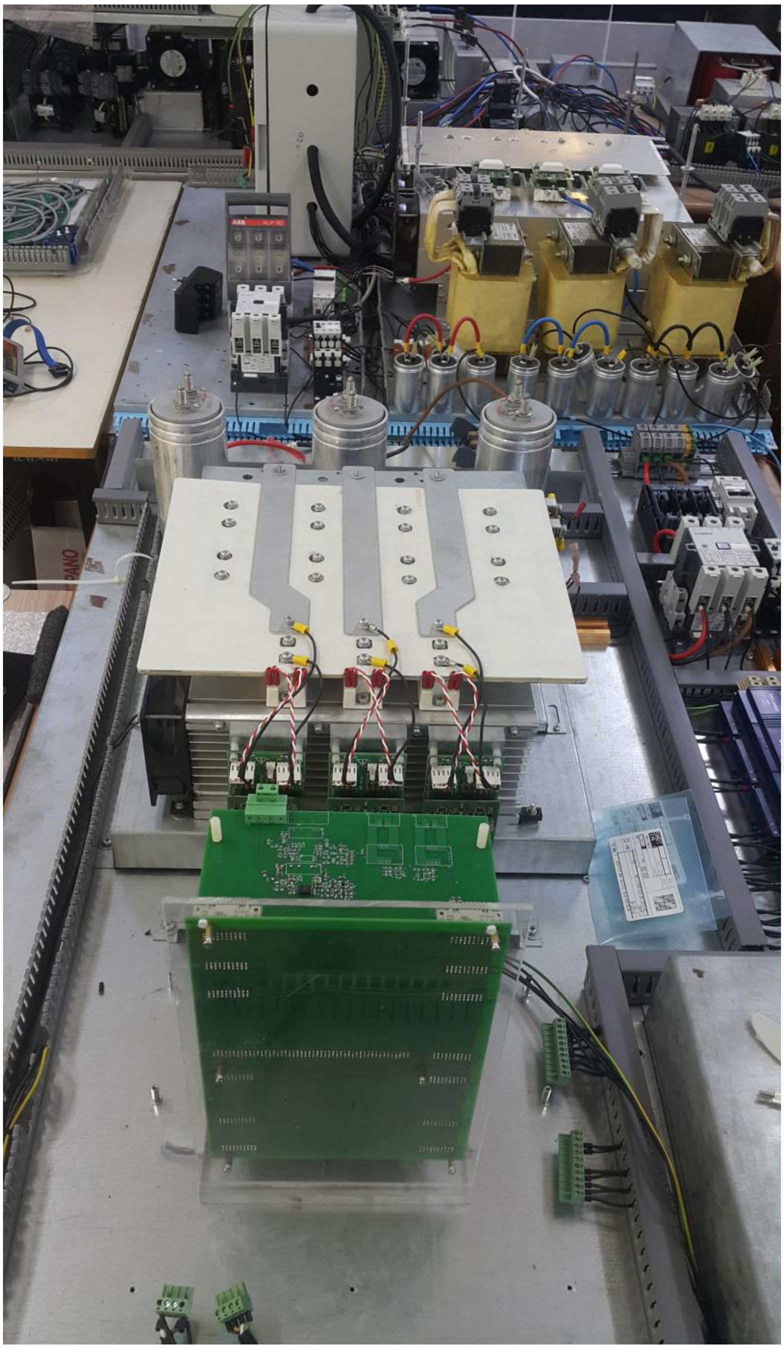

Figure 4.22. Picture of SAPF with LCL filter and CBAD prototypes

4.6. Software Development of Microcontroller

In thesis studies, two different microcontrollers from Texas Instrument are used for SAPF and CBAD prototypes. The embedded software of SAPF and CBAD prototypes are developed in C programing language through Code Composer Studio software development environment from Texas Instrument. The software of SAPF and CBAD include main and interrupt functions.

The CPU, peripherals and initialization of global variable values are performed in the main function. In the main function, the steps in Table 4.13 should be primarily ensured. In step-1, the system control registers are initialized to a known state. Besides, the watchdog timer is disabled. The system clock frequencies are adjusted to 150 MHz for SAPF and 100 MHz for CBAD. In addition, the clocks of peripherals are enabled for the used ones; the clocks of unused peripherals are disabled for reducing power dissipation. In step-2, the configuration of GPIOs should be performed according to usage purposes. All inputs/outputs should be carefully configured. The GPIO pins used as ePWM unit should be configured to function as ePWM, otherwise they are set as input by default. ePWM1, ePWM2 and ePWM3 are configured for both SAPF and CBAD prototypes. In step-3, interrupts of all peripherals are set to default values that are disabled and their flags are cleared. Besides, CPU interrupts are disabled and all flags are cleared. PIE vector table is also initialized. After initializing PIE vector table, interrupts that will be used in program algorithm should be enabled. Since the PIE vector table registers are protected, enabling codes must be written between EALLOW-EDIS typing. EALLOW allows to write the protected registers and EDIS disables to write. In experimental applications, ePWM1 timer interrupt is enabled for interrupt function. In step-4, ADC and PWM peripherals are initialized and configured. In the proposed systems, fourteen ADC channels for SAPF and seven channels for CBAD are utilized. Three ePWM peripherals are used in SAPF and CBAD prototypes. Each ePWM module has two outputs (EPWMxA and EPWMxB) that can be used either with single-edge and dual-edge symmetric operations. ePWM peripheral interrupt routine is used for sampling frequency. Besides, Start of Conversion (SOC) of ADCs are enabled by EPWM modules. ePWM modules are operated in synchronous mode. ePWM2 and ePWM3 clocks are synchronized with ePWM1 module. To adjust 10 kHz control frequency, ePWM module periods are set to 7500 for SAPF and 5000 for CBAD with up-down sampling mode. Thus, 150 MHz and 100 MHz clock frequencies with 15 kHz and 10 kHz ePWM timer frequencies generate interrupts every 100 us. In step-5, the interrupts that are used in the program should be enabled in PIE multiplexer block. All interrupts can be enabled and disabled within PIE block. In last step, idle loop, an infinite loop is performed. In addition, it is optional used to save power. The flowchart of main program for SAPF and CBAD prototypes is demonstrated in Figure 4.23.

In the interrupt function, all control algorithms and functions of the system such as start-up function, trip function, controller algorithms etc. are included. In both SAPF and CBAD prototypes, PWM interrupts are chosen for interrupt functions. The control algorithm software can be written after complete of initializing steps determined in Table 4.13.

Table 4.13. Software algorithm steps in main function

Stage	Description
Step - 1	Initialize the system control
Step - 2	Initialize GPIO
Step - 3	Clear all interrupts and initialize PIE vector table
Step - 4	Configure and Initialize all Device Peripherals
Step - 5	Enable Interrupts
Step - 6	IDLE loop

The steps of control algorithms written as given in Table 4.14. In step-1, fault flag is controlled whether enabled or not. Fault flag is enabled when a fault signal comes from driver or analog protection. Besides, DC link voltage, APF current and source voltage are measured and compared with limits determined. A fault signal is generated once the signals are out of the predefined limits and the critical parameters reset to initial values. In step-2, the measured signals are stored in ADC registers. The results are then appointed to predefined variables and each one is multiplied with its constant value in order to obtain the actual values. The constant values are obtained through applying different voltages at measurement points and getting the measurement coefficients for each channel. The measurement coefficients for SAPF and CBAD are given in Table 4.15. In step-3, the phase angle is obtained to synchronize to the grid, and the reference signals are calculated for harmonic currents and dc link voltage. In setp-4, if there are not fault and stop signals, then, the system becomes ready for start-up function. The start-up algorithm is vital. Because, the system may trip if the start-up function is not carefully determined. In SAPF prototype system, dc link is firstly pre-charged by uncontrolled rectifier. Then, it is charged to its reference value by a step function. After the dc link charge is completed, the harmonic compensation flag is enabled. During co-operation of SAPF and CBAD prototypes, dc link of CBAD is charged to the reference dc voltage value before activating dc link controller of SAPF prototype in order to prevent resonance issue. In step-5, ePWM timer interrupt flag must be cleared at the end of the program to be able getting the next interrupt. The flowcharts of SAPF and CBAD interrupt functions are illustrated in Appendix-B. In interrupt functions, there are some functions such as, PLL, reference, trip, etc. The aims of these functions are summarized in Table 4.16.

Table 4.14. Steps of Functions in PWM interrupt function

Stage	**Description**
Step - 1	Check Faults
Step - 2	Record ADC Results
Step - 3	PLL and Reference Signal Calculation
Step - 4	Start-up Function Procedure
Step - 5	Clear EPWM Interrupt Flag

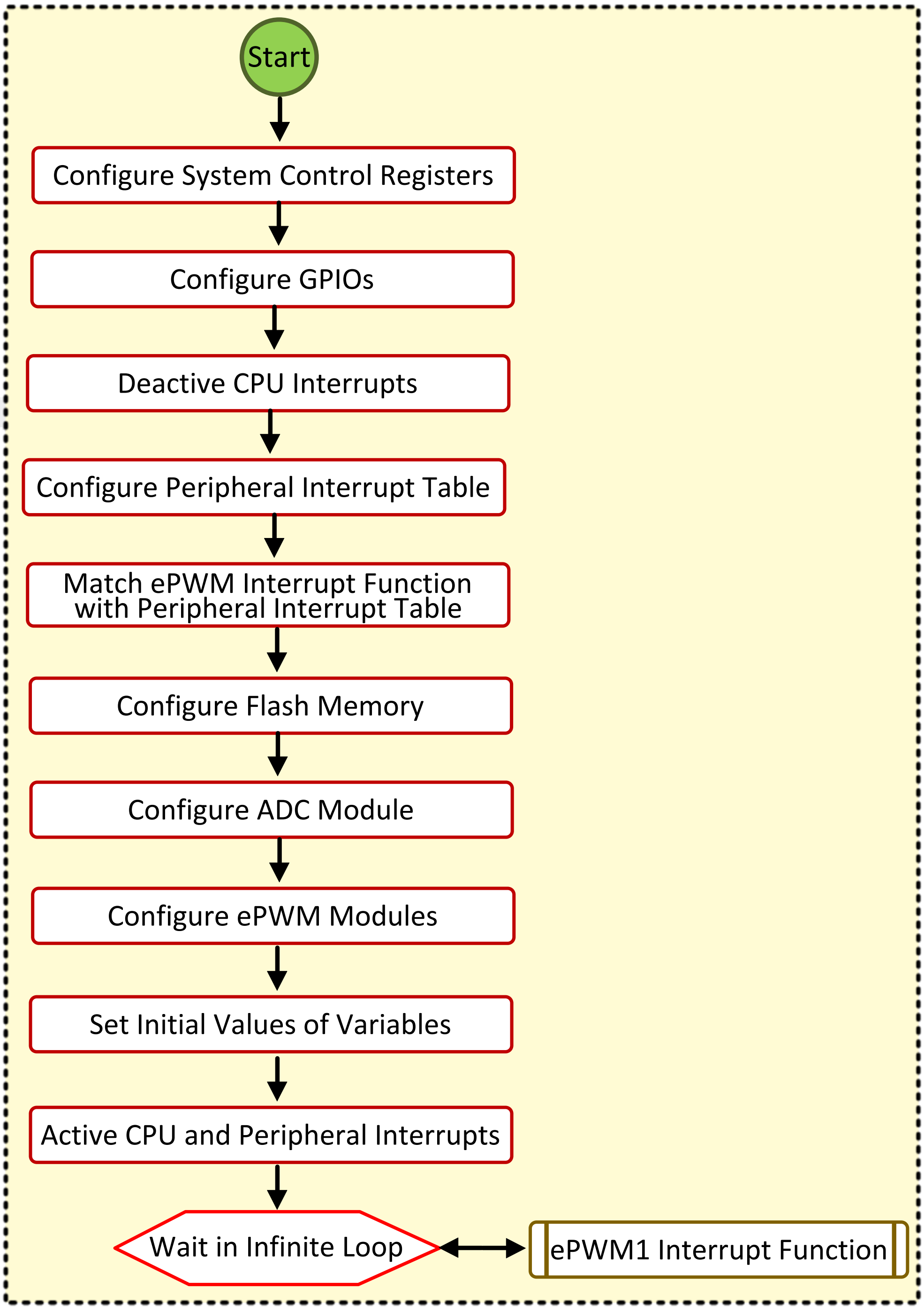

Figure 4.23. Flow chart of main program for SAPF and CBAD prototypes

Table 4.15. Measurement coefficients of Main converter and Auxiliary Converter

	Signals	Values
Main Converter	Source Voltages-Phase A/B/C	217,607/ 216,706/ 217,532
	Source Currents-Phase A/B/C	53,439/ 53,433/ 53,597
	APF Currents-Phase A/B/C	53,479/ 53,584/ 53,316
	Capacitor Currents-Phase A/B/C	17,544/18,002/17,638
	DC Link Voltages-Pos/Neg	210,386/ 211,593
Auxiliary Converter	Source Voltages-Phase A/B/C	305,905/307,869/306,500
	Capacitor Currents-Phase A/B/C	17,622/17,769/17,836
	DC Link Voltages-Pos/Neg	191,330/193,547

Table 4.16. Functions inside ePWM interrupts

Function	Description
Fault Detection	The measured values of dc link, SAPF current and grid voltages are compared with their predefined limits. Fault signal is generated if over limit is measured.
PLL	Generate phase angle to synchronize the grid.
Reference Generation	The reference signals for dc link and harmonic currents are generated for SAPF. Besides, reference signals for dc link and resonance currents are obtained for CBAD.
Start-up	The steps for SAPF or CBAD are performed. Pre-charge flag, main contactor, dc controller flags, harmonic compensator flag and resonance compensator flag are activated with setting.
Stop	PWM run and the critical variables are reset, main contactor is opened and discharge relay is closed.
Trip	Fault flag is set in addition to stop function
Reset	Fault signals are set and Fault flag is reset.
Control	The error and control signals are generated according to the steps of start-up for SAPF and CBAD prototypes.
PWM	IGBTs are modulated according to SPWM technique for both prototypes.

5. EXPERIMENTAL RESULTS

5.1. Overview of Experimental Studies

The experimental studies of the proposed system and conventional methods are performed in the Power Electronics Research Laboratory of Electrical and Electronics Engineering Department of Çukurova University. A Converter based Active Damper and Shunt Active Power Filter with output LCL filter prototypes are constructed in the laboratory. A nonlinear load group is set up in order to realize the functions of the constructed prototype systems.

The power circuit scheme and the photo of the constructed prototype systems are shown in Figure 5.1 and 5.2, respectively. The nonlinear load group consists of three pieces individual 5kW 3-ϕ bridge rectifiers including smoothing reactors in front of rectifiers. The rectifier loads are designed highly capacitive to raise the amplitude of low order harmonic current components

During the experimental studies, the waveforms of experimental result have been taken through Tektronix MSO3034 oscilloscope. Additionally, the PQ measurement results are recorded with Fluke 1760 power quality analyzer that is compatible with IEC 6100-4-30. The record time of voltage, current and power signals is performed by 200ms averages. The record time of harmonics measurement is realized with 3s averages. Single phase signals of supply, load and SAPF are measured with Fluke PQ analyzer to demonstrate the power and harmonics measurement at the same time. Phase A is chosen as reference measurement signal for supply, load and SAPF. To demonstrate the actual three phase power, the power measured phase is taken three times. THDs of source and load currents are obtained with Fluke 1760 up to 50^{th} harmonic components.

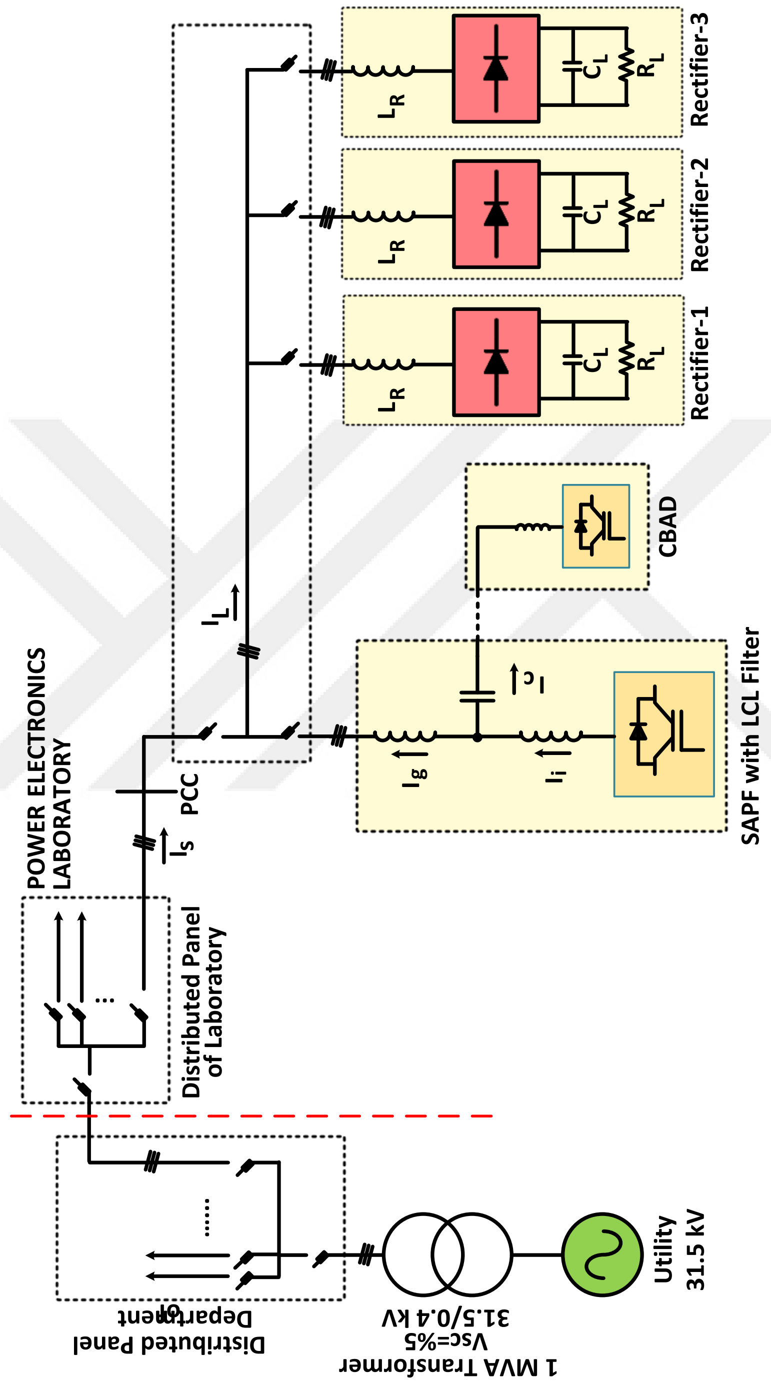

Figure 5.1. Power circuit scheme of experimental setup

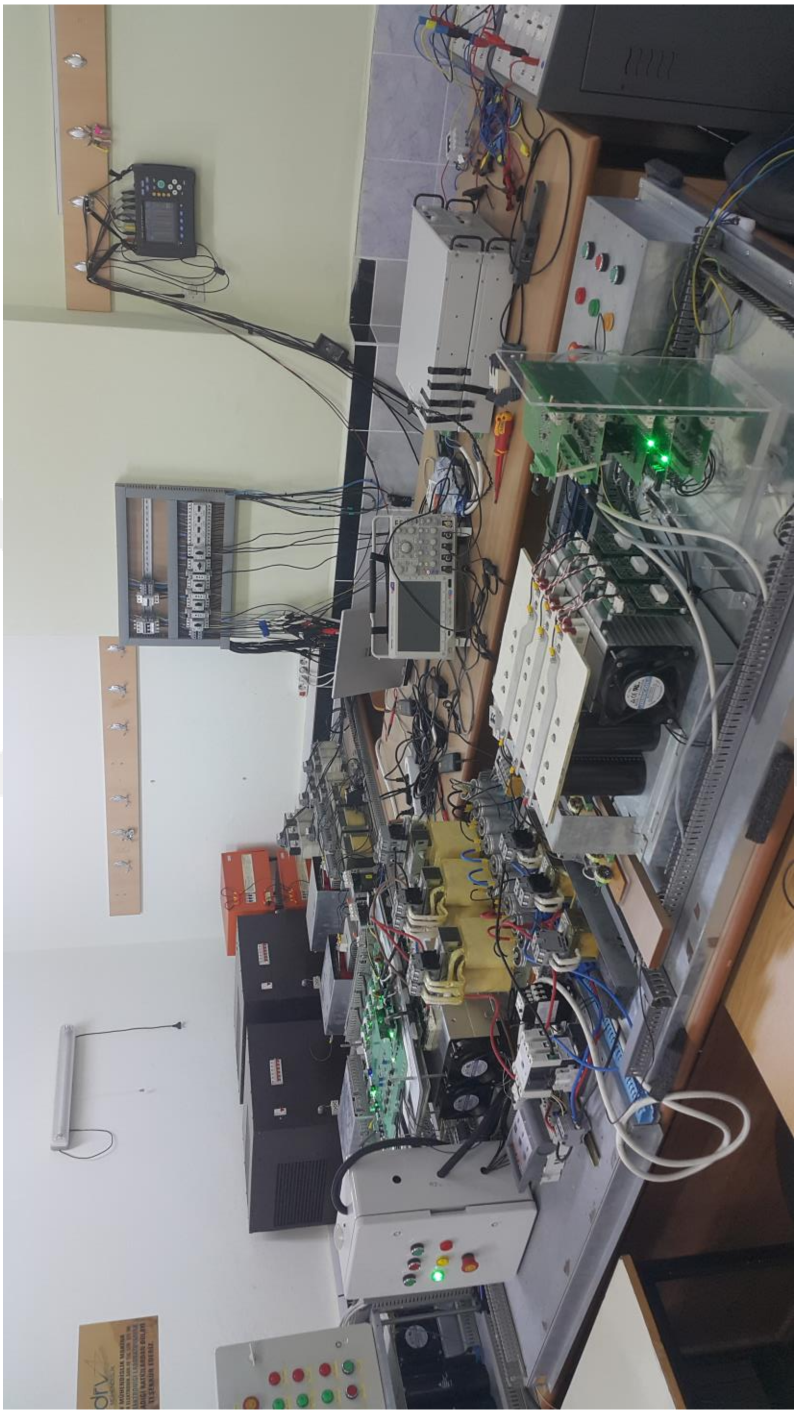

Figure 5.2. Photo of experimental setup

5.2. Start-up Procedure

In this section, the experimental results of implemented system are investigated during start-up. Two start-up cases are examined in experimental results. One start-up is examined for alone operation of SAPF with LCL prototype. And the other start-up is investigated during co-operation of SAPF with LCL and CBAD prototypes.

In the first case, the start-up procedure of SAPF with LCL filter consists of the pre-charge of the dc link, the activation of dc link controller and the current controller, successively. In the second case, the dc link controller of CBAD and the pre-charge of SAPF dc link are started at the same time. After that, the resonance controller of CBAD and the dc link charge controller are activated simultaneously. Then, the harmonic compensation controller is set to compensate harmonics.

5.2.1. Case 1: Start-up of SAPF with LCL Filter

In this procedure, in order to avoid excessive inrush current of the dc link capacitor, the dc link is firstly pre-charged to the peak value of the source voltage over an uncontrolled rectifier. The dc link pre-charge relay is turned on to charge the dc link of SAPF until reaching the peak value of the source voltage. This step takes almost 3-4 seconds. This time can be diminished by lower charging resistor value. After 4s, the pre-charge relay is opened and the main contactor is closed, simultaneously. After 0.5s of the previous step, the dc link controller is activated to regulate the dc link voltage to its reference voltage level. After 1.2s of the dc link controller activation, the harmonic compensation controller is activated to start the harmonic compensation. The start-up of SAPF with LCL filter is shown in Figure 5.3.

The start-up of the dc link controller is presented in Figure 5.4 with the source voltage and current, SAPF grid-side current and the dc link voltage. After activation of the dc link controller, the dc link controller has hold the dc link voltage at 700V with under 5% overshoot.

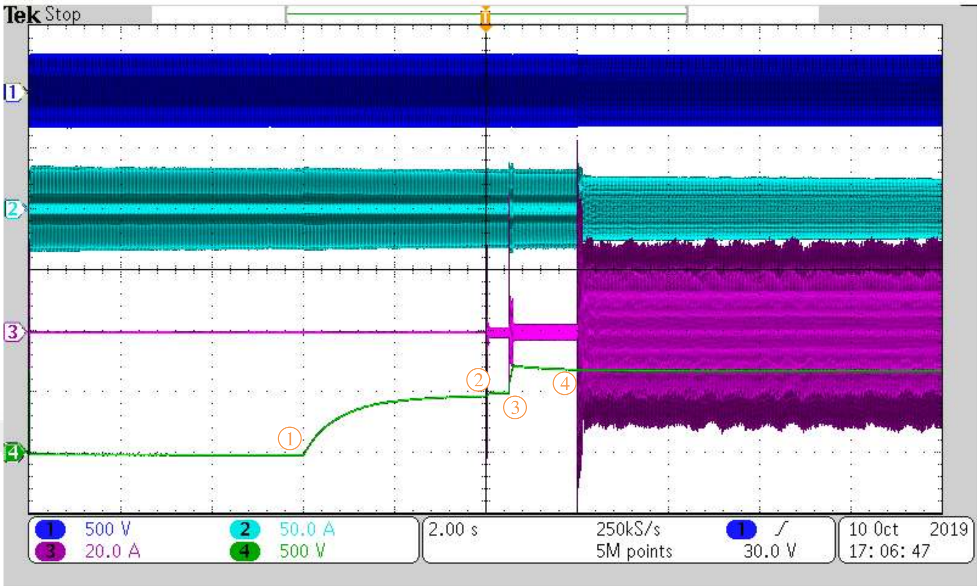

1. Pre-charge, 2. Main contactor closed, 3. DC link control and 4. Harmonic compensation control

Figure 5.3. Start-up SAPF with LCL filter

SAPF with LCL filter is ready to activate the harmonic compensation after providing the required dc link voltage reference by the dc link controller. The harmonic compensation start-up is illustrated in Figure 5.5 with the waveforms of the source voltage, source current, SAPF grid-side current and the dc link voltage. It can be seen from the experimental waveforms that an oscillation on dc link occurs once the harmonic compensation controller is activated. However, the oscillation on dc link is regulated by the dc link controller under 40ms with 1-2% overshoot. The ripple of dc link voltage is under 10V - 1.4% at full rating of SAPF in the steady state condition. The harmonic controller maintains the steady state condition in the harmonic compensation under 100ms (5 period). In the steady state operation following the start-up procedure, SAPF with LCL filter prototype diminishes source current THD value from 37% to 3.1%. The detailed investigation of the prototype with various damping methods are presented in the following sections.

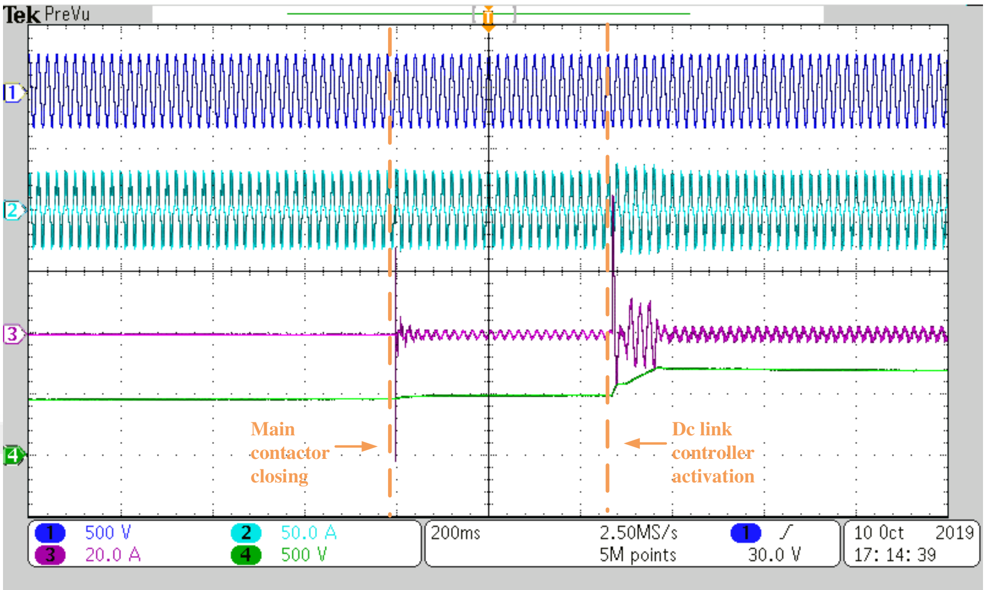

Figure 5.4. Source voltage, source current, SAPF current and dc link voltage waveforms during activation of dc link voltage controller

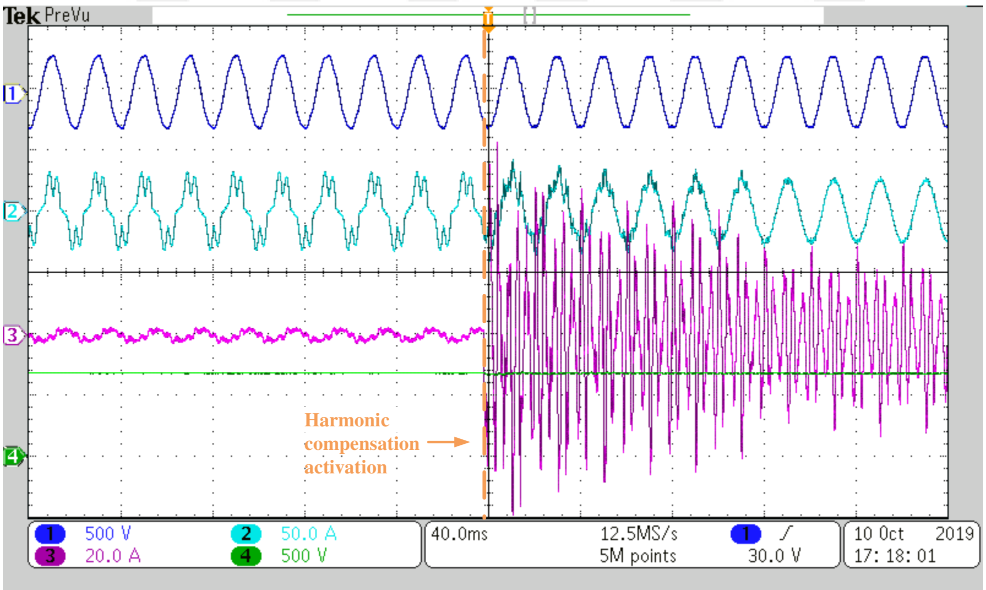

Figure 5.5. Source voltage, source current, SAPF current and dc link voltage waveforms during activation of harmonic compensation controller

5.2.2. Case 2: Start-up of SAPF with CBAD

In this start-up case, the start-up procedures of SAPF with LCL filter and CBAD are presented. The start-up procedure of CBAD is started by sending a start signal from SAPF prototype when the pre-charge of dc link is turned on. The dc link voltage of CBAD must be kept to its reference voltage level before SAPF prototype activates dc link controller in order to suppress the resonance of LCL filter. The start-up of the whole system is demonstrated in Figure 5.6. The pre-charge of main converter dc link, SAPF, is firstly started. After 1s than closing the dc link pre-charge relay, dc link controller of CBAD is activated to charge dc link of auxiliary converter, CBAD, to it reference voltage level. After 1.5s than activating dc link controller of CBAD, the contactor of SAPF is closed and after 0.5s the dc link controller of SAPF is activated. The harmonic compensation controller is activated following the dc link controller activation by 1.5s. The dc link of CBAD, as seen from start-up operation, has an oscillation with 5-10V. This oscillation realizes at 2. orders of fundamental frequency because unbalanced grid voltages and filter component values cause unbalanced capacitor current flowing, which affects the digital notch filter performance adversely.

The start-up of dc link controller of CBAD is presented in Figure 5.7 with SAPF grid-side current and dc link voltage, capacitor current and CBAD dc link voltage. After activation of CBAD dc link controller, dc link voltage of CBAD is kept at the desired reference voltage level 100V with under 10% overshoot.

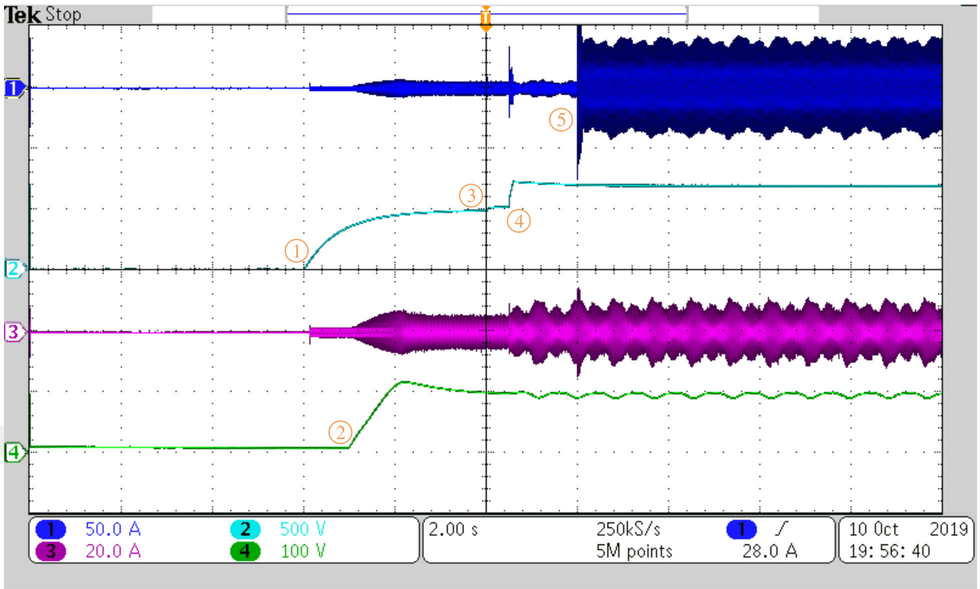

1. Pre-charge of SAPF dc link, 2. DC link control of CBAD, 3. Main contactor closed,
4. DC link control of SAPF and 5. Harmonic compensation control

Figure 5.6. Start-up of SAPF with LCL filter and CBAD prototypes

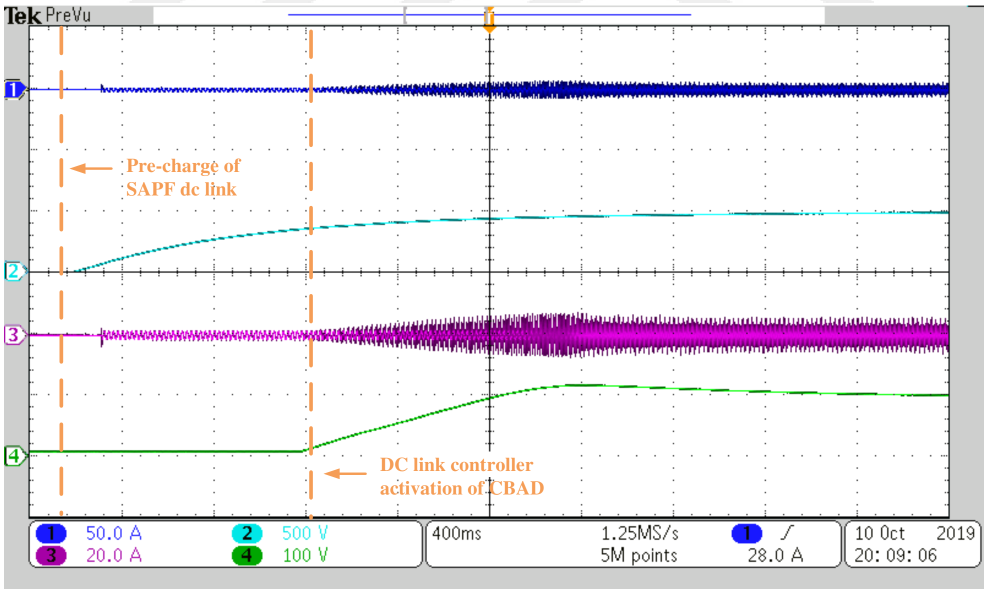

Figure 5.7. SAPF grid-side current, SAPF dc link voltage, capacitor current and CBAD dc link voltage waveforms during activation of CBAD dc link controller

After maintaining the required voltage level of CBAD, SAPF with LCL filter prototype is, by the way, ready to operate dc link and harmonic compensation controllers, respectively. The experimental result waveforms during the activations of dc link controller and harmonic compensation controller are demonstrated in Figures 5.8 and 5.9, respectively. SAPF with LCL filter shows similar performance with alone start-up operation during activations of dc link controller and harmonic controller. In the steady state operation following the second start-up procedure, SAPF with LCL filter prototype drops source current THD value from 37% to under 3.2%.

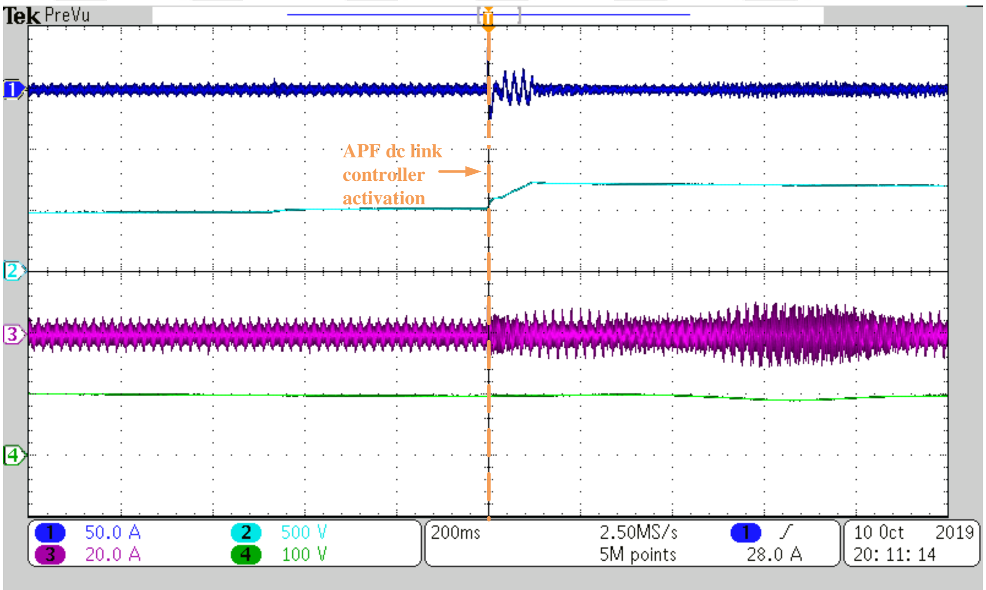

Figure 5.8. SAPF grid-side current and dc link voltage, capacitor current and CBAD dc link voltage waveforms during activation of SAPF dc link controller

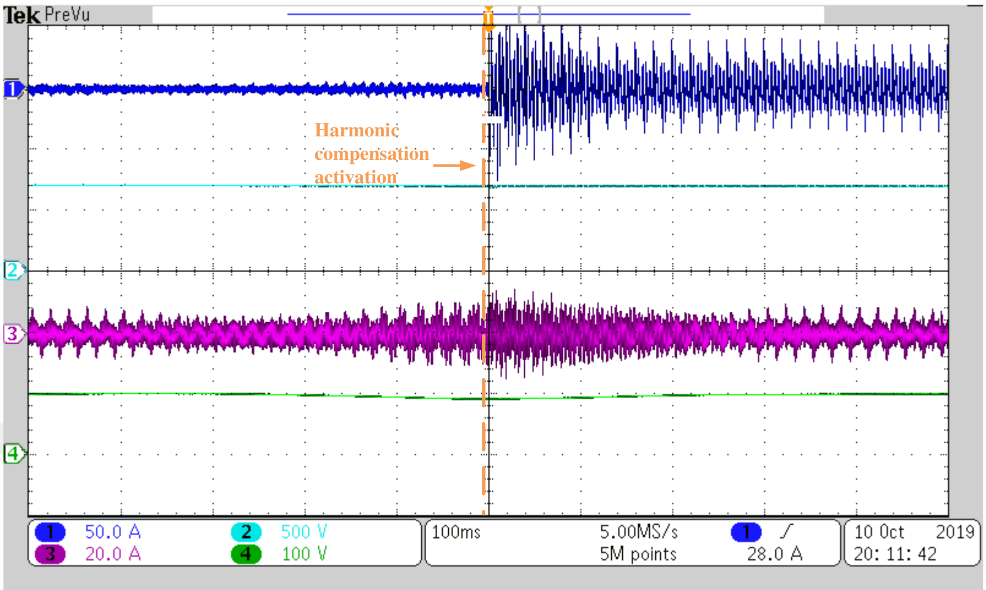

Figure 5.9. SAPF grid-side current and dc link voltage, capacitor current and CBAD dc link voltage waveforms during activation of harmonic compensation controller

5.3. SAPF with Different Output Filters and Damping Methods for LCL filter

In this section of experimental study, the performance results of SAPF is investigated and assessed through single L filter, LCL filter without damping and with three different damping methods including simple resistor PD, capacitor current feedback AD and CBAD. The investigated cases are summarized as follows;

Case I: SAPF with Single L filter.

Case II: SAPF with LCL filter without resonance damping.

Case III: SAPF with LCL filter damping through series resistor.

Case IV: SAPF with LCL filter damping through capacitor current feedback.

Case V: SAPF with LCL filter damping through the proposed CBAD.

In order to demonstrate the effect of LCL filter, same inductance values for single L filter and LCL filter are selected. Moreover, the controller parameters are set same for all cases.

5.3.1. Single L Filter

In this case, the performance of SAPF with output single L filter is presented and analyzed. The source voltage and current waveforms are illustrated in Figure 5.10. The waveforms of the source, load and SAPF currents and dc link voltage are demonstrated in Figure 5.11. Besides, SAPF current waveform with FFT spectrum is shown in Figure 5.12. In addition, the harmonic spectrums of load and source currents are shown in Figures 5.13 and 5.14, respectively. The dynamic response of SAPF with single L filter is demonstrated in Figure 5.15. The active power trends of source, load and SAPF and THD trends of source and load currents during harmonic compensation are demonstrated in Figures 5.16 and 5.17, respectively.

The performance of SAPF with single L filter during harmonic compensation are clearly seen from the oscilloscope waveforms and harmonic spectrum. The dominant low order harmonic components are compensated so that satisfying the specifications. The dominant low order harmonics are compensated with the rates of 96.97%, 97.14%, 86.21% and 80.45% for 5th, 7th, 11th and 13th harmonics, respectively, as given in Table 5.1. The harmonic compensation performance may be sufficient for low order harmonics in SAPF with LCL filter. However, single L filter cannot perform sufficient performance to reduce switching ripple harmonic components as seen from SAPF current and FFT spectrum in Figure 5.12. The switching ripple harmonic components are seen in switching frequency and its multiples. It can be seen from Figure 5.12 that the switching ripple harmonics are almost 1 A at 10 kHz, 0.6 A at 20 kHz and 0.2 A at 30 kHz. The switching ripple harmonics can be decreased further by increasing the inductance value. However, increasing the inductance value will adversely affect the compensation performance of low order harmonics and result in a bigger volume of system. The increase of inductance value also will necessitate higher DC link voltage level which increases the switching losses and the ratings of capacitor bank and IGBTs. The THD spectrum of load and source currents are illustrated in Figure 5.13 and 5.14, respectively. The THD level of source current is nearly decreased to %3.3 from %37.5.

The dynamic response of SAPF with single L filter is shown in Figure 5.15. DC link voltage, source, load and SAPF currents are demonstrated in the figure. In this operation mode, two bridge rectifiers have been energized. The third bridge rectifier is then energized for the investigation of load change. It can be seen that SAPF with L filter

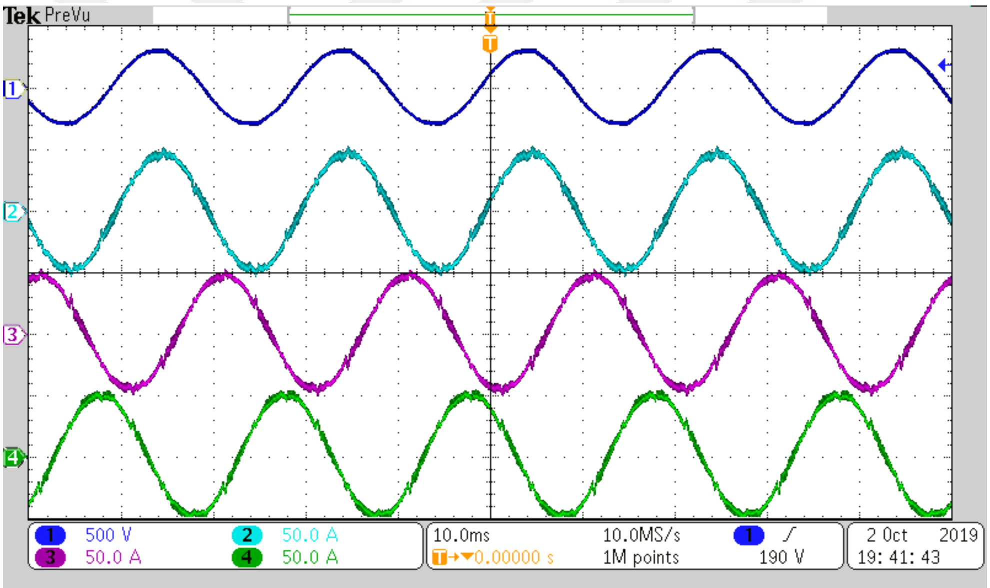

Figure 5.10. Source voltage and current waveforms during operation with single L filter

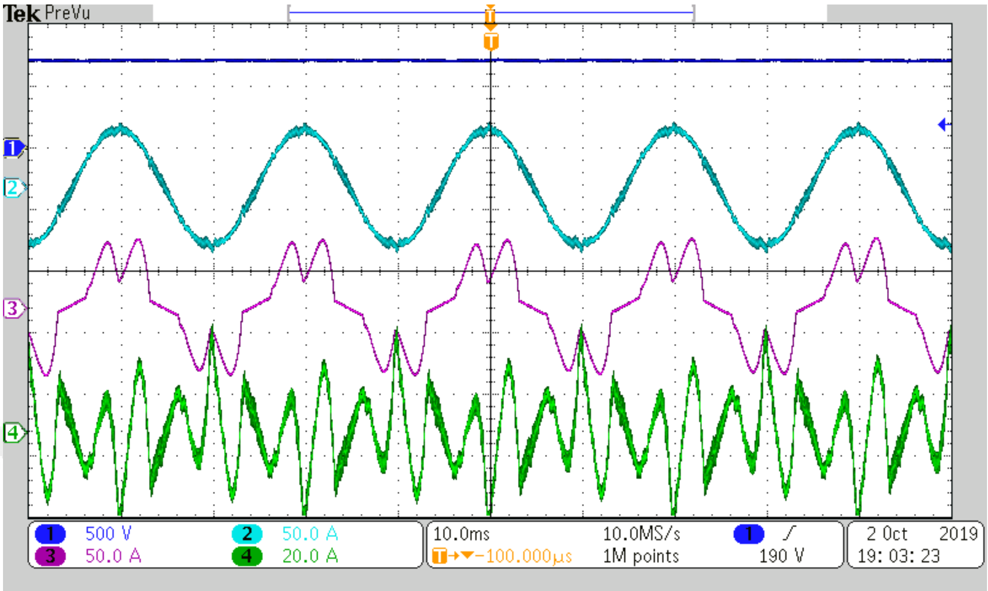

Figure 5.11. DC link voltage and current waveforms during operation with single L filter

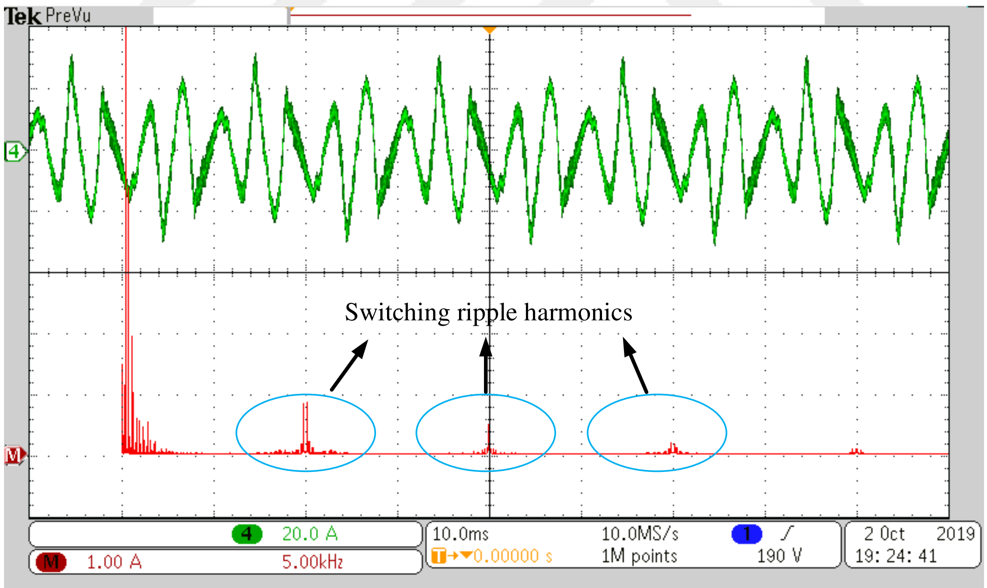

Figure 5.12. SAPF current and FFT spectrum during operation with single L filter

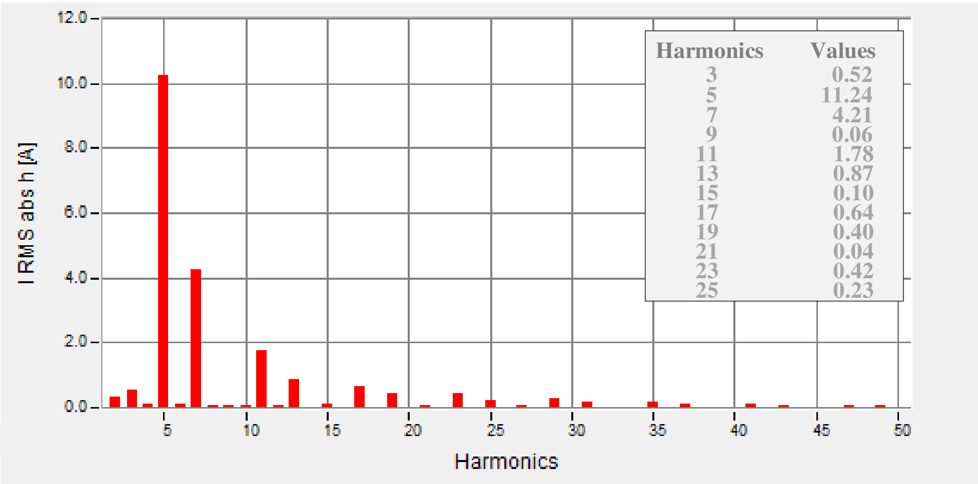

Figure 5.13. Load current harmonic spectrum during operation with single L filter

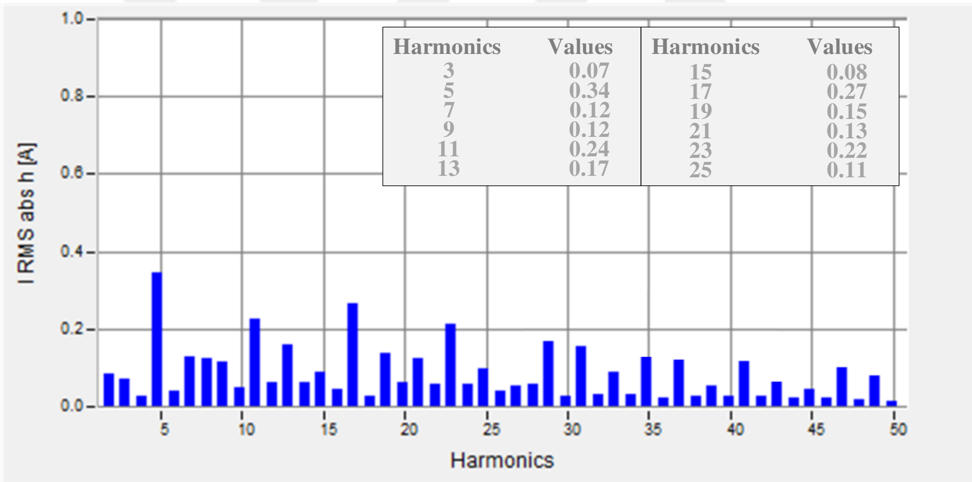

Figure 5.14. Source current harmonic spectrum during operation with single L filter

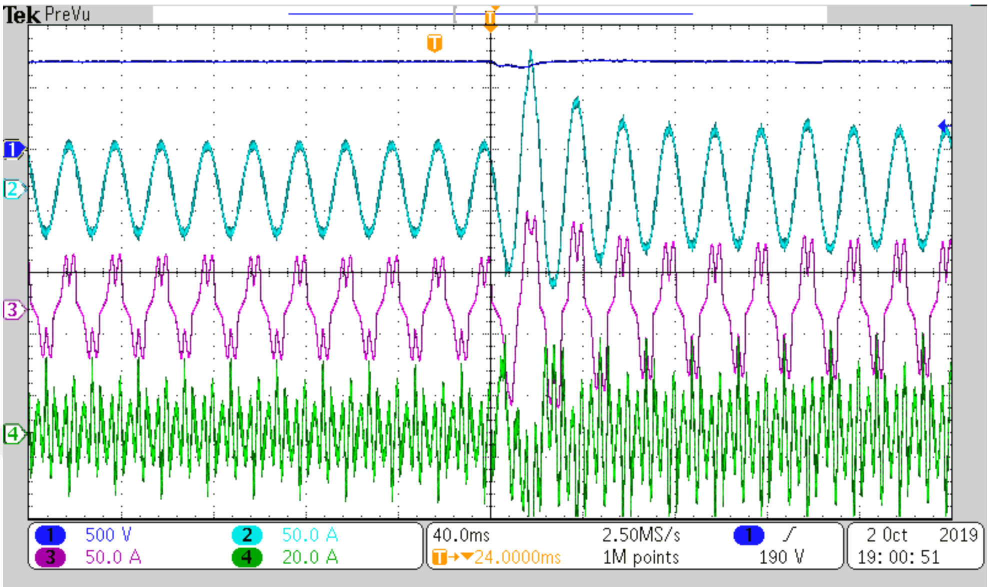

Figure 5.15. DC link voltage and current waveforms during dynamic operation with single L filter

Table 5.1. Harmonic levels in load and source current and compensation performance of SAPF with L filter

Harm. Order	Load current	Source Current	Comp. Perform.
5	11.24	0.34	96.97%
7	4.21	0.12	97.14%
11	1.78	0.24	86.51%
13	0.87	0.14	83.90%
17	0.64	0.27	57.81%
19	0.40	0.15	62.50%
23	0.42	0.22	47.61%
25	0.23	0.11	52.17%

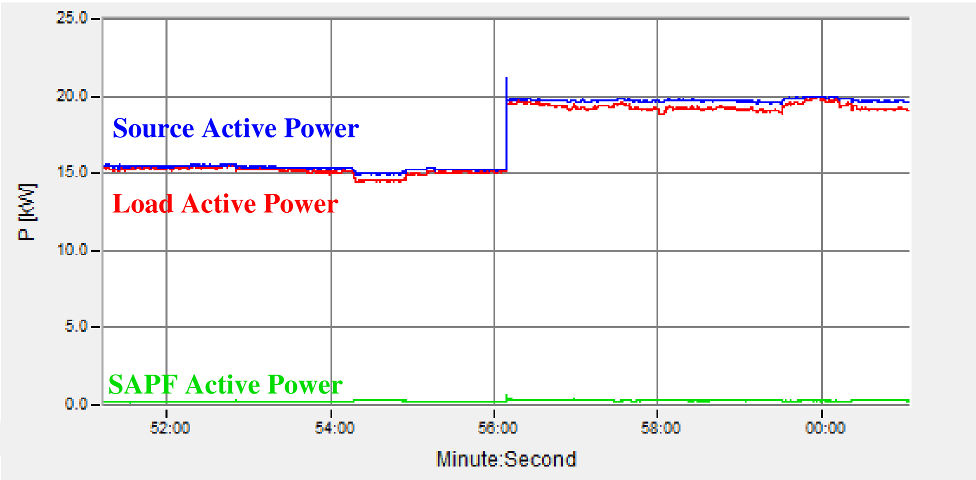

Figure 5.16. Active power trends of source, load and SAPF during operation with single L filter

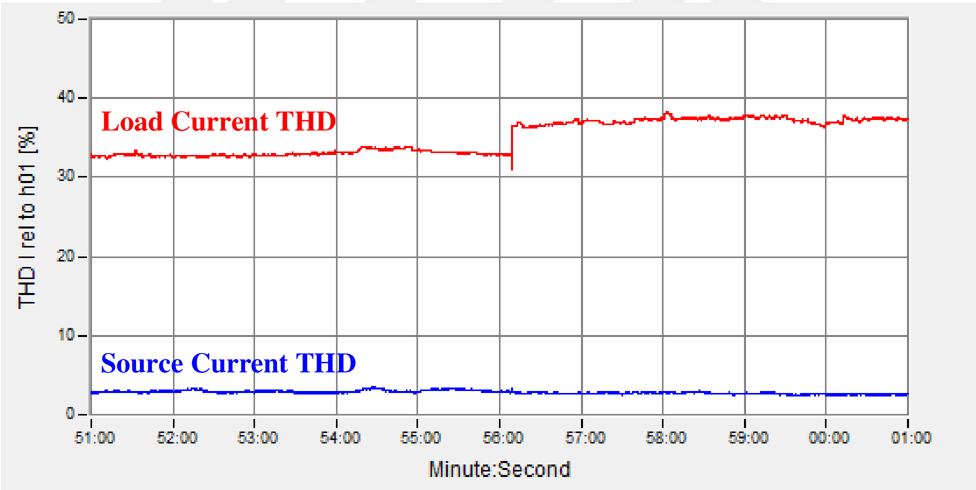

Figure 5.17. THD trends of source and load currents during dynamic operation

5.3.2. LCL filter without Resonance Damping

In this case, the impact of LCL filter on high frequency harmonics is investigated. By this way, LCL filter without resonance damping is applied with SAPF during harmonic compensation. The SAPF current and FFT spectrum is shown in Figure 5.18. It is illustrated from the waveform that LCL filter effectively mitigates the high frequency switching ripple harmonics. The switching harmonics around 10 kHz side are 0.17 A, which are reduced by 84%. However, LCL filter adversely has a resonance at almost 3.48 kHz, satisfying the theoretical analyses mention in Section 3.3. The resonance current reaches nearly 0.44 A. The impact of resonance is suppressed by inductor and line resistances, where these resistances show PD effect on the system. Otherwise, a higher resonance current would occur on the system.

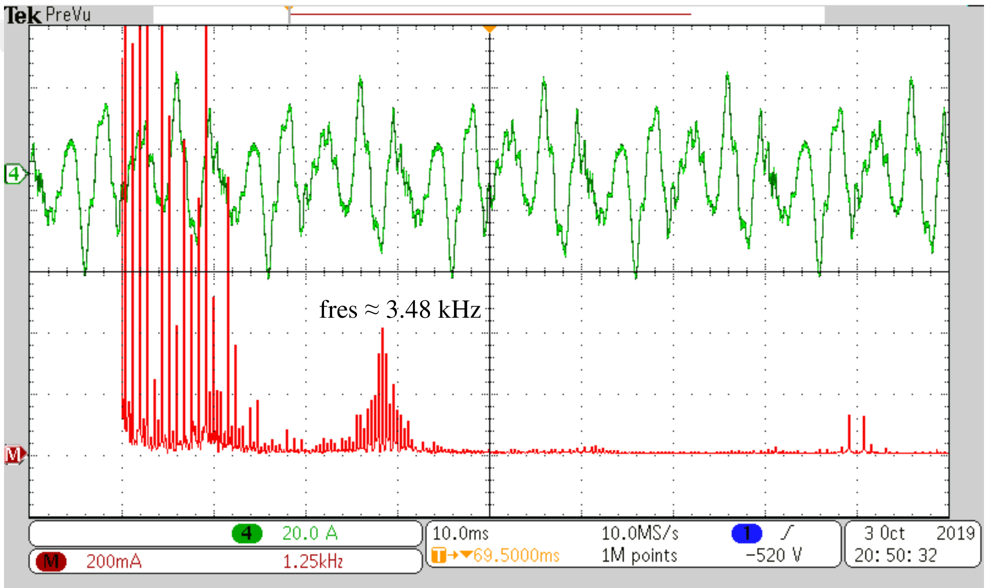

Figure 5.18. Grid-side current waveform and FFT spectrum without damping of LCL filter

5.3.3. LCL Filter with Single Series Resistor Passive Damping

In this case, the harmonic compensation performance of SAPF with LCL filter damped through simple resistor method (Figure 3.14) presented in Section 3.4.1 is examined. The source voltage and current waveforms are demonstrated in Figure 5.19. The waveforms of DC link voltage and source, load and SAPF currents are shown in Figure 5.20. The inverter-side and grid-side currents with their FFTs are given in Figures 5.21 and 5.22, respectively. In addition, the harmonic spectrums of load and source currents are demonstrated in Figure 5.23 and 5.24, respectively. The dynamic response of SAPF with LCL filter damped by simple series resistor is shown in Figure 5.25. The active power trends of source, load and SAPF with passively damped LCL filter is shown in Figure 5.26. Besides, the THD trend of load and source currents are given in Figure 5.27.

The experimental results show that the resonance of LCL filter has been damped by adding simple resistor series to the filter capacitor. The resonance components are suppressed by 82%. In the contrary, adding resistor series with capacitor leads to an amplification of the switching ripple harmonics. In this case, the switching ripple harmonics around 10 kHz and 20 kHz sidebands are 0.21A and 0.07A, which are suppressed by 73%. The resonance can be further suppressed by increasing the resistor value. However, the higher the resistance value is, the more power losses and the lower reduction of the switching harmonics are. Therefore, a tradeoff between resonance suppression performance and power losses should be done. The theoretical calculations of damping resistor is mentioned in Section 3.4 An optimal resistor value is selected in the experimental studies in order to satisfy sufficient resonance damping and to maintain low power losses. With the selected damping resistor value, SAPF with LCL filter prototype lessens the source current THD from 37.6% to 3.14%. Besides, the power dissipation of SAPF is almost 0.41 kW. Harmonic levels in load and source current and compensation performance of SAPF are given in Table 5.2.

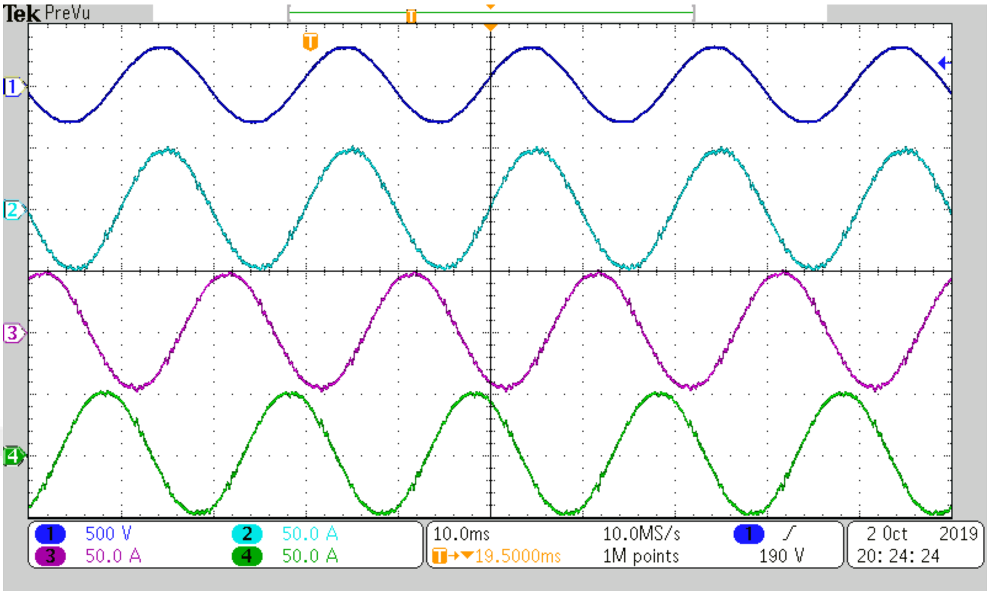

Figure 5.19. Source voltage and current waveforms during operation with LCL filter damped through series resistor

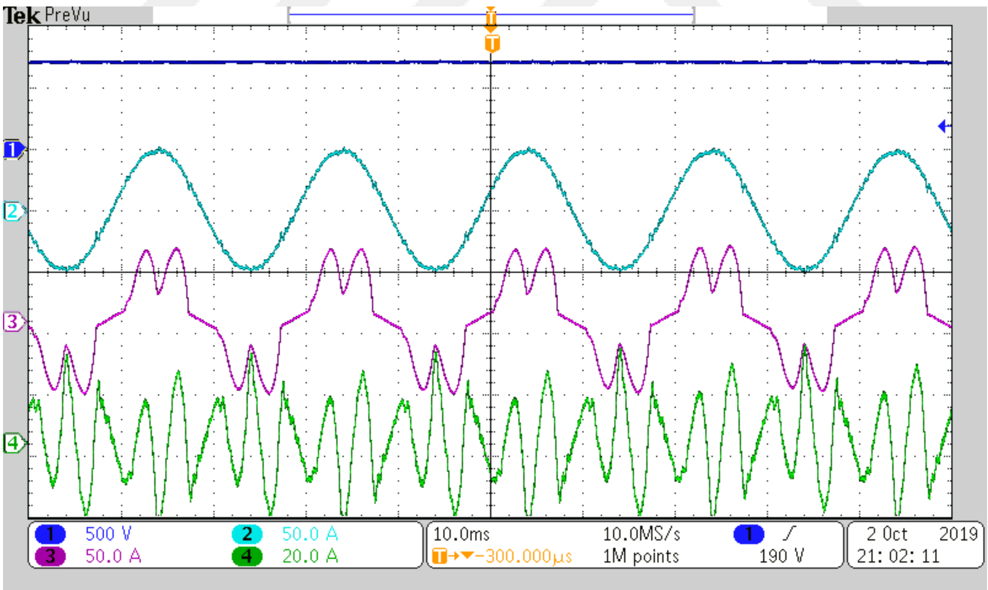

Figure 5.20. DC link voltage and current waveforms during operation with LCL filter damped through series resistor

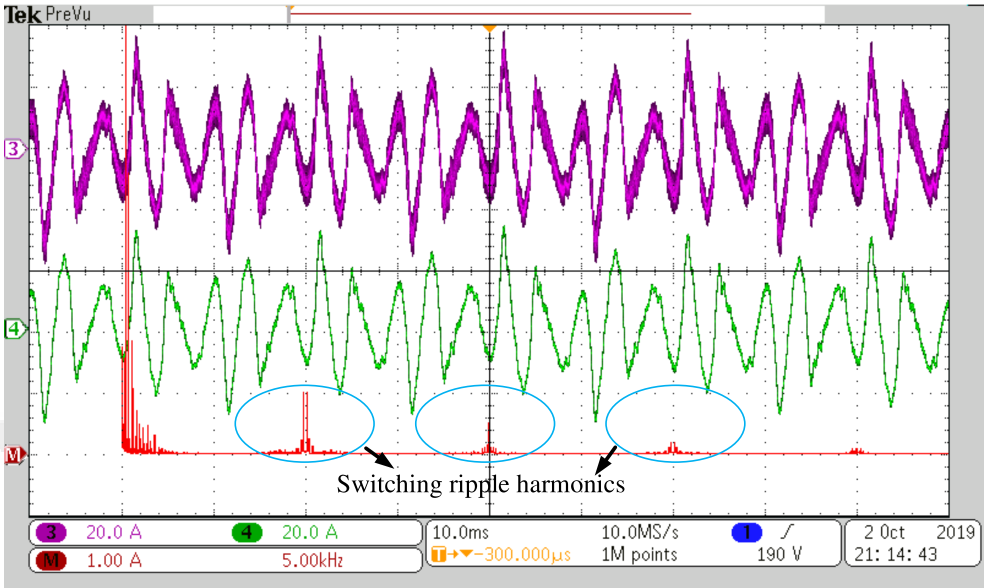

Figure 5.21. Grid-side and inverter-side current waveforms of SAPF with FFT spectrum of inverter-side current

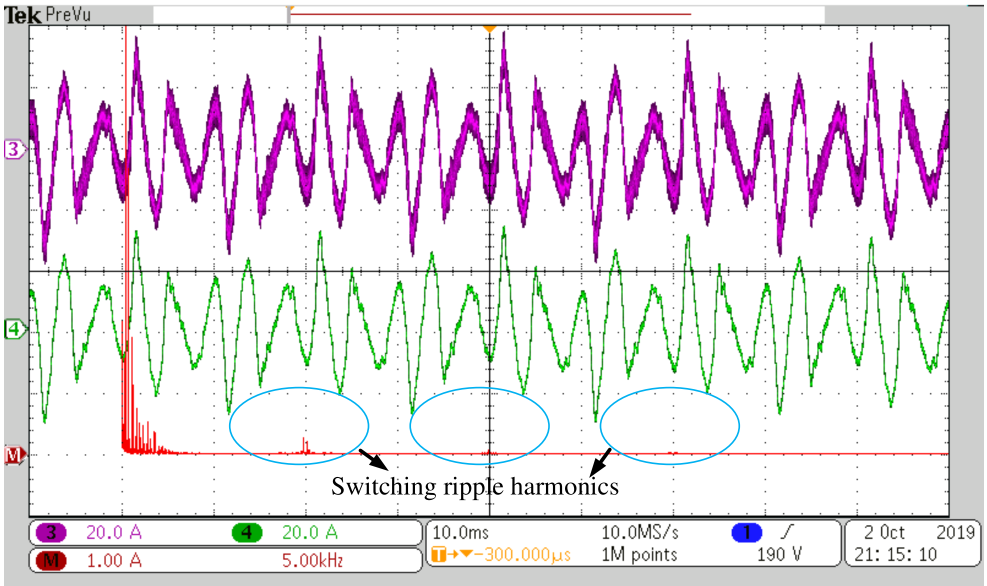

Figure 5.22. Grid-side and inverter-side SAPF current waveforms with FFT spectrum of grid-side current

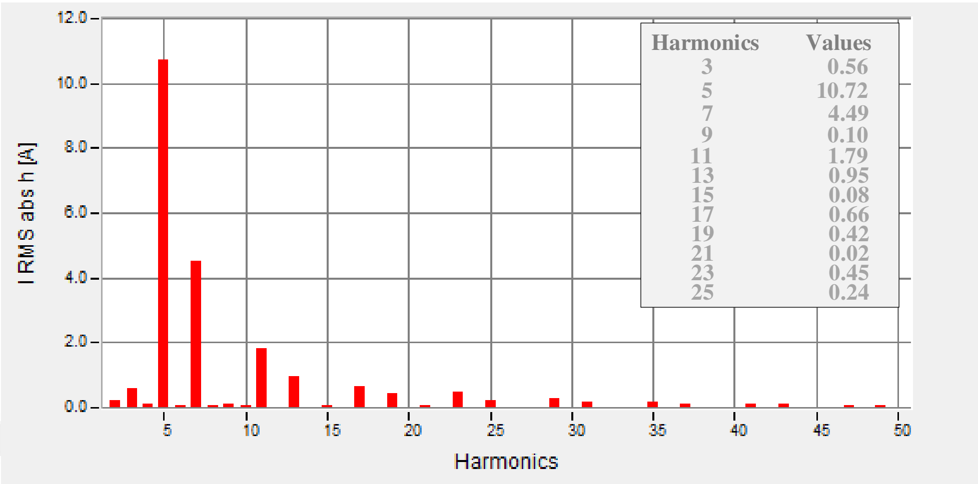

Figure 5.23. Load current harmonic spectrum during operation with LCL filter damped through series resistor

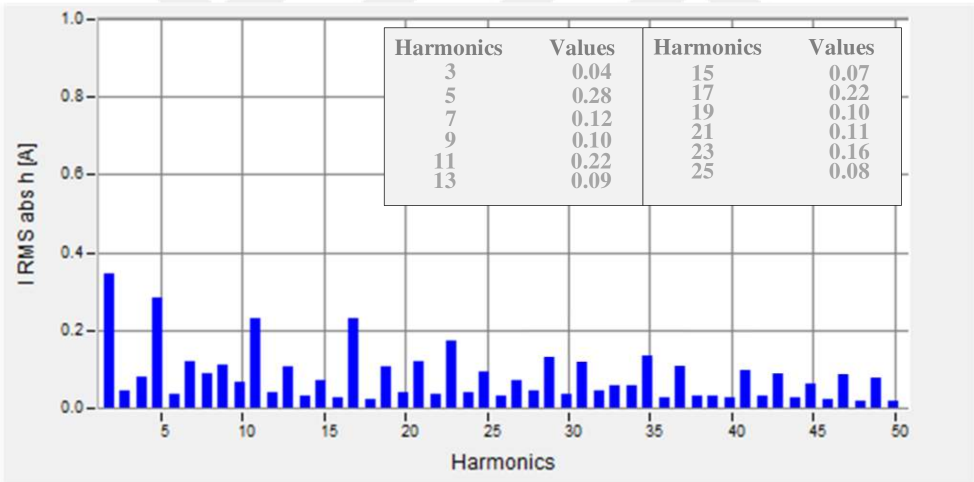

Figure 5.24. Source current harmonic spectrum during operation with LCL filter damped through series resistor

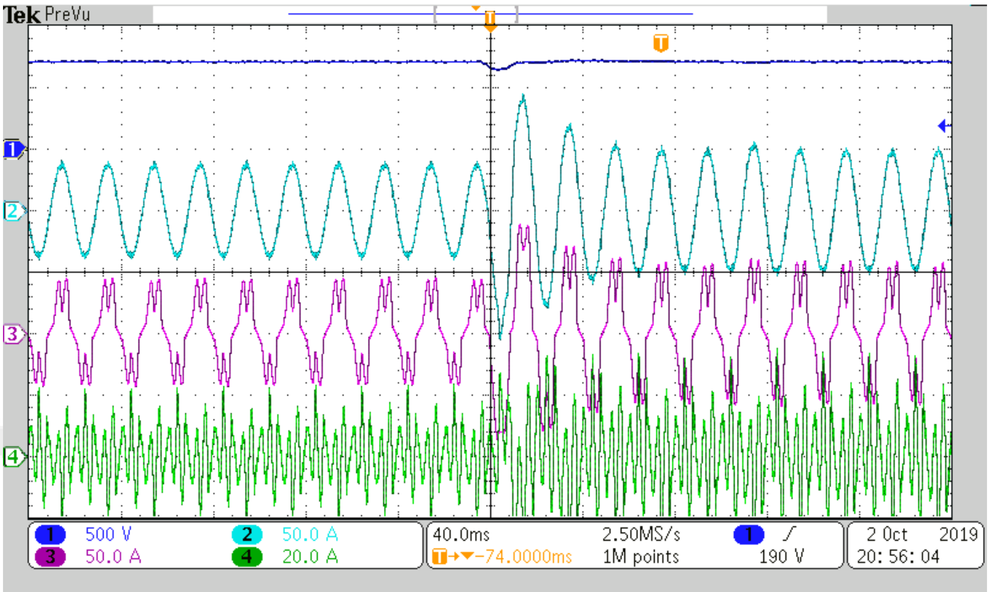

Figure 5.25. DC link voltage and current waveforms during dynamic operation with LCL filter damped through series resistor

Table 5.2. Harmonic levels in load and source current and compensation performance of SAPF with LCL filter damped with series resistor

Harm. Order	Load current	Source Current	Comp. Perform.
5	10.72	0.28	97.38%
7	4.49	0.12	97.32%
11	1.79	0.22	87.70%
13	0.95	0.09	90.52%
17	0.66	0.22	66.66%
19	0.42	0.10	76.19%
23	0.45	0.16	64.44%
25	0.24	0.08	66.66%

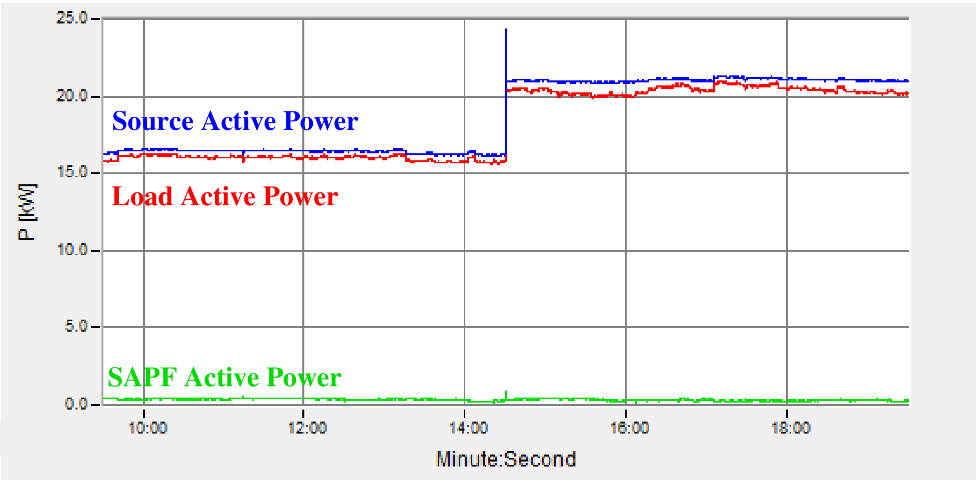

Figure 5.26. Active power trends of source, load and SAPF during operation with LCL filter damped through series resistor

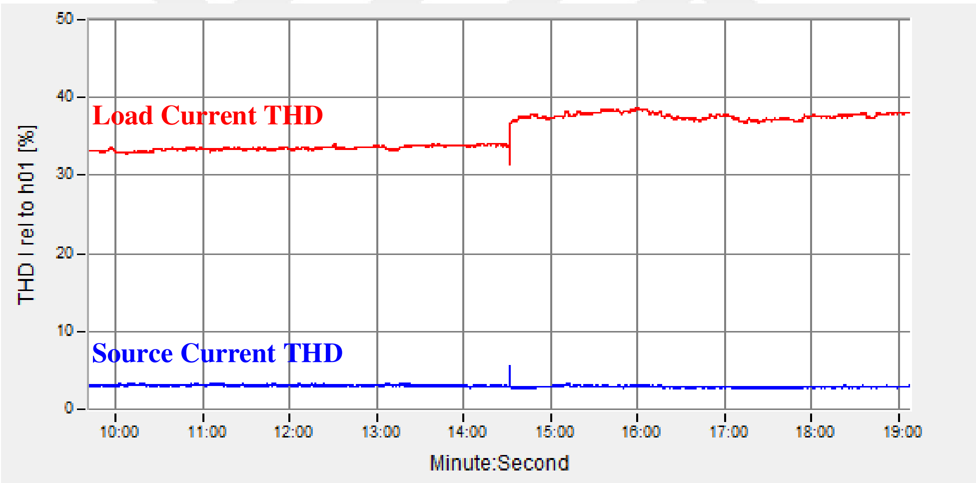

Figure 5.27. THD trends of source and load currents during dynamic operation

5.3.4. LCL Filter with Capacitor Current feedback Active Damping

In this case, the resonance damping performance of the capacitor current feedback method (Figure 3.17) presented in Section 3.4.2 is investigated. The source voltage and current waveforms are demonstrated in Figure 5.28. The waveforms of DC link voltage and source, load and SAPF currents are shown in Figure 5.29. The inverter-side and grid-side currents with their FFTs are given in Figures 5.30 and 5.31, respectively. The harmonic spectrums of load and source currents are demonstrated in Figures 5.32 and 5.33, respectively. Additionally, the waveforms of DC link voltage, source, load and SAPF currents are presented in Figure 5.34 while enabling and disabling of the capacitor current feedback active damping. The dynamic response of SAPF with LCL filter damped by capacitor current feedback method is shown in Figure 5.35. The active power trends of source, load and SAPF with capacitor current feedback damped LCL filter is shown in Figure 5.36. Besides, the THD trend of load and source currents are given in Figure 5.37.

It is shown from the experimental results that the capacitor current feedback satisfies sufficient resonance damping. The resonance harmonic currents are suppressed with 87%. Moreover, the switching ripple harmonics around 10 kHz and 20 kHz sidebands are diminished to 0.17 A and 0.01 A. The switching ripple harmonics are, filtered by 84%, same as undamped LCL filter case. On the other hand, the compensation performance of SAPF prototype is adversely affected at upper harmonic components than 30^{th} order due to feedback of the capacitor current. The harmonic currents upper than 30^{th} order are increased compared with single L filter and passively damped LCL filter systems.

As mention above, the resonance currents are dropped by 87% with the capacitor current feedback AD. The resonance currents can be further decreased by tuning higher capacitor current feedback gain. However, at the certain value of the feedback gain, it has negative impact on the main controller of SAPF system, which leads to a contradiction between resonance damping and compensation performance of SAPF system. With the selected feedback gain, SAPF with LCL prototype ensures sufficient resonance damping and minimum THD value of the source current despite of amplified high order harmonics. SAPF with LCL filter damped by capacitor current feedback AD drops the source current THD value from 37.5% to 3.38%. Harmonic levels in load and source current and compensation performance of SAPF are demonstrated in Table 5.3. Besides, the power dissipation of SAPF is almost 0.22

kW that decreased by half in comparison of series resistor PD case.

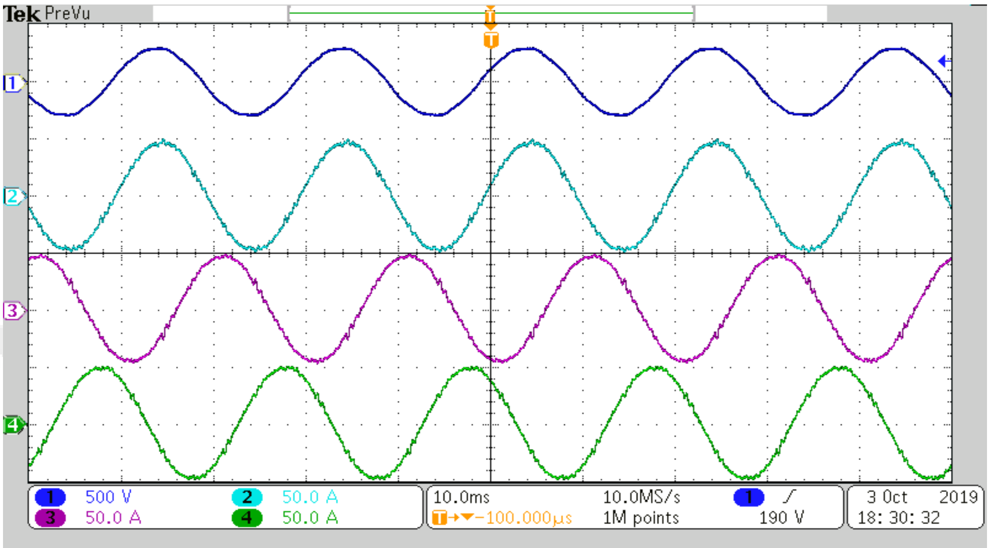

Figure 5.28. Source voltage and current waveforms during operation with LCL filter damped through capacitor current feedback

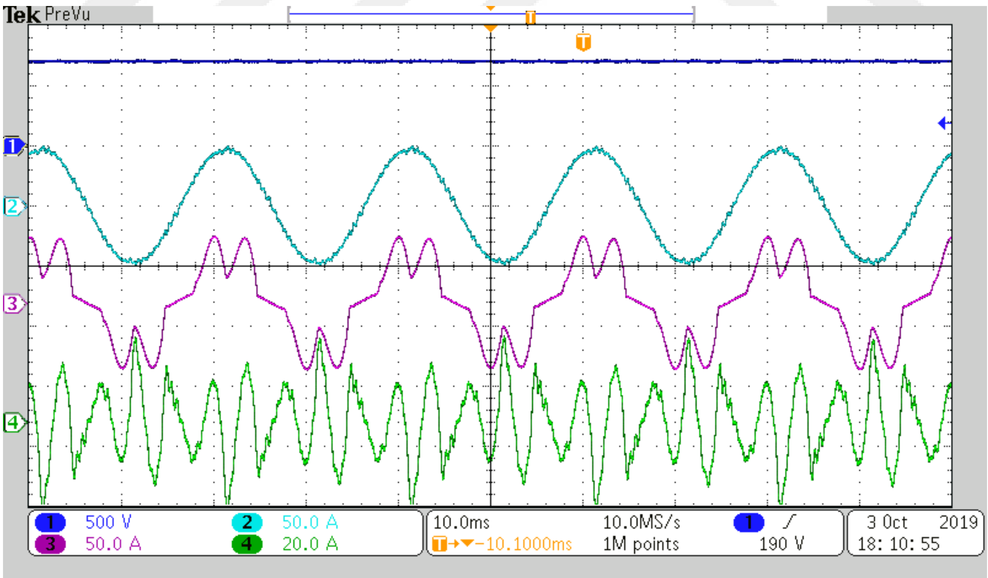

Figure 5.29. DC link voltage and current waveforms during operation with LCL filter damped through capacitor current feedback

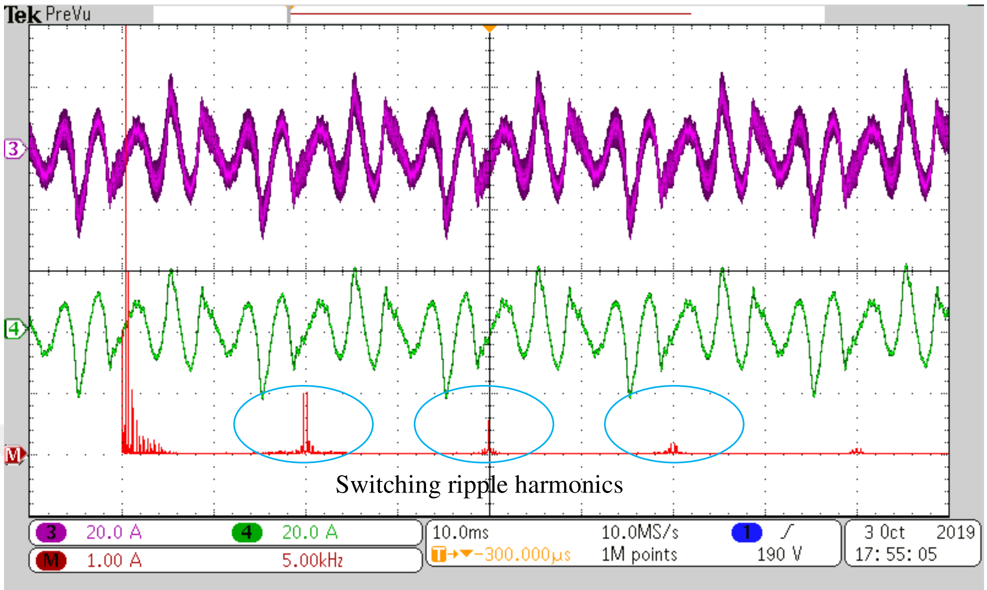

Figure 5.30. Grid-side and inverter-side current waveforms of SAPF with FFT spectrum of inverter-side current

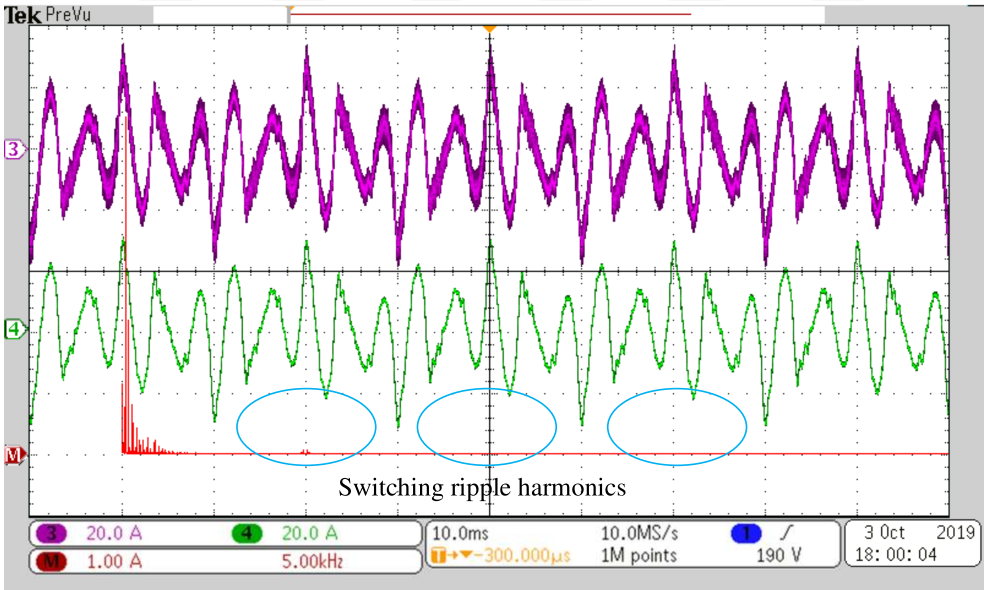

Figure 5.31. Grid-side and inverter-side current waveforms of SAPF with FFT spectrum of grid-side current

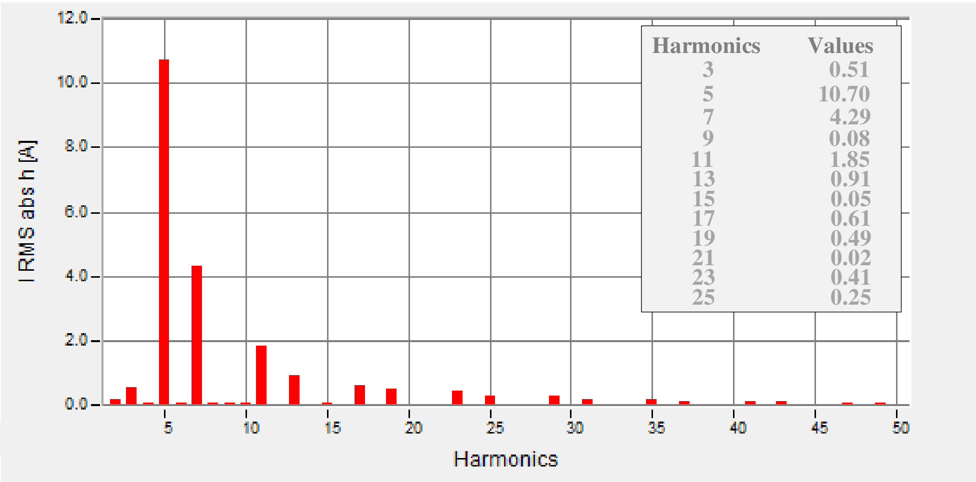

Figure 5.32. Load current harmonic spectrum during operation with LCL filter damped through capacitor current feedback

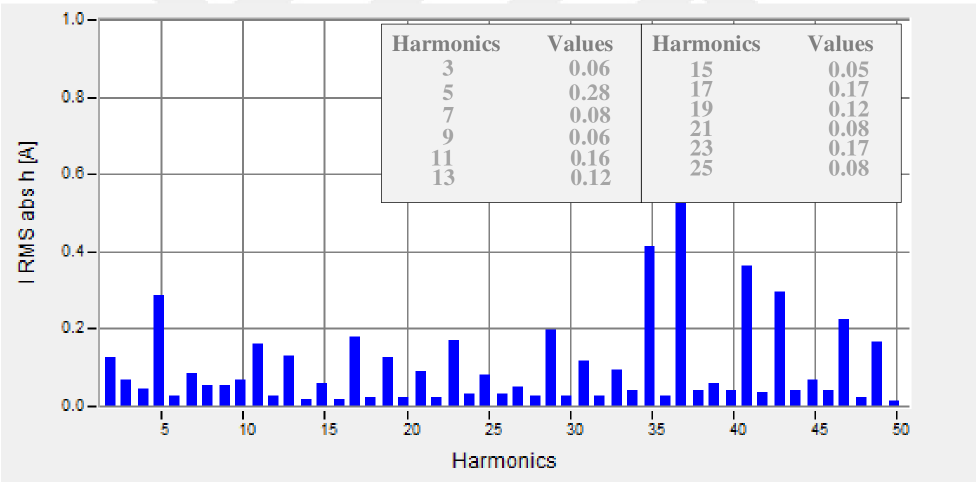

Figure 5.33. Source current harmonic spectrum during operation with LCL filter damped through capacitor current feedback

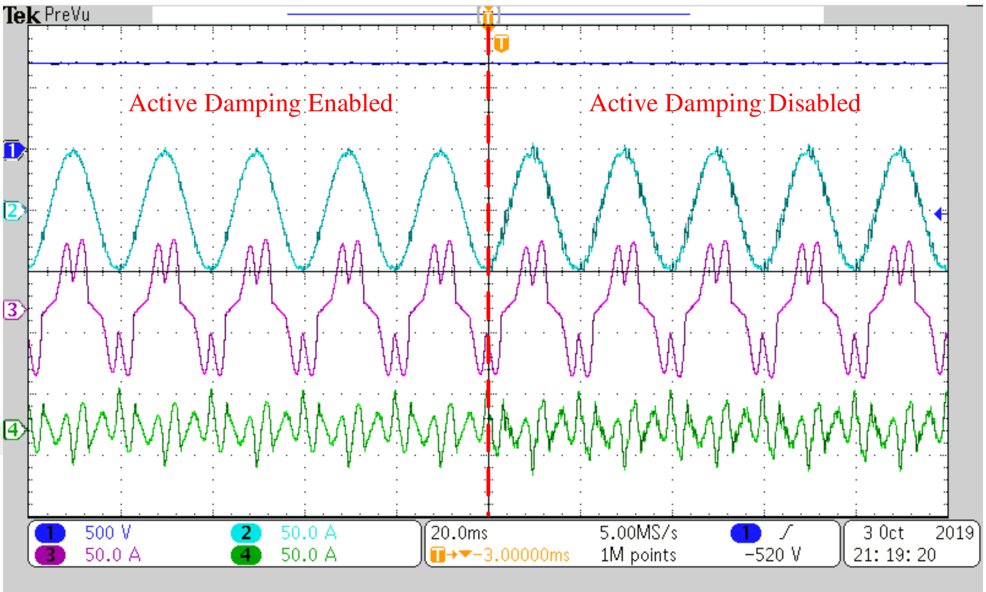

Figure 5.34. DC link voltage and current waveforms during enabling and disabling capacitor current feedback active damping

Table 5.3. Harmonic levels in load and source current and compensation performance of SAPF with LCL filter damped with capacitor current feedback

Harm. Order	Load current	Source Current	Comp. Perform.
5	10.70	0.28	97.38%
7	4.29	0.08	98.13%
11	1.85	0.16	91.38%
13	0.91	0.12	86.81%
17	0.61	0.17	72.13%
19	0.49	0.12	75.51%
23	0.41	0.17	58.53%
25	0.25	0.08	68.00%

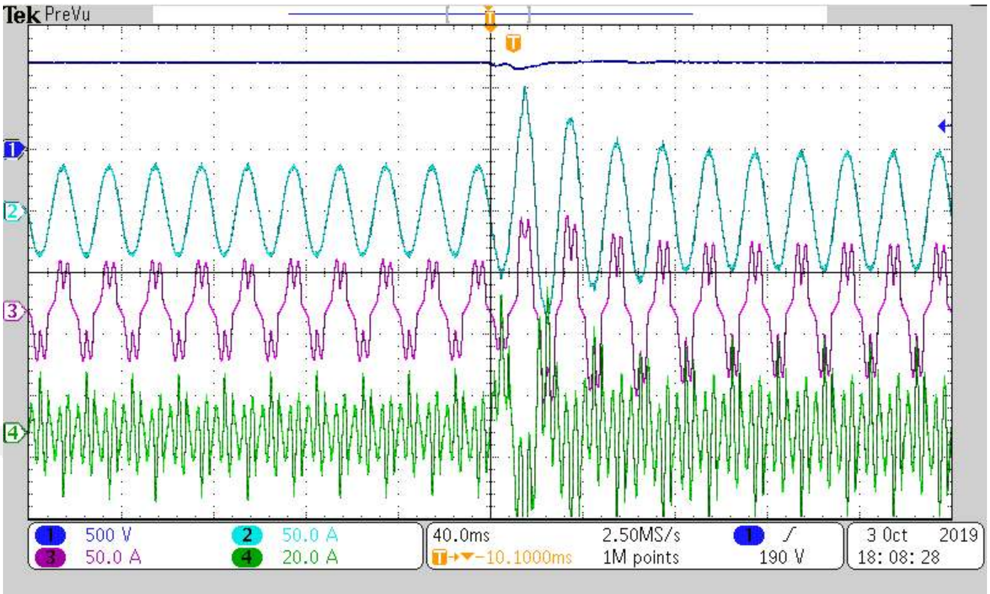

Figure 5.35. DC link voltage and current waveforms during dynamic operation with LCL filter damped through capacitor current feedback

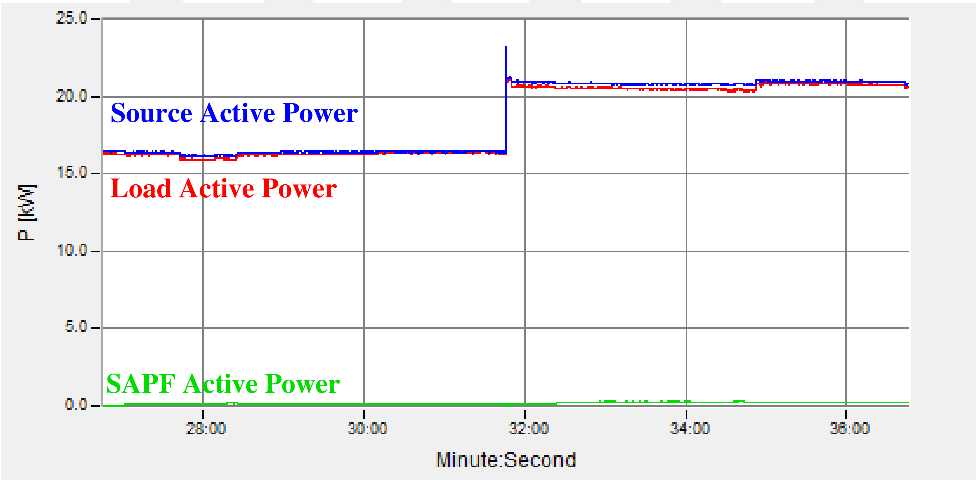

Figure 5.36. Active power trends of source, load and SAPF during operation with LCL filter damped through capacitor current feedback

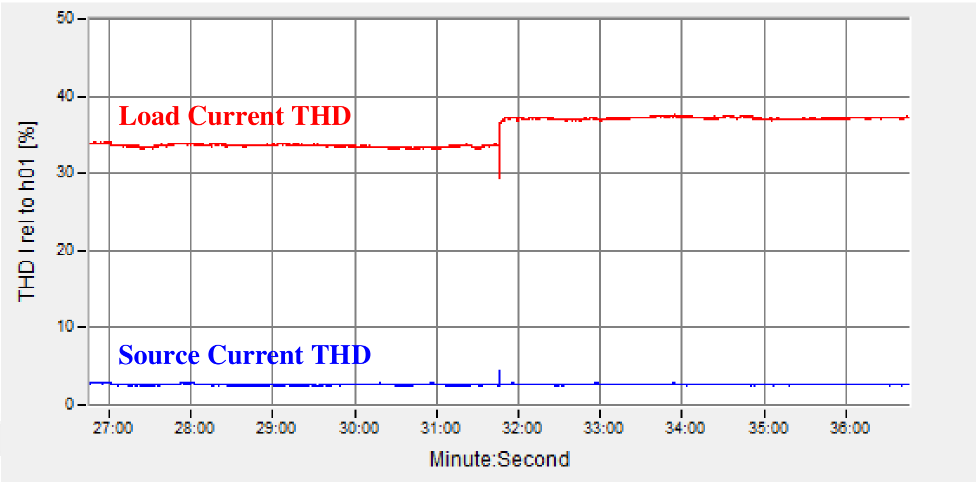

Figure 5.37. THD trends of source and load currents during dynamic operation

5.3.5. LCL Filter with the Proposed Converter based Active Damper

Owing to the damping power losses of PD method and adverse effect of capacitor current feedback AD on compensation currents upper than 30^{th} order, a distinct resonance damping method based on converter is proposed in literature, named CBAD in this thesis. By this means, the power losses because of damping resonance and reduced compensation performance of high harmonic currents are aimed to be alleviated. In this case, the resonance damping performance and power losses of CBAD method (Figure 3.22) presented in Section 3.4.3 is examined and evaluated.

The source voltage and current waveforms are demonstrated in Figure 5.38. The waveforms of DC link voltage and source, load and SAPF currents are shown in Figure 5.39. Besides, the grid-side, inverter-side and capacitor currents of LCL filter and CBAD dc link voltage waveforms are shown in Figure 5.40. The inverter-side, grid-side and capacitor currents of LCL filter with their FFTs are given in Figures 5.41, 5.42 and 5.43, respectively. The harmonic spectrums of load and source currents are demonstrated in Figure 5.44 and 5.45, respectively. In addition, the waveforms of CBAD dc link voltage, source current, grid-side SAPF current and capacitor current are presented in Figure 5.46 while enabling and disabling of CBAD damping controller. The dynamic response of SAPF with LCL filter damped by CBAD is shown in Figure 5.47. The active power trends of source, load and SAPF with LCL filter damped through CBAD is shown in Figure 5.48. Besides, the THD trend of load and source currents are given in Figure 5.49.

It is shown from the experimental results of SAPF with LCL filter damped with CBAD that sufficient resonance damping is ensured by auxiliary converter. The resonance suppression is performed by 68%, which is almost same with capacitor current feedback method. Furthermore, the switching ripple harmonics around 10 kHz and 20 kHz sidebands are decreased to 0.15A and 0.06A, where filtering performance achieved by 83%. In contrast, compensation performance of high order harmonic components is not endangered from CBAD as capacitor current AD method. SAPF with LCL filter damped CBAD decreases the source current THD value from 41.2% to 3.43%. Harmonic levels in load and source current and compensation performance of SAPF are given in Table 5.4. Additionally, the damping power losses drop almost 0.1kW compared with simple resistor PD method.

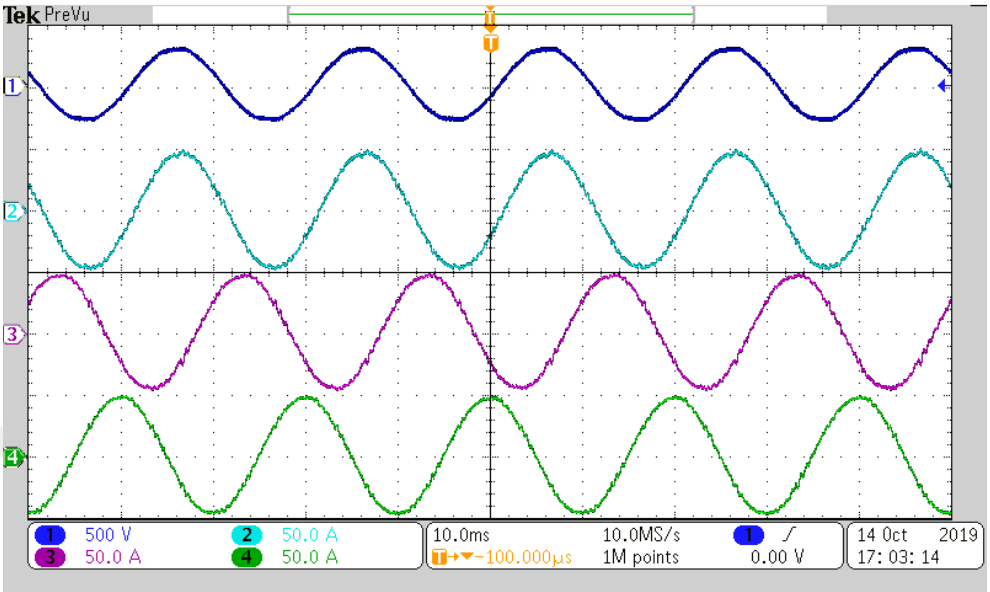

Figure 5.38. Source voltage and current waveforms during operation with LCL filter damped through CBAD

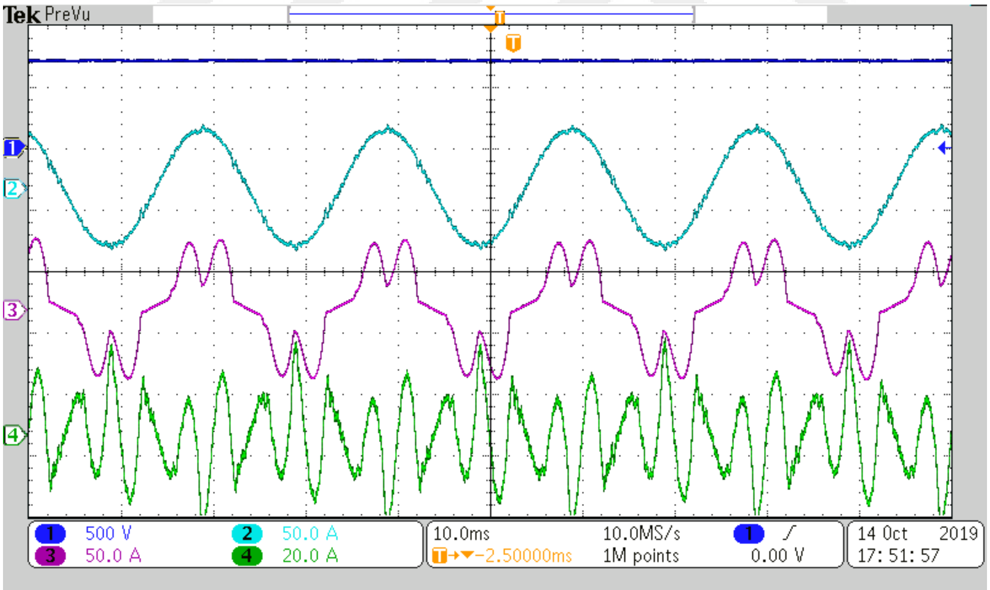

Figure 5.39. DC link voltage and current waveforms during operation with LCL filter damped through CBAD

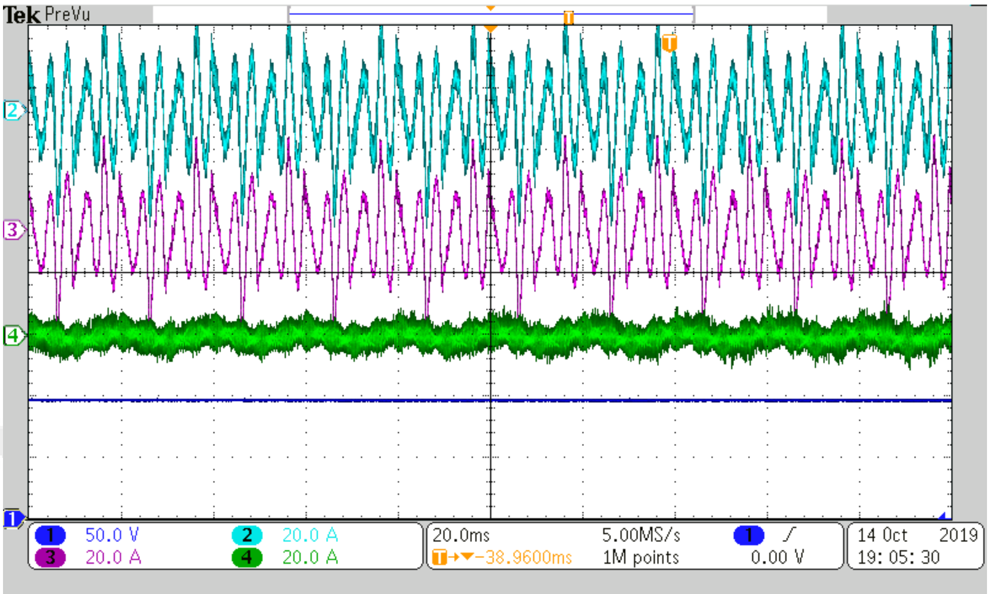

Figure 5.40. Grid-side, inverter-side and capacitor currents and CBAD dc link voltage waveforms during operation with LCL filter damped through CBAD

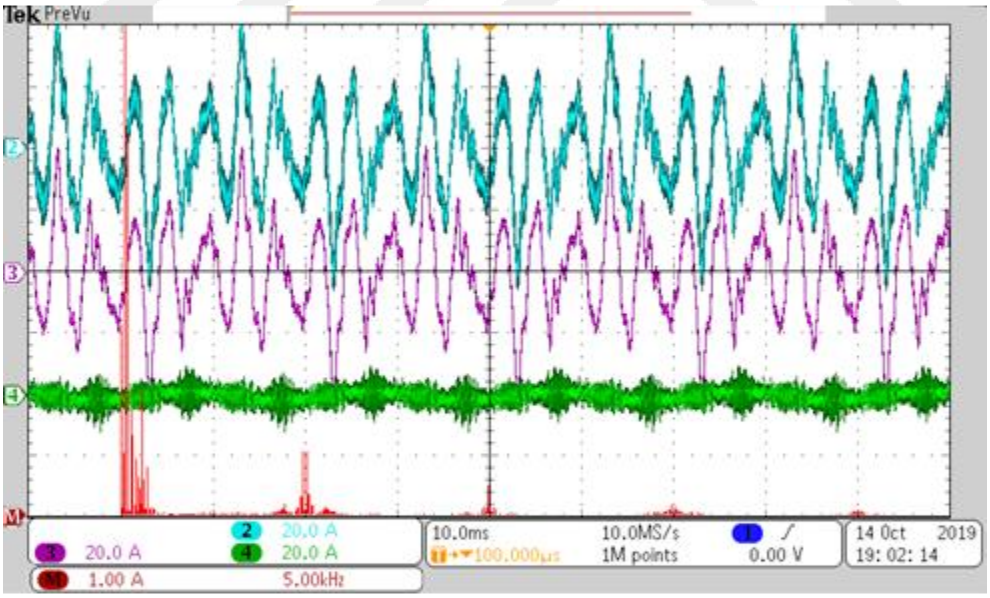

Figure 5.41. Grid-side, inverter-side and capacitor current waveforms of SAPF with FFT spectrum of inverter-side current

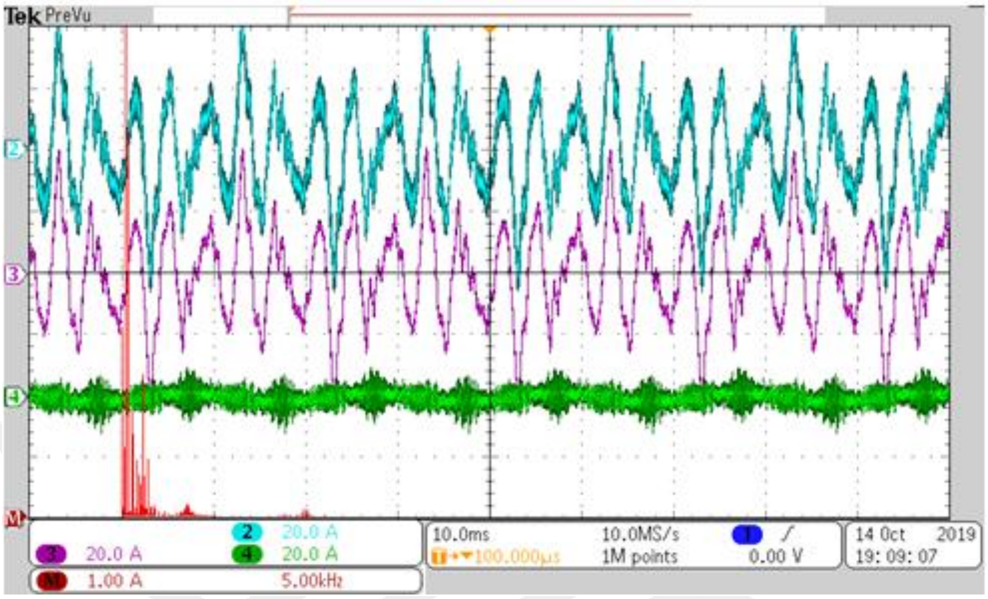

Figure 5.42. Grid-side, inverter-side and capacitor current waveforms of SAPF with FFT spectrum of grid-side current

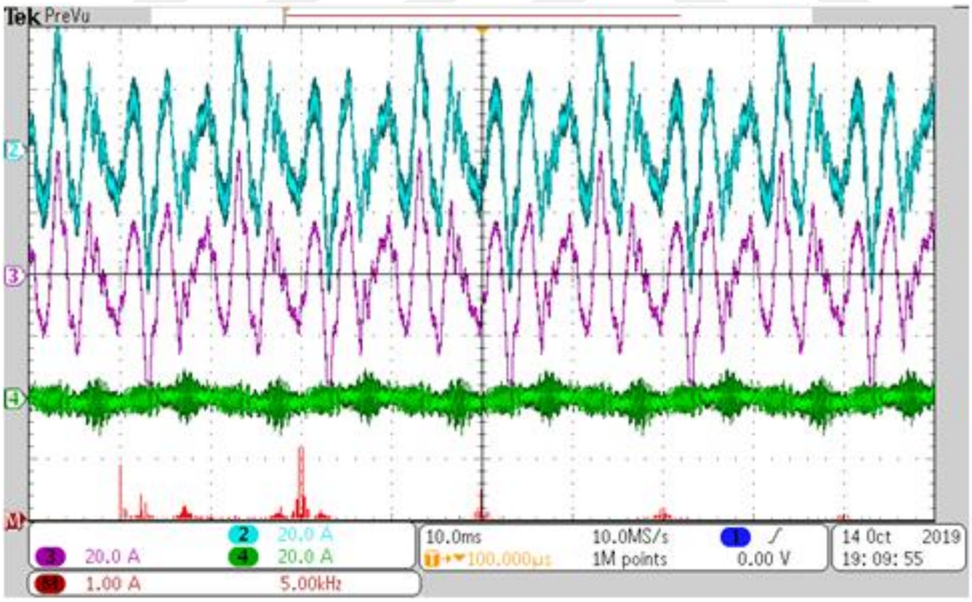

Figure 5.43. Grid-side, inverter-side and capacitor current waveforms of SAPF with FFT spectrum of capacitor current

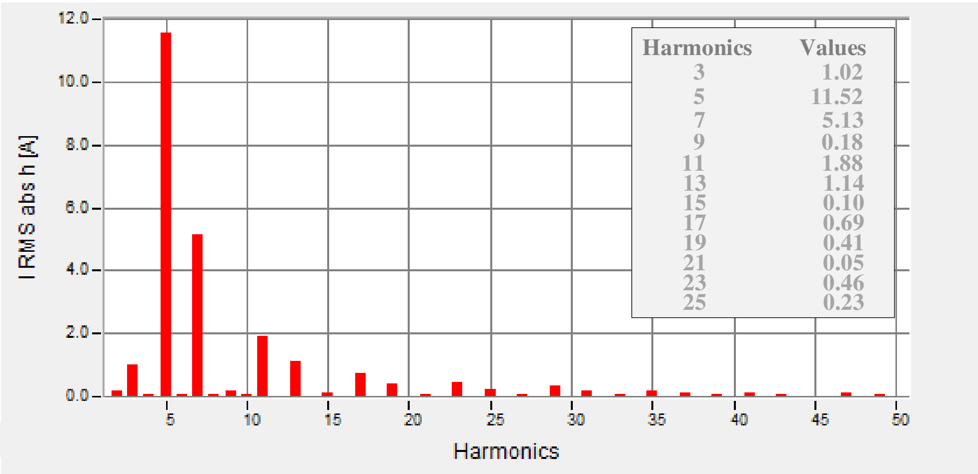

Figure 5.44. Load current harmonic spectrum during operation with LCL filter damped through CBAD

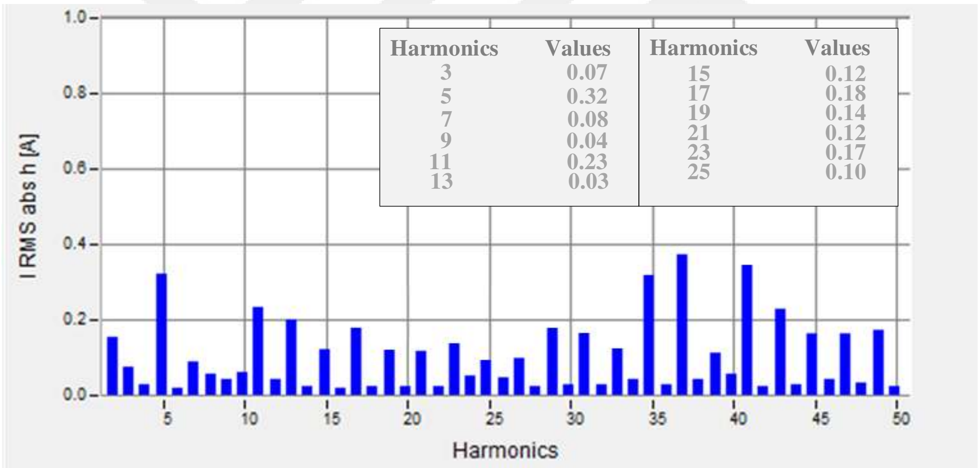

Figure 5.45. Source current harmonic spectrum during operation with LCL filter damped through CBAD

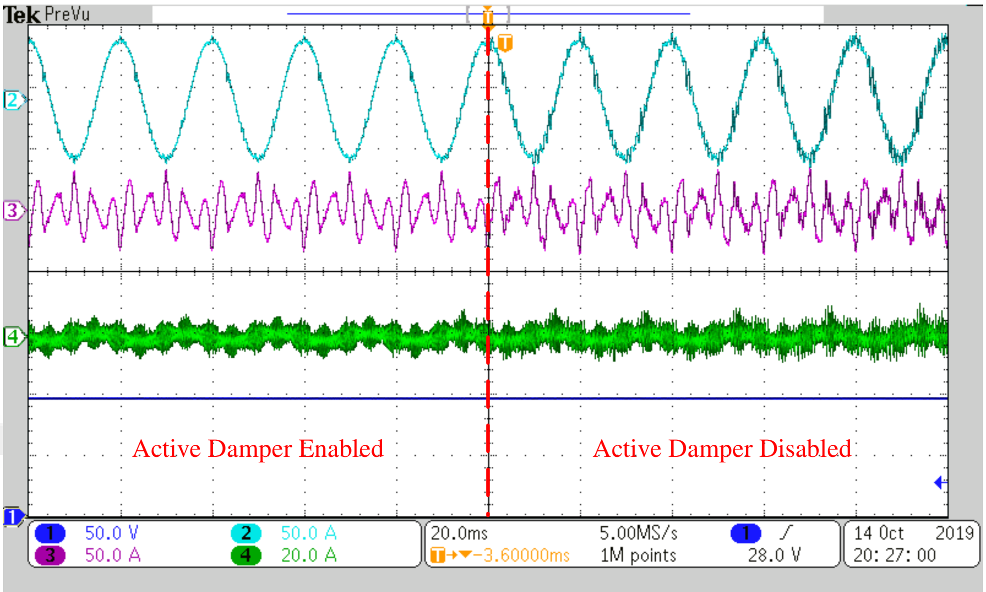

Figure 5.46. Source current, SAPF grid-side current, capacitor current and CBAD dc link voltage waveforms during enabling and disabling damping function of CBAD

Table 5.4. Harmonic levels in load and source current and compensation performance of SAPF with LCL filter damped with CBAD

Harm. Order	Load current	Source Current	Comp. Perform.
5	11.52	0.32	97.22%
7	5.13	0.08	98.44%
11	1.88	0.23	87.76%
13	1.14	0.03	97.36%
17	0.69	0.18	73.91%
19	0.41	0.14	65.85%
23	0.46	0.17	63.04%
25	0.23	0.10	56.52%

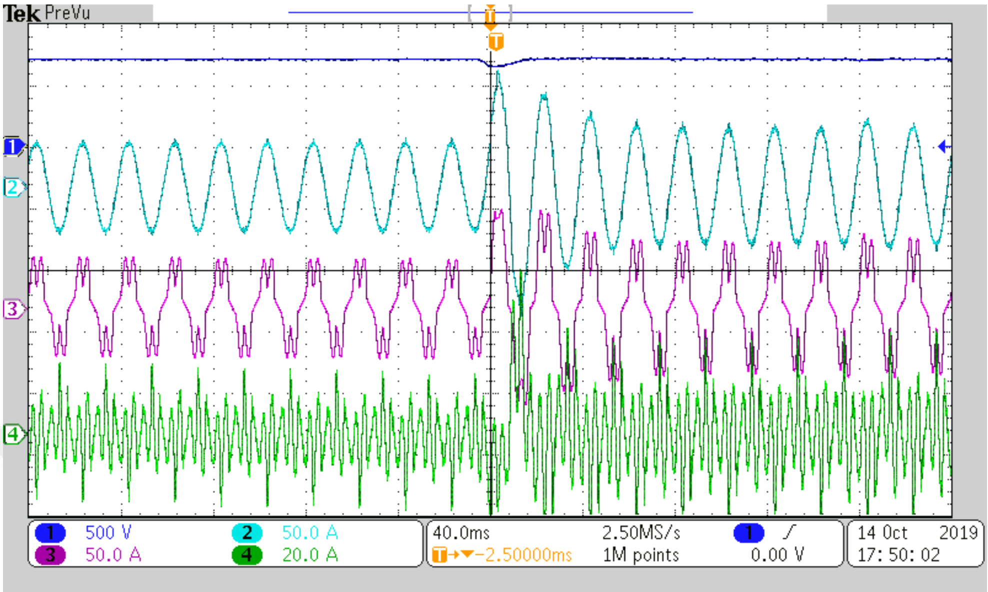

Figure 5.47. DC link voltage and current waveforms during dynamic operation with LCL filter damped through CBAD

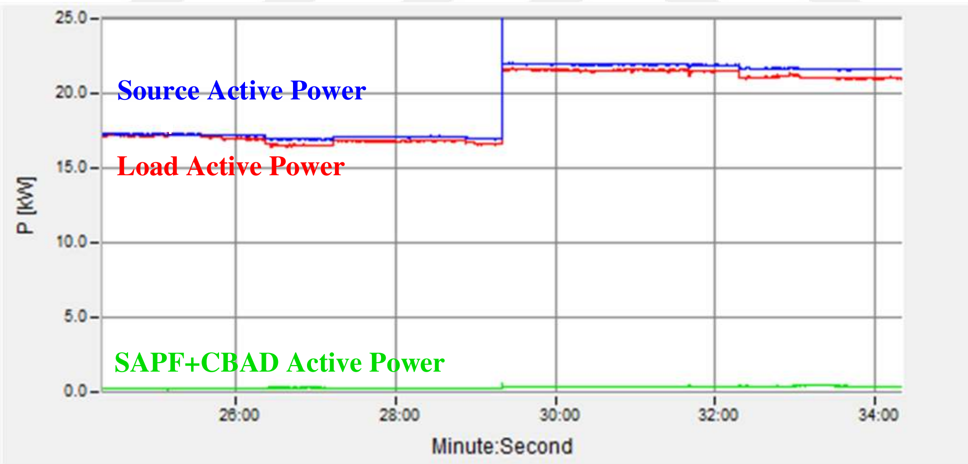

Figure 5.48. Active power trends of source, load and SAPF+CBAD during operation with LCL filter damped through CBAD

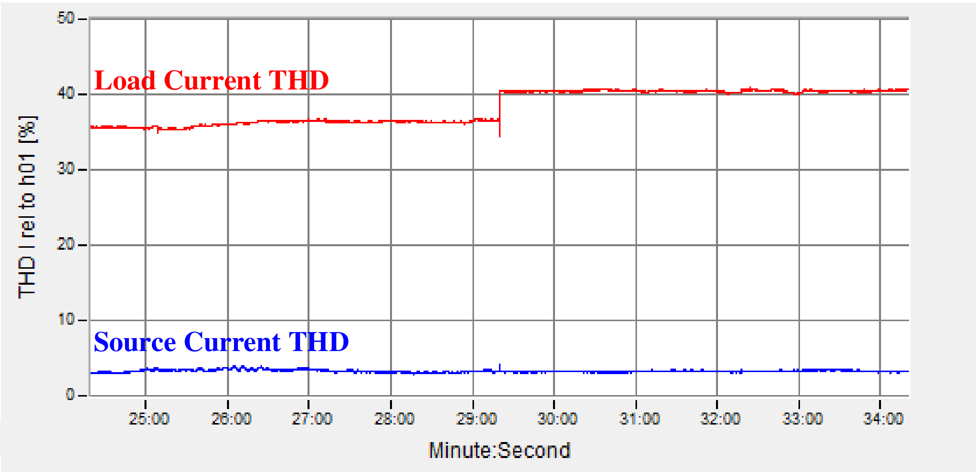

Figure 5.49. THD trends of source and load currents during dynamic operation

5.4. Discussion and Performance Evaluation of Investigated Damping Methods

In this section, the performance of SAPF with LCL filter is discussed and evaluated under three applied damping methods. The applied damping methods are simple resistor PD, capacitor current feedback AD and CBAD. These damping methods are based on passive component, modification of SAPF controller and adding an auxiliary converter, respectively. The performance of damping methods are compared with respect to resonance suppression, damping power losses, switching harmonics attenuation and impact on harmonic compensation performance of SAPF.

The first concern to compare the damping methods is their capability of resonance damping. To perform effective comparison, optimal resistor value, feedback coefficient and notch filter parameters are designed and chosen for PD, AD and CBAD, respectively. The damping performances are examined through Bode graphs presented in Section 3. According to the graphs, the resonance peak of undamped LCL filter is obtained near 270 dB at 3.45 kHz, the reason of system instability. After applying simple resistor PD with 1.5Ω value, the magnitude at the resonance frequency is observed as -13.3dB, ensuring sufficient resonance suppression. By applying capacitor current feedback with 7.3 constant gain, the amplitude at the resonance frequency is monitored as -11.8dB, providing adequate resonance damping and stable system. However, increasing the feedback constant value to 8.3, in order to get same resonance suppression as PD method, leads an unstable system. In CBAD resonance damping method, a virtual resistor characteristic is provided at the resonance frequency. A notch filter is used to obtain the resonance current from the capacitor current. The parameters of the notch filter is tuned so that it will suppress the resonance same ratio with PD method. Thus, the magnitude at the resonance frequency is acquired as -13.3dB. The damping ratio can be theoretically further increased by increasing the injected resonance current value with increasing the notch depth and reducing the notch filter band. However, further increase of the notch filter depth has adverse impact on CBAD controller.

Another parameter for performance comparison is power losses caused because of damping. The power losses are observed by Fluke 1760 PQ analyzer and compared according to measuring PCC voltages and SAPF currents. As mentioned previously, AD methods do not cause additional losses in the system. But, in order to obtain actual damping power losses of the other two methods, the system power losses of SAPF with LCL filter during operation are obtained by applying capacitor current feedback AD method. The measured power losses of the system is acquired as 220W at full load operation. These power losses are released owing to the switching of the main VSI, supply of the control card and cooling fan of heatsink. On the other side, the power losses are observed as 410W at full load operation condition. This means that suppressing the resonance by adding a 1.5Ω series resistor with the filter capacitor results in additional 190W power losses in the system. The power losses generated because of the damping resistor equal to 1.9% of the SAPF power rating. The power losses are measured as 310W under full load operation once suppressing the resonance by adding an auxiliary converter, meaning that extra 90W power losses are drawn from the electric grid. The additional power losses caused due to CBAD is equivalent to 0.9% of rated SAPF power. Performing resonance damping by CBAD instead of simple resistor PD leads a reduction of the power losses by 1%.

Another factor to determine the performance of the damping method is the attenuation of the switching ripple harmonics. In order to evaluate their mitigation ratio of the switching frequency harmonics, the experimental results of SAPF with single L filter are referred as comparison indicator. Thus, the total inductances of single L filter and LCL filter are hold same. According to theoretical studies and Bode diagrams of open loop transfer functions given in Section 3, the attenuation ratios at the switching frequency and the twice switching frequency are obtained 40dB and 65dB for simple resistor PD. These ratios are 55dB and 75dB when using capacitor current feedback AD method. Additionally, the attenuation ratios are acquired as 215dB and 70dB with applying CBAD. In higher frequencies than the twice switching frequency, the mitigation superiorities come respectively as capacitor current feedback AD, simple resistor PD and CBAD. In experimental studies, the current amplitudes at the switching frequency and the twice switching frequency are obtained as 1A and 0.6A for SAPF with single L filter. The current values are 0.21A at the switching frequency and 0.07A at the twice switching frequency for passively damped SAPF with LCL filter. For the capacitor current feedback damped SAPF with LCL filter, the switching harmonic amplitudes are 0.17A and 0.01A, respectively. With applying CBAD to suppress the resonance of SAPF with LCL filter, the switching currents are measured as 0.15A and 0.06A, respectively. The experimental results show that the switching ripple harmonics are well attenuated through application of LCL filter with various damping techniques. The switching ripple currents at switching frequency are minimum when the CBAD method is used. This performance is obtained because the series inductance with the filter capacitor show lowest impedance at the switching frequency. However, the harmonics at the twice switching frequency are lower with the capacitor current feedback AD method. On the other side, despite sufficient attenuation with simple resistor PD method, the switching harmonics are highest among the damping methods.

The last comparison quantity is that the influence of damping method on compensation performance of SAPF. The controller bandwidth of SAPF is selected to be at 1.5 kHz in experimental studies. According to this, the gain margins are obtained by applying optimal parameters for the damping methods. The gain margins are observed as 11.5dB at 2.88kHz, 10.8dB at 2.45kHz and 11.2dB at 2.7kHz for PD, AD and CBAD methods, respectively. The source current THDs are obtained up to 50^{th} harmonic components as 3.14%, 3.38% and 3.43%, respectively. During experimental studies of CBAD case, the third harmonics are high in load current due to voltage unbalance occurred in the electrical grid. Thus, the third harmonic components, especially 15^{th} order, are high and increase the source THD of CBAD case.

To summarize the experimental results, a comparison table is presented in Table 5.5.

Table 5.5. Comparison summary of experimental results.

Method/Comp. Parameter	**PD**	**AD**	**CBAD**
Resonance Suppression (%)	82%	87%	68%
Switching Components Mitigation (%)	73%	84%	83%
Power Losses (W)	190 (1.9%)	-	90 (0.9%)
Source-Load THDs (%)	3.14% - 37.6%	3.38% - 37.5%	3.43% - 41.2%

6. CONCLUSION AND FUTURE

6.1. Concluding Remarks

In recent years, the increasing nonlinear characteristic change in load profiles brings about harmonics PQ problem, distorting the electric grid system. The distortion limits of harmonic currents are determined by IEEE Std. 519-1992 and IEC-61000-3-4 standards. The current harmonics should be kept under the determined limits. The harmonics compensation issues a challenge to today's complicated electric distribution system. PFs were the earliest solution among harmonic compensation systems. However, because of inadequate compensation performance of PFs, APFs attract more interest with dynamic harmonic compensation capability. APFs are formed by VSIs, performing compensation via controlling switching components. Nevertheless, the high order switching harmonics are generated during operation of VSI. With this respect, another harmonic phenomena is exposed in the system. To solve the switching ripple harmonics, a single L filter was commonly used with SAPF filtering ripple currents. However, a large inductance is necessitated to sufficiently reduce the ripple harmonics, which also leads higher voltage drop. To overcome this phenomena, LCL filter has recently wide penetration to SAPF. LCL filter has more effective ripple harmonics alleviation with lower inductance value. Despite excellent benefits, a third order LCL filter has a resonance issue dragging the system unstable. The resonance damping methods are investigated by many researchers for grid-connected VSIs. However, the damping methods need a detailed examination for SAPF with LCL filter because of wide operation bandwidth.

In this thesis, a 10kVA experimental prototype of SAPF with LCL filter is implemented in order to perform harmonic compensation and apply various resonance damping methods. In addition, an auxiliary converter based damping method is proposed and applied for the first in SAPF with LCL filter. The comprehensive designs of power circuits of SAPF with LCL filter and CBAD are presented in this thesis studies. The design of VSIs and LCL filter are fulfilled according to the theoretical calculations and simulation environment studies done in MATLAB/Simulink. In the scope of this thesis, electronic cards are designed and developed for SAPF and CBAD systems. The detailed design guides are performed including the selection of microcontroller, electronic circuits and PCB card. The prototype systems are implemented through power circuits, electronic control system with developed embedded software algorithms.

The performances of SAPF with LCL filter applying different damping methods are examined through experimental studies carried out in Power Electronics Research Laboratory of Çukurova University Electric and Electronics Engineering Department. A nonlinear load group including three pieces with 5kW each is set to investigate dynamic and steady state performances of the implemented prototypes.

In the aspect of the experimental studies, SAPF is firstly tested with single L filter in order to demonstrate the effectiveness of LCL filter. After that, SAPF with undamped LCL filter is investigated to show the resonance issue. Then, simple resistor PD, capacitor current AD and CBAD methods are examined and compared in terms of resonance damping, switching ripple attenuation, power losses and harmonic compensation performances. The experimental results show that each damping method has its own superiority over the other methods. Thus, a trade of damping method decision should be made according to previously determined comparison parameters by including cost of method. As a result of experimental studies, it is useful to choose simple resistor PD method once the system complexity, resonance suppression and the implementation cost are taken into consideration. The resonance is damped by resistor without affecting the system stability. Besides, simple resistor are used series with the filter capacitor, not causing extreme cost increase to overall system cost. On the other side, it is not rational to use PD method when attenuation of switching harmonics and power losses are considered. In the context of switching harmonics mitigation and power losses, it is sensible to apply the capacitor current feedback AD method. The utilization of AD does not cause additional power losses in the system, which keeps the system efficiency higher than other methods. However, this method may jeopardize the system stability owing to additional feedback in the controller algorithm. Furthermore, extra current measurement points are required to fulfil the resonance damping in this method. In this case, not only the system cost increases but also the size of the control card also scales up. Considering the stability range of the system and power losses simultaneously, it is reasonable to decide damping resonance through an auxiliary converter. In contrast to PD method, this method has lower damping power losses reducing by 1% of SAPF power rating. Moreover, this method provides better stability characteristic in comparison with AD method because of not making change in the controller algorithm. However, the implementation cost is quite high according to previous two methods. In addition, it occupies further space in implementation area.

6.2. Future Work

The application of LCL filter with SAPF is not having long duration. Thus, it needs further researches and enhancement, especially resonance damping methods. Some of methods are investigated and proposed in this thesis studies. The following contents will be performed as future research works.

- Investigation of different connection points of CBAD
- Examination of switching ripples produced by CBAD
- Support to high order harmonic compensation by CBAD
- Effect of LCL filter over high order harmonics compensation
- Apply various active damping methods by investigation stability regions
- Different digital filter to extract resonance currents for CBAD

REFERENCES

Aghdam, M. G. H. And Gharehpetian, G. B. (2005). Modeling of switching and conduction losses in three-phase SPWM VSC using switching function concept. 2005 IEEE Russia Power Tech.

Akagi, H., (1996). "New trends in active filters for power conditioning." IEEE Transactions on Industry Applications 32(6): 1312-1322.

Akagi, H., (2005). "Active Harmonic Filters." Proceedings of the IEEE 93(12): 2128-2141.

Akagi, H. (2005). The state-of-the-art of active filters for power conditioning. European Conference on Power Electronics and Applications, 2005

Allocco, J. M., (1997). "Laminated bus bars for power system interconnects." Apec '97 - Twelfth Annual Applied Power Electronics Conference and Exposition, Vols 1 and 2: 585-589.

Anwar, M. N. And Teimor, M., (2002). "An analytical method for selecting dc-link-capacitor of a voltage stiff inverter." Conference Record of the 2002 Ieee Industry Applications Conference, Vols 1-4: 803-810.

Arrillaga, J. (1997). Power System Harmonic Analysis, Wiley.

Asiminoaei, L., Blaabjerg, F. And Hansen, S., (2005). "Evaluation of harmonic detection methods for active power filter applications." APEC 2005: Twentieth Annual IEEE Applied Power Electronics Conference and Exposition, Vols 1-3: 635-641.

Asiminoaei, L., Blaabjerg, F. And Hansen, S., (2007). "Detection is key - Harmonic detection methods for active power filter applications." IEEE Industrial Electronics Magazine 13(4): 22-33.

Asiminoael, L., Blaabjerg, F. And Hansen, S., (2007). "Detection is key - Harmonic detection methods for active power filter applications." IEEE Industry Applications Magazine 13(4): 22-33.

Bai, H. F., Wang, X. F. And Blaabjerg, F., (2016). "Passivity Enhancement by Series LC Filtered Active Damper with Zero Current Reference." 2016 Ieee 8th International Power Electronics and Motion Control Conference (Ipemc-Ecce Asia).

Bai, H. F., Wang, X. F., Loh, P. C. And Blaabjerg, F., (2017). "Passivity Enhancement of Grid-Tied Converters by Series LC-Filtered Active Damper." Ieee Transactions on Industrial Electronics 64(1): 369-379.

Balasubramanian, A. K. And John, V., (2013). "Analysis and design of split-capacitor resistive-inductive passive damping for LCL filters in grid-connected inverters." Iet Power Electronics 6(9): 1822-1832.

Bao, C. L., Ruan, X. B., Wang, X. H., Li, W. W., Pan, D. H. And Weng, K. L., (2014). "Step-by-Step Controller Design for LCL-Type Grid-Connected Inverter with Capacitor-Current-Feedback Active-Damping." Ieee Transactions on Power Electronics 29(3): 1239-1253.

Bhattacharya, A., Chakraborty, C. And Bhattacharya, S., (2009). "Shunt compensation." IEEE Industrial Electronics Magazine 3(3): 38-49.

Bierhoff, M. H. And Fuchs, F. W., (2004). "Semiconductor losses in voltage source and current source IGBT converters based on analytical derivation." Pesc 04: 2004 Ieee 35th Annual Power Electronics Specialists Conference, Vols 1-6, Conference Proceedings: 2836-2842.

Bina, M. T. And Pashajavid, E., (2009). "An efficient procedure to design passive LCL-filters for active power filters." Electric Power Systems Research 79(4): 606-614.

Buyuk, M., Inci, M. And Tumay, M. (2016). Performance evaluation of LLCL filter for active power filter. 2016 IEEE 16th International Conference on Environment and Electrical Engineering (EEEIC).

Buyuk, M., Tan, A., Bayindir, K. C. And Tumay, M., (2015). "Analysis and Comparison of Passive Damping Methods for Shunt Active Power Filter with Output Lcl Filter." 2015 Intl Aegean Conference on Electrical

Machines & Power Electronics (Acemp), 2015 Intl Conference on Optimization of Electrical & Electronic Equipment (Optim) & 2015 Intl Symposium on Advanced Electromechanical Motion Systems (Electromotion): 434-440.

Buyuk, M., Tan, A. And Tumay, M., (2018). "Improved adaptive notch filter-based active damping method for shunt active power filter with LCL-filter." Electrical Engineering 100(3): 2037-2049.

Buyuk, M., Tan, A., Tumay, M. And Bayindir, K. C., (2016). "Topologies, generalized designs, passive and active damping methods of switching ripple filters for voltage source inverter: A comprehensive review." Renewable & Sustainable Energy Reviews 62: 46-69.

Büyük, M., (2015). Investigation and analysis of switching ripple filters for three-phase four-wire shunt active power filter. MSc, Çukurova.

Büyük, M., İnci, M., Tan, A. And Tümay, M., (2019). "Improved instantaneous power theory based current harmonic extraction for unbalanced electrical grid conditions." Electric Power Systems Research 177: 106014.

Büyük, M., Tan, A., Tümay, M. And Bayındır, K. Ç., (2016). "Topologies, generalized designs, passive and active damping methods of switching ripple filters for voltage source inverter: A comprehensive review." Renewable and Sustainable Energy Reviews 62: 46-69.

Channegowda, P. And John, V., (2010). "Filter Optimization for Grid Interactive Voltage Source Inverters." Ieee Transactions on Industrial Electronics 57(12): 4106-4114.

Chung, D. W. And Sul, S. K., (1997). "Minimum-loss PWM strategy for 3-phase PWM rectifier." Pesc'97: 28th Annual Ieee Power Electronics Specialists Conference - Record, Vols I and Ii: 1020-1026.

Çetin, A., (2007). Design and Implementation of a Voltage Source Converter Based STATCOM for Reactive Power Compensation and Harmonic Filtering. Doctor of Philosophy, Middle East Technical University.

Dannehl, J., Fuchs, F. W., Hansen, S. And Thogersen, P. B., (2010). "Investigation of Active Damping Approaches for PI-Based Current Control of Grid-Connected Pulse Width Modulation Converters With LCL Filters." Ieee Transactions on Industry Applications 46(4): 1509-1517.

Dannehl, J., Liserre, M. And Fuchs, F. W., (2011). "Filter-Based Active Damping of Voltage Source Converters With LCL Filter." Ieee Transactions on Industrial Electronics 58(8): 3623-3633.

El-Habrouk, M., Darwish, M. K. And Mehta, P., (2000). "Active power filters: A review." Iee Proceedings-Electric Power Applications 147(5): 403-413.

Fang, J. Y., Xiao, G. C., Yang, X. And Tang, Y., (2017). "Parameter Design of a Novel Series-Parallel-Resonant LCL Filter for Single-Phase Half-Bridge Active Power Filters." Ieee Transactions on Power Electronics 32(1): 200-217.

Fujita, H. And Akagi, H., (1991). "A practical approach to harmonic compensation in power systems-series connection of passive and active filters." IEEE Transactions on Industry Applications 27(6): 1020-1025.

Ge, H. Y., Zhen, Y. W., Wang, Y. And WANG, D., (2017). "Research on LCL Filter Active Damping Strategy in Active Power Filter System." 2017 9th International Conference on Modelling, Identification and Control (Icmic 2017): 476-481.

Geddada, N., Karanki, S. B. And Mishra, M. K. (2012). Synchronous reference frame based current controller with SPWM switching strategy for DSTATCOM applications. 2012 IEEE International Conference on Power Electronics, Drives and Energy Systems (PEDES).

Guo, X. Q., Wu, W. Y. And Gu, H. R., (2010). "Modeling and simulation of direct output current control for LCL-interfaced grid-connected inverters with parallel passive damping." Simulation Modelling Practice and Theory 18(7): 946-956.

Han, Y., Xu, L., Khan, M. M., Chen, C., Yao, G. And Zhou, L. D., (2011). "Robust Deadbeat Control Scheme for a Hybrid APF With Resetting Filter and ADALINE-Based Harmonic Estimation Algorithm." Ieee Transactions on Industrial Electronics 58(9): 3893-3904.

He, J. W., Liang, B. H., Li, Y. W. And Wang, C. S., (2017). "Simultaneous Microgrid Voltage and Current Harmonics Compensation Using Coordinated Control of Dual-Interfacing Converters." Ieee Transactions on Power Electronics 32(4): 2647-2660.

He, N., Xu, D. H., Zhu, Y., Zhang, J., Shen, G. Q., Zhang, Y. F., Ma, J. And Liu, C. J., (2013). "Weighted Average Current Control in a Three-Phase Grid Inverter With an LCL Filter." Ieee Transactions on Power Electronics 28(6): 2785-2797.

Hu, G. Z., Chen, C. S. And Duan, S. X., (2013). "New Active Damping Strategy for LCL-Filter-Based Grid-Connected Inverters with Harmonics Compensation." Journal of Power Electronics 13(2): 287-295.

IEC (1990). IEC TR 61000-2-1:1990 Electromagnetic compatibility (EMC) - Part 2: Environment - Section 1: Description of the environment - Electromagnetic environment for low-frequency conducted disturbances and signalling in public power supply systems, IEC: 48.

IEC (1998). IEC TS 61000-3-4:1998 Electromagnetic compatibility (EMC) - Part 3-4: Limits - Limitation of emission of harmonic currents in low-voltage power supply systems for equipment with rated current greater than 16 A, IEC: 29.

IEC (2002). IEC 61000-2-2:2002 Electromagnetic compatibility (EMC) - Part 2-2: Environment - Compatibility levels for low-frequency conducted disturbances and signalling in public low-voltage power supply systems, IEC: 57.

IEEE (1992). IEEE Std 519-1992 Recommended Practices and Requirements for Harmonic Control in Electrical Power Systems, IEEE: 112.

IEEE (2009). IEEE Std 1159-2009 Recommended Practice for Monitoring Electric Power Quality: 81.

Inci, M., Buyuk, M. And Tumay, M., (2016). "FFT based Reference Signal Generation to Compensate Simultaneous Voltage Sag/Swell and Voltage Harmonics." 2016 Ieee 16th International Conference on Environment and Electrical Engineering (Eeeic).

Jia, L., Ruan, X. B., Zhao, W. X., Lin, Z. H. And Wang, X. H., (2018). "An Adaptive Active Damper for Improving the Stability of Grid-Connected Inverters Under Weak Grid." Ieee Transactions on Power Electronics 33(11): 9561-9574.

Jia, Y. Q., Zhao, J. Q. And Fu, X. W., (2014). "Direct Grid Current Control of LCL-Filtered Grid-Connected Inverter Mitigating Grid Voltage Disturbance." Ieee Transactions on Power Electronics 29(3): 1532-1541.

Leblanc, D., Nahid-Mobarakeh, B., Pham, B., Pierfederici, S. And Davat, B., (2013). "Stability analysis and active stabilization by a centralized stabilizer of Voltage-Source-Rectifier Loads in AC microgrids." 2013 Ieee Industry Applications Society Annual Meeting.

Li, L. And Jiang, X., (2013). "Research on Control Strategy for Three-Phase Four-Wire LCL-Based Active Power Filter." International Journal of Computer and Electrical Engineering 5(13): 5.

Li, Y. W., (2009). "Control and Resonance Damping of Voltage-Source and Current-Source Converters With LC Filters." Ieee Transactions on Industrial Electronics 56(5): 1511-1521.

Liang, X. D. And Ilochonwu, O., (2011). "Passive harmonic filter design scheme subsea cable applications with six-pulse variable frequency drives." Ieee Industry Applications Magazine 17(5): 36-44.

Liserre, M., Blaabjerg, F. And Hansen, S., (2005). "Design and control of an LCL-filter-based three-phase active rectifier." IEEE Transactions on Industry Applications 41(5): 1281-1291.

Liu, C., Dai, K., Duan, K. W. And Kang, Y., (2013). "Application of a C-Type Filter Based LCFL Output Filter to Shunt Active Power Filters." Journal of Power Electronics 13(6): 1058-1069.

Liu, Q., Peng, L., Kang, Y., Tang, S. Y., Wu, D. L. And Qi, Y., (2014). "A Novel Design and Optimization Method of an LCL Filter for a Shunt Active Power Filter." Ieee Transactions on Industrial Electronics 61(8): 4000-4010.

Lo Calzo, G., Lidozzi, A., Solero, L. And Crescimbini, F., (2015). "LC Filter Design for On-Grid and Off-Grid Distributed Generating Units." Ieee Transactions on Industry Applications 51(2): 1639-1650.

Longhui, W., Fang, Z., Pengbo, Z., Hongyu, L. And Zhaoan, W., (2007). "Study on the Influence of Supply-Voltage Fluctuation on Shunt Active Power Filter." IEEE Transactions on Power Delivery 22(3): 1743-1749.

Malinowski, M., Kazmierkowski, M. P. And Bernet, S., (2005). "New simple active damping of resonance in three-phase PWM converter with LCL filter." 2005 IEEE International Conference on Industrial Technology - (ICIT), Vols 1 and 2: 925-929.

Özkaya, H., (2007). Parallel Active Filter Design, Control, and Implementation. Master of Science, Middle East Technical University.

Özkaya, H., (2007). Parallel Active Filter Design, Control, and Implementation. MsC, Middle East Technical University.

Pan, D. H., Ruan, X. B., Bao, C. L., Li, W. W. And Wang, X. H., (2014). "Capacitor-Current-Feedback Active Damping With Reduced Computation Delay for Improving Robustness of LCL-Type Grid-Connected Inverter." Ieee Transactions on Power Electronics 29(7): 3414-3427.

Pena-Alzola, R., Liserre, M., Blaabjerg, F., Ordonez, M. And Kerekes, T., (2014). "A Self-commissioning Notch Filter for Active Damping in a Three-Phase LCL-Filter-Based Grid-Tie Converter." Ieee Transactions on Power Electronics 29(12): 6754-6761.

Pena-Alzola, R., Liserre, M., Blaabjerg, F., Sebastian, R., Dannehl, J. And Fuchs, F. W., (2013). "Analysis of the Passive Damping Losses in LCL-Filter-Based Grid Converters." Ieee Transactions on Power Electronics 28(6): 2642-2646.

Pena-Alzola, R., Liserre, M., Blaabjerg, F., Sebastian, R., Dannehl, J. And Fuchs, F. W., (2014). "Systematic Design of the Lead-Lag Network Method for Active Damping in LCL-Filter Based Three Phase Converters." Ieee Transactions on Industrial Informatics 10(1): 43-52.

Pettersson, S., Salo, M. And Tuusa, H., (2006). "Applying an LCL-filter to a four-wire active power filter." 2006 Ieee Power Electronics Specialists Conference, Vols 1-7: 605-611.

Reznik, A., Simoes, M. G., Al-Durra, A. And Muyeen, S. M., (2014). "LCL Filter Design and Performance Analysis for Grid-Interconnected Systems." Ieee Transactions on Industry Applications 50(2): 1225-1232.

Routimo, M., Salo, M. And Tuusa, H., (2007). "Comparison of Voltage-Source and Current-Source Shunt Active Power Filters." IEEE Transactions on Power Electronics 22(2): 636-643.

Routimo, M. And Tuusa, H., (2007). "LCL type supply filter for active power filter - Comparison of an active and a passive method for resonance damping." 2007 Ieee Power Electronics Specialists Conference, Vols 1-6: 2939-2945.

Semikron. (2007). "Datasheet of SKYPER 32 PRO R". https://www.semikron.com. Last Access Date: September 2015.

Semikron. (2014). "Datasheet of SEMiX202GB12E4s". https://www.semikron.com. Last Access Date: June 2014.

Semikron. (2015). "Application Manual Power Semiconductors ". http://www.semikron.com/. Last Access Date: September 2015.

Serpa, L. A., Ponnaluri, S., Barbosa, P. M. And Kolar, J. W., (2007). "A modified direct power control strategy allowing the connection of three-phase inverters to the grid through LCL filters." Ieee Transactions on Industry Applications 43(5): 1388-1400.

Shen, G. Q., Zhu, X. C., Zhang, J. And Xu, D. H., (2010). "A New Feedback Method for PR Current Control of LCL-Filter-Based Grid-Connected Inverter." Ieee Transactions on Industrial Electronics 57(6): 2033-2041.

Singh, B., Al-Haddad, K. And Chandra, A., (1999). "A review of active filters for power quality improvement." Ieee Transactions on Industrial Electronics 46(5): 960-971.

Tan, A., (2015). Design and Implementation of a Shunt Hybrid Active Power Filter. Doctor of Philosophy, Çukurova Univertsity.

Tan, A., Bayindir, K. C., Cuma, M. U. And Tumay, M., (2017). "Multiple harmonic elimination-based feedback controller for Shunt Hybrid Active Power Filter." Iet Power Electronics 10(8): 945-956.

Tang, S. Y., Peng, L. And Kang, Y., (2011). "Active Damping Method Using Grid-Side Current Feedback for Active Power Filters with LCL Filters." Journal of Power Electronics 11(3): 311-318.

Tang, Y., Loh, P. C., Wang, P., Choo, F. H., Gao, F. And Blaabjerg, F., (2011). "Design, Control, and Implementation of LCL-Filter-Based Shunt Active Power Filters." 2011 Twenty-Sixth Annual Ieee Applied Power Electronics Conference and Exposition (Apec): 98-105.

Tang, Y., Loh, P. C., Wang, P., Choo, F. H., Gao, F. And Blaabjerg, F., (2012). "Generalized Design of High Performance Shunt Active Power Filter With Output LCL Filter." Ieee Transactions on Industrial Electronics 59(3): 1443-1452.

Terciyanlı, A., (2010). Design and Implementation of a Current Source Converter Based Active Power Filter for Medium Voltage Applications. PhD, Middle East Technical University.

Texas-Instruments. (2014). "Datasheet of AMC1100". http://www.ti.com/product/AMC1100. Last Access Date: December 2014.

Texas-Instruments. (2015). "TMS320F28335 Delfino Microcontroller". http://www.ti.com/product/tms320f28335. Last Access Date: September 2015.

Texas-Instruments. (2017). "Datasheet of AMC1301". http://www.ti.com/product/AMC1301. Last Access Date: January 2017.

Texas-Instruments. (2018). "Datasheet of AMC1311". http://www.ti.com/product/AMC1311. Last Access Date: June 2018.

Texas-Instruments. (2018). "TMS320F28379D Delfino Microcontroller". http://www.ti.com/product/TMS320F28379D. Last Access Date: November 2018.

Thomas, T., Haddad, K., Joos, G. And Jaafari, A., (1998). "Design and performance of active power filters." IEEE Industry Applications Magazine 4(5): 38-46.

Tian, Y. S. And Jiang, Q. R., (2013). "A Dual-Current-Loop Control Method Based On System Current Detection for LCL-Filter-Based Active Power Filters." 39th Annual Conference of the Ieee Industrial Electronics Society (Iecon 2013): 8498-8503.

Uçak, O., (2009). Design and Implementation of a Voltage Source Converter Based Hybrid Active Power Filter. Master of Science, Middle East Technical University.

Usluer, S. N. And Hava, A. M., (2014). "Investigation on Series Active Filter Compensated High Power Grid-Connected Voltage Source Inverters with LCL Filter." 2014 Ieee Energy Conversion Congress and Exposition (Ecce): 381-388.

Usluer, S. N. And Hava, A. M., (2014). "Series Active Filter Based Resonance Damping of High Power Three-phase, LCL Filtered, Grid Connected Voltage Source Inverters." 2014 Ieee 23rd International Symposium on Industrial Electronics (Isie): 643-648.

Vodyakho, O. And Mi, C. C., (2009). "Three-Level Inverter-Based Shunt Active Power Filter in Three-Phase Three-Wire and Four-Wire Systems." Ieee Transactions on Power Electronics 24(5-6): 1350-1363.

Wang, X. F., Blaabjerg, F. And Liserre, M., (2014). "An Active Damper to Suppress Multiple Resonances with Unknown Frequencies." 2014 Twenty-Ninth Annual Ieee Applied Power Electronics Conference and Exposition (Apec): 2184-2191.

Wang, X. F., Blaabjerg, F., Liserre, M., Chen, Z., He, J. W. And Li, Y. W., (2014). "An Active Damper for Stabilizing Power-Electronics-Based AC Systems." Ieee Transactions on Power Electronics 29(7): 3318-3329.

Wang, X. F., Pang, Y., Loh, P. C. And Blaabjerg, F., (2015). "A Series-LC-Filtered Active Damper With Grid Disturbance Rejection for AC Power-Electronics-Based Power Systems." Ieee Transactions on Power Electronics 30(8): 4037-4041.

Wang, Y., Liu, J. Z. And Xu, X. T., (2014). "Study of A New Grid-connected LCL Filter for Shunt Active Power Filter." 2014 Ieee Transportation Electrification Conference and Expo (Itec) Asia-Pacific 2014.

Wojciechowski, D., (2010). "Predictive Control of High Power Active Filter System with LCL Circuit." Ieee International Symposium on Industrial Electronics (Isie 2010): 2575-2580.

Xie, C., Wang, Y., Zhong, X. J. And Chen, G. Z., (2012). "A Novel Active Damping Method for LCL-Filter-Based Shunt Active Power Filter." 2012 Ieee International Symposium on Industrial Electronics (Isie): 64-69.

Xu, Y., Yu, J. R., Cao, Y. J., Lu, X. N. And Yu, J. Q., (2016). "Double resonant output filter to eliminating the tradeoff between bandwidth and switching ripple in shunt active power filters." Iet Power Electronics 9(4): 846-854.

Yan, Z. Y. And Zhu, G. P., (2012). "Voltage ripple across the capacitor in DC side of shunt APF." 2012 Ieee International Conference on Power System Technology (Powercon).

Yang, L. And Yang, J. Q., (2018). "Robust Current Control Method for LCL-Type Shunt Active Power Filters with Inverter-Side Current Feedback Active Damping." 2018 Ieee Energy Conversion Congress and Exposition (Ecce): 5706-5712.

Yang, L. And Yang, J. Q., (2019). "A Robust Dual-Loop Current Control Method With a Delay-Compensation Control Link for LCL-Type Shunt Active Power Filters." Ieee Transactions on Power Electronics 34(7): 6183-6199.

Yuan, H. W. And Jiang, X. J., (2016). "A Simple Active Damping Method for Active Power Filters." Apec 2016 31st Annual Ieee Applied Power Electronics Conference and Exposition: 907-912.

Zeng, G. H., Rasmussen, T. W., Ma, L. And Teodorescu, R., (2010). "Design and Control of LCL-Filter with Active Damping for Active Power Filter." Ieee International Symposium on Industrial Electronics (Isie 2010): 2557-2562.

Zhang, Y., Xue, M. Y., Li, M. Y., Kang, Y. And Guerrero, J. M., (2014). "Co-design of the LCL Filter and Control for Grid-Connected Inverters." Journal of Power Electronics 14(5): 1047-1056.

Zhao, W. Q. And Chen, G. Z., (2009). "Comparison of Active and Passive Damping Methods for Application in High Power Active Power Filter with LCL-filter." 2009 International Conference on Sustainable Power Generation and Supply, Vols 1-4: 2128-2133.

Zou, Z. X., Wang, Z. And Cheng, M., (2014). "Modeling, Analysis, and Design of Multifunction Grid-Interfaced Inverters With Output LCL Filter." Ieee Transactions on Power Electronics 29(7): 3830-3839.

BIOGRAPHY

Mehmet BÜYÜK was born in Mardin, Turkey in 1989. He graduated from Anafartalar Anatolian High School in 2006. He received his BSc and MsC degrees in Electrical and Electronics Engineering from Çukurova University, Adana, Turkey, in 2012 and 2015, respectively. He has been working as a Research Assistant in Electrical and Electronics Engineering Department of Çukurova University since 2015. His research interests include electric energy quality, power electronic converters and applications, renewable energy systems and energy efficiency applications.

APPENDICES

APPENDIX A: Technical Specifications Of Igbt Modules And Igbt Driver

Table A.1. Technical specifications of SEMiX202GB12E4s (Semikron, 2015)

Man.	SEMIKRON				
No	SEMiX202GB12E4s				
V_{CES}	$T_j = 25^oC$			1200 V	
I_C	$T_j = 175^oC$		$T_c = 25^oC$	312 A	
			$T_c = 80^oC$	240 A	
I_{Cnom}	200 A				
I_{CRM}	600 A				
			min	typ.	max
$V_{CE(sat)}$	$I_C = 200A$ $V_{GE} = 15V$ chiplevel	$T_j = 25^oC$		1.8V	2.05V
		$T_j = 150^oC$		2.20V	2.40V
I_{CES}	$V_{GE} = 0V$ $V_{CE} = 1200V$	$T_j = 25^oC$			2.7mA
		$T_j = 150^oC$			
R_{Gint}	$T_j = 25^oC$			3.75Ω	
Q_G	$V_{GE} = -8V \dots + 15V$			1130nC	
$t_{d(on)}$	$V_{CC} = 600V$ $I_C = 200A$ $V_{GE} = +15/-15V$ $R_{Gon} = 2.4\Omega$ $R_{Goff} = 2.4\Omega$ $di/dt_{on} = 3600A/\mu s$ $di/dt_{off} = 2100A/\mu s$ $T_j = 150^oC$			253ns	
t_r				55ns	
E_{on}				22mJ	
$t_{d(off)}$				533ns	
t_f				113ns	
E_{off}				27.9mJ	
V_f	$I_f = 200A$ $V_{GE} = 0V$ chiplevel	$T_j = 25^oC$		2.2V	2.52V
		$T_j = 150^oC$		2.15V	2.47V
E_{rr}	$I_f = 200A$ $di/dt_{off} = 3400A/\mu s$ $V_{GE} = -15V$ $V_{CC} = 600V$ $T_j = 150^oC$			12mJ	

Table A.2. Technical specifications of SKYPER 32 PRO P (Semikron, 2007)

Man.	SEMIKRON		
No	SKYPER 32 PRO R		
Specifications	• Two channels output • Soft turn-off • Drive interlock • Dynamic short circuit protection • Under voltage protection • Halt status with failure management • External failure input		
V_{CEmax}	1700V		
I_{outmax}	15A		
f_{max}	50kHz		
V_{dcmax}	1200Vdc		
V_{isol}	4000V		
$R_{Gon\ min}$	1.5Ω		
$R_{Goff\ min}$	1.5Ω		
$Q_{out}/pulse$	6.3uC		
	min	typ	max
V_S	14.4V	15V	15.6V
$I_{Snoload}$	80mA	-	-
I_{Smax}	-	-	500mA
V_{IH}	-	15V	-
V_{IL}	-	0V	-
V_{Gon}	-	+15V	-
V_{Goff}	-	-7V	-
$t_{d(on)}$	-	1.2us	
$t_{d(off)}$	-	1.2us	-
$t_{r(out)}$	-	-	-
$t_{f(out)}$	-	-	-

Table A.3. Technical specifications of SKM100GB12T4 (Semikron, 2013)

Man.	SEMIKRON				
No	SKM100GB12T4				
V_{CES}	$T_j = 25^oC$			1200 V	
I_C	$T_j = 175^oC$	$T_c = 25^oC$		160 A	
		$T_c = 80^oC$		123 A	
I_{Cnom}	100 A				
I_{CRM}	300 A				
			min	typ.	max
$V_{CE(sat)}$	$I_C = 150A$ $V_{GE} = 15V$ chiplevel	$T_j = 25^oC$		1.8V	2.05V
		$T_j = 150^oC$		2.20V	2.40V
I_{CES}	$V_{GE} = 0V$ $V_{CE} = 1200V$	$T_j = 25^oC$			1mA
		$T_j = 150^oC$			
R_{Gint}	$T_j = 25^oC$			7.5Ω	
Q_G	$V_{GE} = -8V ... + 15V$			565nC	
$t_{d(on)}$	$V_{CC} = 600V$ $I_C = 200A$ $V_{GE} = +15/-15V$ $R_{Gon} = 2.4\Omega$ $R_{Goff} = 2.4\Omega$ $di/dt_{on} = 3600A/\mu s$ $di/dt_{off} = 2100A/\mu s$ $T_j = 150^oC$			165ns	
t_r				47ns	
E_{on}				15mJ	
$t_{d(off)}$				400ns	
t_f				75ns	
E_{off}				10.2mJ	
V_f	$I_f = 200A$ $V_{GE} = 0V$ chiplevel	$T_j = 25^oC$		2.2V	2.52V
		$T_j = 150^oC$		2.15V	2.47V
E_{rr}	$I_f = 200A$ $di/dt_{off} = 3400A/\mu s$ $V_{GE} = -15V$ $V_{CC} = 600V$ $T_j = 150^oC$			5.9mJ	

APPENDIX B: FLOWCHART OF INTERRUPT FUNCTIONS

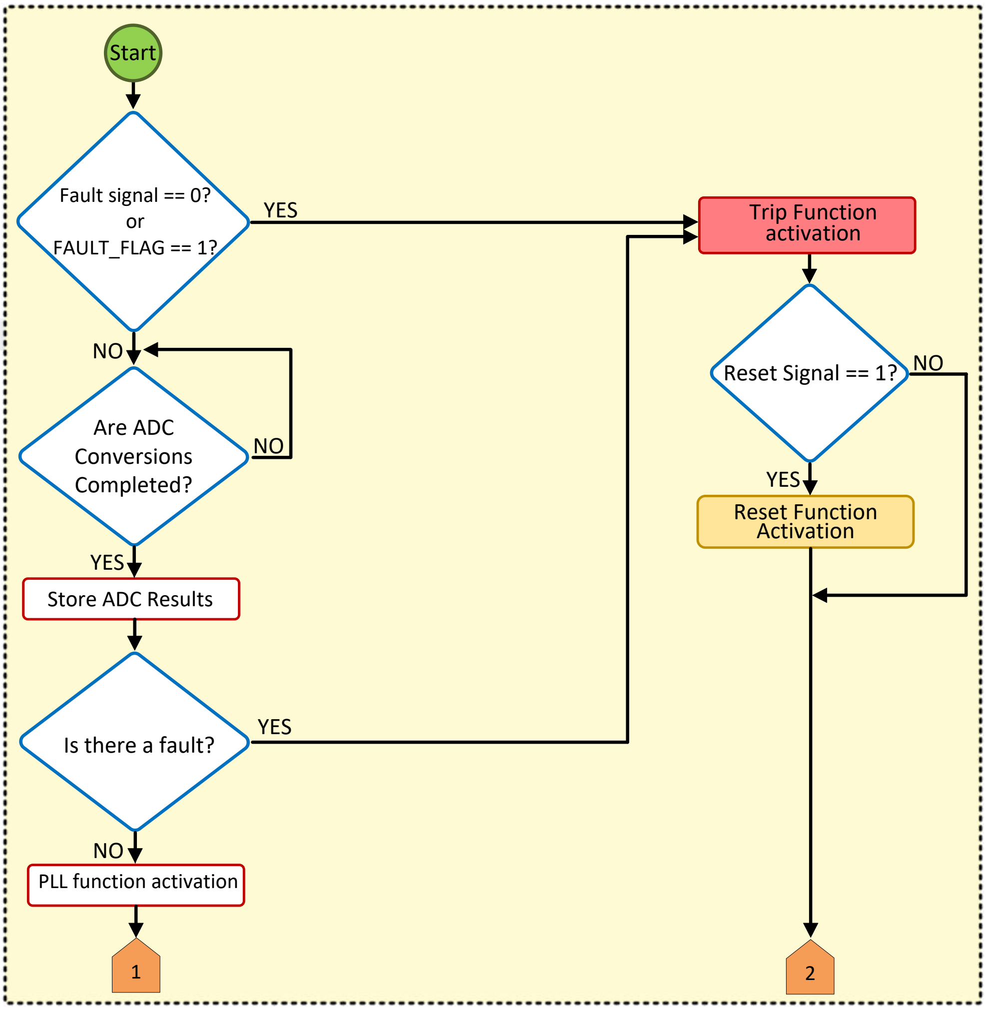

Figure B.1. SAPF interrupt function – Part 1

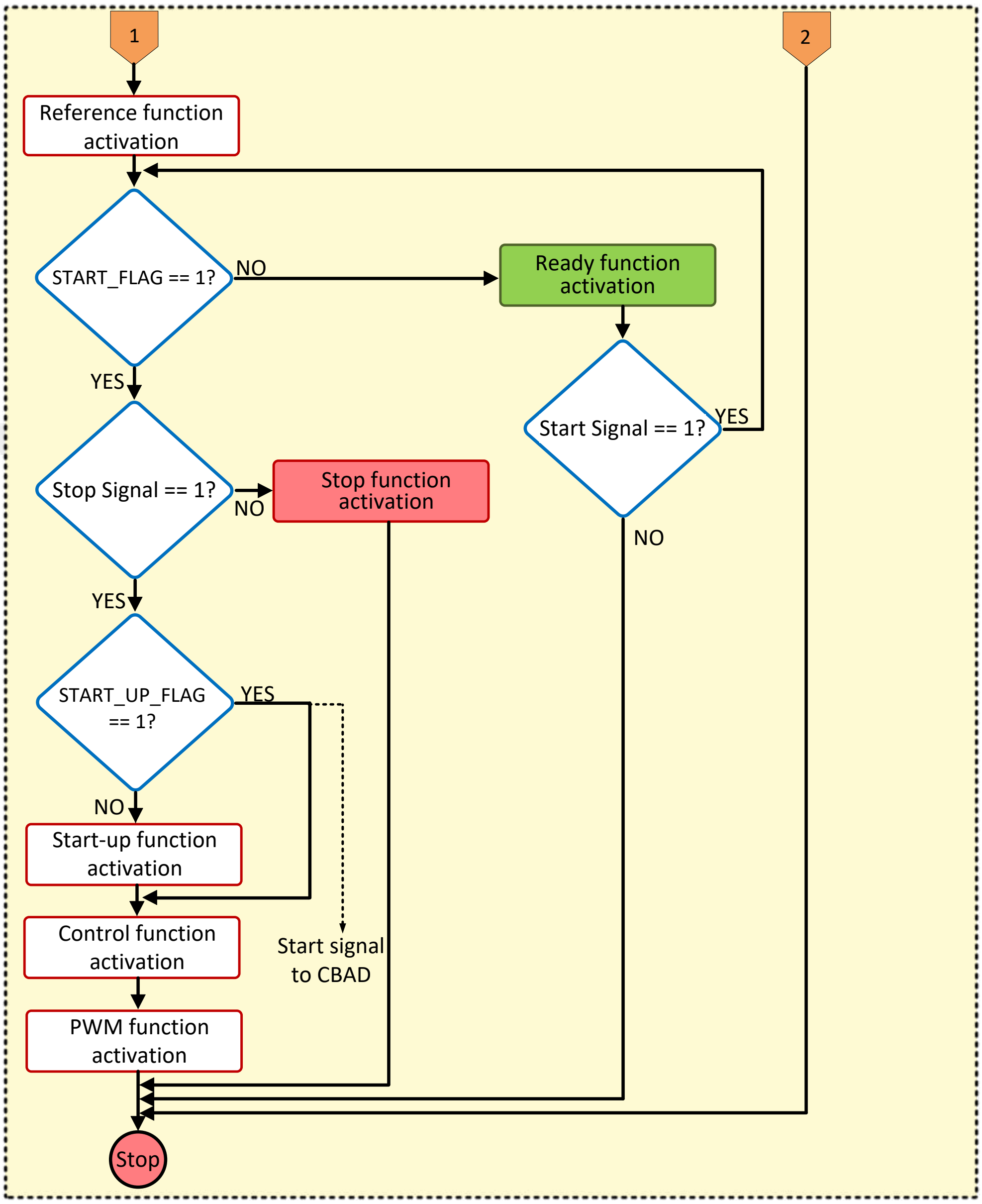

Figure B.2. SAPF interrupt function – Part 2

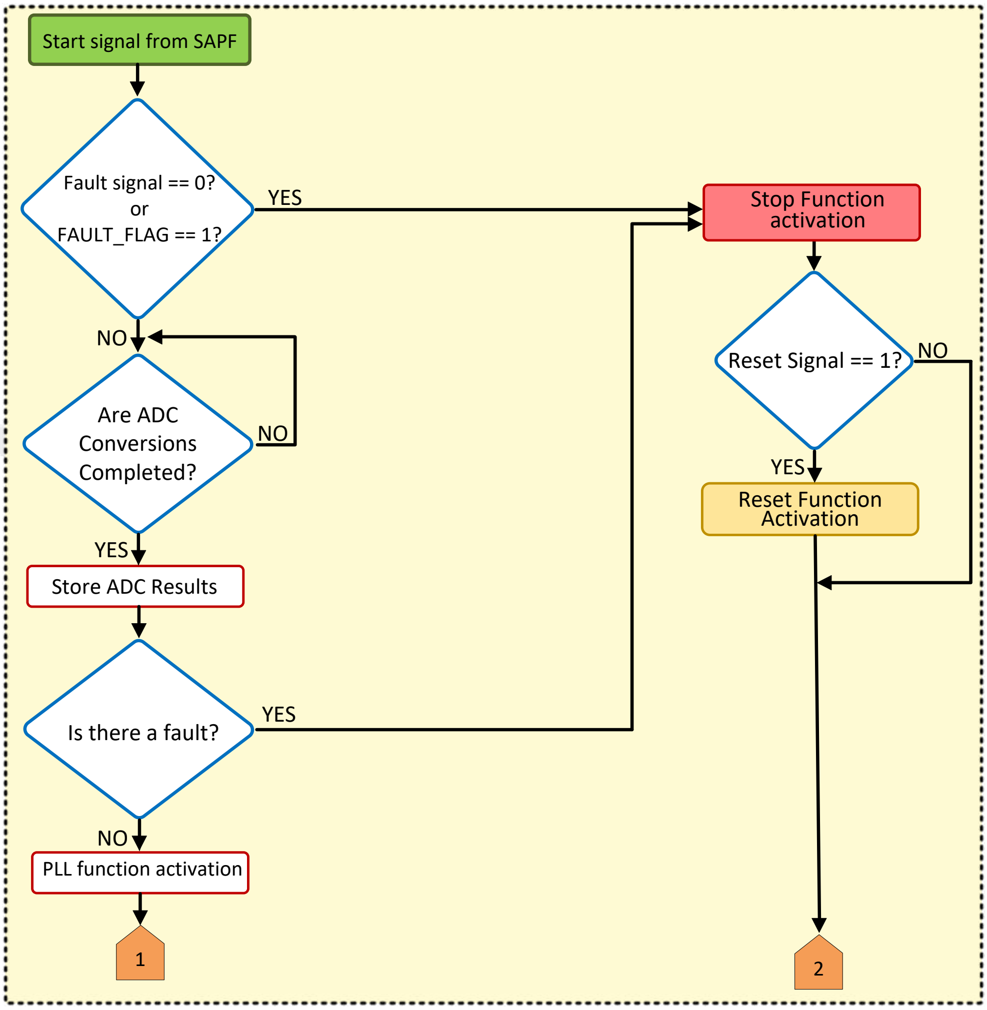

Figure B.3. CBAD interrupt function – Part 1

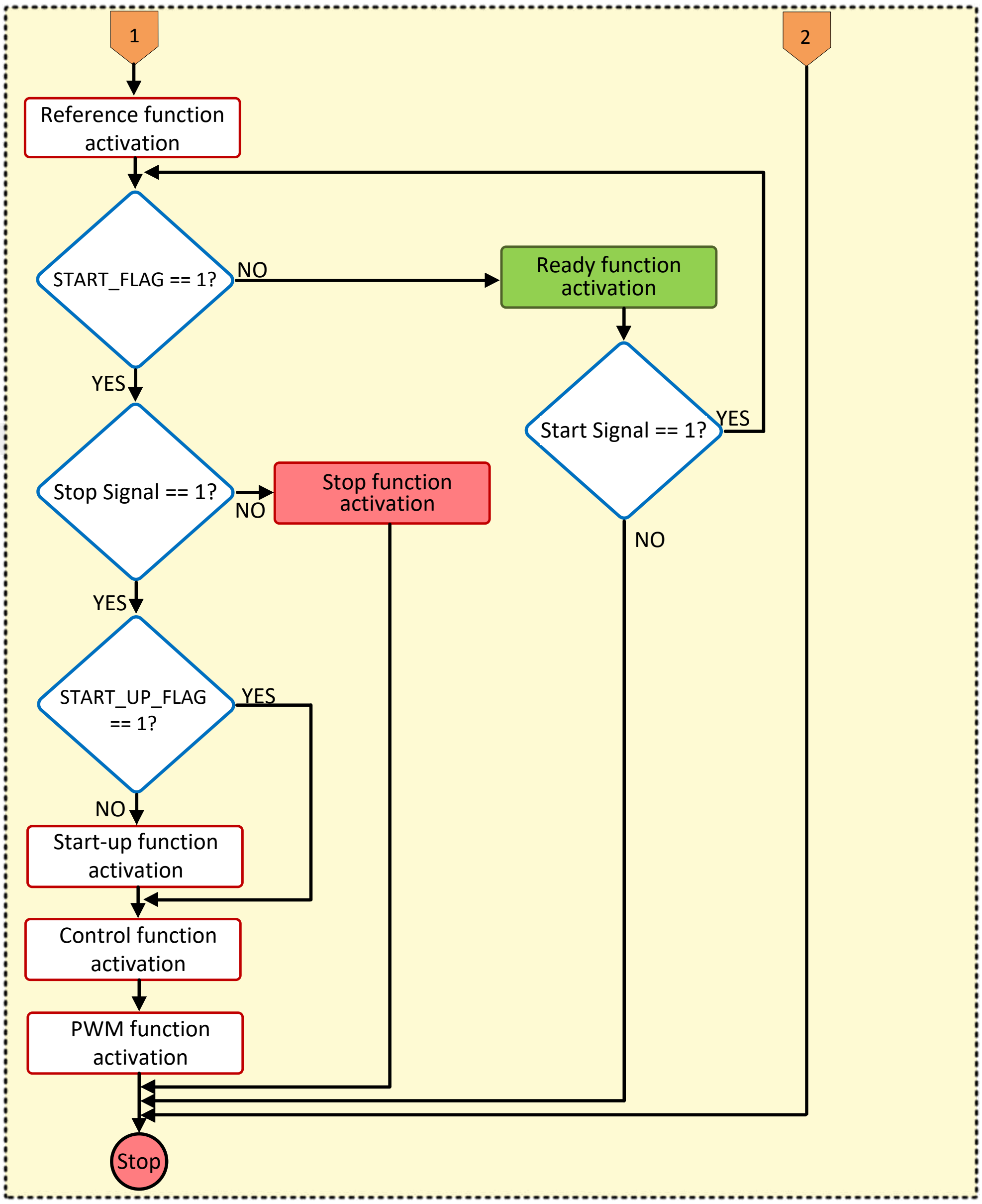

Figure B.4. CBAD interrupt function – Part 2